Technical University of Denmark

DTU

Metmaterials for sensing applications

Jeppesen, Claus; Kristensen, Anders; Boltasseva, Alexandra

Publication date:
2011

Document Version
Publisher's PDF, also known as Version of record

Link back to DTU Orbit

DTU Library
Technical Information Center of Denmark

Ph.D. Thesis

Metamaterials for Sensing Applications

Claus Jeppesen

Main supervisor: Anders Kristensen
Co-supervisor: Niels Asger Mortensen
Co-supervisor: Alexandra Boltasseva

Department of Micro- and Nanotechnology
Technical University of Denmark

14 December 2010

ii

Abstract

The objective of this PhD work is to experimentally investigate the sensing potential of different plasmonic metamaterial designs. There is a natural focus on performance parameters such as resolution and figure-of-merit but thought have also been put into the material choice to enable later integration by i.e. considering the compatibility with down-stream processing.

The project is divided into two parts. The first part deals with nanometer thin silver lenses that enable sub-wavelength resolution imaging in the near-field. As opposed to conventional optical lenses typically made out of glass, these silver lenses can resolve structures smaller than the diffraction limit of light. The project focuses on the highly demanding fabrication of these metal lenses, which requires extensive optimization due to small fabrication tolerances. We apply the overall superlens design by Fang *et al.* [1], demonstrating superlensing via a photolithographic read-out scheme where light intensity is converted into topographical modulations of a UV-sensitive resist.

The second part of the project focuses on planar gold Split-Ring Resonator (SRR) structures, which is one of the central and most extensively studied optical metamaterials. This is mainly due to a simple analytical circuit model description of the ground mode resonance and because of an uncomplicated fabrication process. All dimensions of the split-ring resonators are in the nanoscale and the ground mode resonance is at telecommunication wavelengths. The SRRs' resonance position is highly sensitive to the local dielectric environment and hence, SRRs can be employed as refractometric sensors. SRRs can detect minute changes in bulk refractive index by monitoring the corresponding shift of the resonance position. To optimize the sensor performance, the resonance linewidth is narrowed by addressing different loss mechanisms. The bulk sensitivity is characterized through cladding tuning experiments using index oils. The fluidic tuning experiments also lead to an extended circuit model that takes all geometrical parameters and host materials into account.

All the structures have been fabricated using state-of-the-art cleanroom facilities and the experimental results are supported by full-wave 2D/3D numerical modeling.

Dansk resumé

Formålet med dette PhD projekt er eksperimentielt at undersøge sensor potentialet af forskellige plasmoniske metamateriale designs. Der er et naturligt fokus på præstations-parametre som eksempelvis opløsning og "figure-of-merit", men der er også gjort overve-jelser omkring materialevalget med henblik på kompatibilitet med eventuelle procestrin, som er nødvendige ved senere integration af komponenterne.

Projektet er delt op i to dele. Den første del handler om nanometer tynde sølv linser som muliggører en opløsning bedre end lysets bølgelængde i nær-feltet. Til forskel fra nor-male optiske linser, som typisk er lavet af glas, så kan disse sølv linser opløse strukturer mindre end diffraktionsgrænsen af lyset. Projektet fokuserer på den krævende fabrikation af disse metal linser, som forudsætter omfattende optimering på grund af små fabrikations tolerancer. Vi benytter Fang et al.'s [1] superlinse design, hvor superlinse effekten demon-streres via fotolitografisk udlæsning, hvor lysintensitet bliver konverteret til topografiske modulationer af en UV-følsom resist.

Den anden del af projektet fokuserer på guld "Split-Ring" Resonatorer (SRR), som er en af de centrale og mest undersøgte optiske metamaterialer. Det er primært på grund af en simpel analytisk resonans beskrivelse via en elektrisk kredsløbsmodel, og fordi de er enkle at fabrikere. Alle dimensionerne af SRR strukturerne er i nanoskala og den grundlæggende resonans er ved telekommunikations bølgelængder. Resonans positionen er yderst følsom overfor det lokale dielektriske miljø og derfor kan split-ring resonatorer bruges some refraktometriske sensorer. Med SRR strukturer kan man detektere små æn-dringer i brydningsindeks ved at observere det tilhørende skifte i resonans positionen. Ved at minimere tabene, kan resonanslinjebredden reduceres og derved forbedres sensor præ-stationerne. Følsomheden karakteriseres gennem tuning eksperimenter med indeks olier. Tunings eksperimenterne fører også til en udvidet kredsløbsmodel som tager højde for alle geometriske parametre og værtsmaterialer.

Alle strukturerne er blevet fabrikeret ved brug af avancerede renrums faciliteter og de eksperimentielle resultater er understøttet af numeriske 2D/3D beregninger.

List of publications

Publications submitted as part of the Ph.D. thesis. The publications are referred to in the text by roman numerals.

I. **C. Jeppesen**, R. B. Nielsen, A. Boltasseva, S. Xiao, N. A. Mortensen, and A. Kristensen, *Thin film Ag superlens towards lab-on-a-chip integration*, Opt. Express, **17**(25), 22543-22552 (2009). Selected for the Virtual Journal for Biomedical Optics, Volume 5, Issue 1, Jan. 4, 2010.

II. **C. Jeppesen**, N.A. Mortensen, and A. Kristensen, *Capacitance tuning of nanoscale split-ring resonators*, Appl. Phys. Lett., **95**(19), 193108 (2009). Selected for the Virtual Journal of Nanoscale Science & Technology, Nov. 16, 2009.

III. **C. Jeppesen**, S. Xiao, N.A. Mortensen, and A. Kristensen, *Extended verification of scaling behavior in split-ring resonators*, Opt. Commun., **284**, 799-801 (2011).

IV. **C. Jeppesen**, N.A. Mortensen, and A. Kristensen, *The effect of Ti and ITO adhesion layers on gold split-ring resonators*, Appl. Phys. Lett., Accepted (2010).

V. **C. Jeppesen**, S. Xiao, N.A. Mortensen, and A. Kristensen, *Metamaterial localized resonance sensors: prospects and limitations*, Opt. Express, **18**(24), 25075-25080 (2010).

Preface and acknowledgments

This thesis is submitted in partial fulfillment of the requirements for obtaining the Doctor of Philosophy (Ph.D.) degree at the Technical University of Denmark (DTU). The work presented here has been carried out at the Department of Micro and Nanotechnology (DTU Nanotech) in the optofluidics group and in the DTU Danchip clean-room facilities during the period December 2007 to December 2010.

The project was supervised by Professor Anders Kristensen, whom I acknowledge for his enthusiasm and encouragement during the project. I also thank my other supervisor Associate Professor Niels Asger Mortensen for his theoretical insight and good discussions, which I have largely benefited from during the second half of the project. I thank Associate Professor Alexandra Boltasseva for introducing me to the exciting world of plasmonics and metamaterials.

The pleasant working environment in the group is of course also thanks to all the past and present group members. I thank everybody for being such good colleagues. In particular I acknowledge my office colleagues Asger Laurberg Vig and Morten Bo Mikkelsen.

I am also indebted to numerous other people at DTU Nanotech and DTU Fotonik. Assistant Professor Sanshui Xiao for invaluable help with the modeling, Rasmus Bundgaard Nielsen for taking part in a joint fabrication effort to kickstart the project, and Assistant Professor Radu Malureanu for helping me with the far-field characterization, fruitful discussions and keeping the measurement setup in good shape.

I am also grateful for the financial support from the Otto Moensteds foundation, which enabled me to visit a number of conferences and present my results.

Claus Jeppesen
14 December 2010

Contents

List of Figures

Abbreviations and Symbols

Abbreviation	Description
AFM	Atomic Force Microscope
CL	CathodoLuminescence
COC	Cyclo-Olefin Copolymer
EBL	Electron-Beam Lithography
EELS	Electron Energy Loss Spectroscopy
FOM	Figure-Of-Merit
MZI	Mach-Zehnder Interferometer
NA	Numerical Aperture
NFSL	Near-Field SuperLens
NIL	NanoImprint Lithography
NIM	Negate Index Material
OSA	Optical Spectrum Analyzer
OTF	Optical Transfer Function
PMMA	Poly(Methyl Methacrylate)
PSF	Point Spread Function
QD	Quantum Dot
RIE	Reactive Ion Etch
RIU	Refractive Index Unit
SAM	Self-Assembled Monolayer
SEM	Scanning Electron Microscope
SERS	Surface Enhanced Raman Scattering
SNOM	Scanning Near-field Optical Microscope
SPR	Surface Plasmon Resonance
SRR	Split-Ring Resonator
STS	Scanning Tunneling Spectroscopy
TE	Transverse Electric
TM	Transverse Magnetic

Symbol	Description	Unit
$\mathbf{r}$	Position vector	m
x, y, z	Position coordinates	m
$\mathbf{k}$	Wave vector	m^{-1}
k_x, k_y, k_z	Wave coordinates/spatial frequencies	m^{-1}
k_0	Vacuum wavenumber	m^{-1}
k_c	Cut-off frequency	m^{-1}
λ_0	Vacuum wavelength	m
ω	Angular frequency	rad/s
n	Refractive index	
ε	Relative permittivity	
ε_0	Vacuum permittivity	8.854×10^{-12} F/m
μ	Relative permeability	
μ_0	Vacuum permeability	$4\pi \times 10^{-7}$ H/m
c	Speed of light in vacuum	299792458 m/s
t	Time	s
θ	Angle	rad or °
$\mathbf{E}$	Electric field vector	V/m
$\mathbf{H}$	Magnetizing field vector	A/m
$\mathbf{D}$	Electric displacement field vector	C/m^2
$\mathbf{B}$	Magnetic field vector	T
$\mathbf{J}_f$	Free current density vector	A/m^2
$\mathbf{P}$	Polarization vector	C/m^2
r	Spatial resolution	m
a	Surface periodicity	m^{-1}
Δ	Surface roughness (root-mean-square)	m
d_1, d_2	Thickness	m
f	Filling fraction	
L	Magnetic inductance	H
C	Capacitance	F
R	Resistance	Ω
ρ	Resistivity	$\Omega{\cdot}\text{m}$
Q	Quality factor	
ℓ	Split-ring resonator sidelength	m
d	Split-ring resonator gap width	m
w	Split-ring resonator gap length	m
h	Split-ring resonator height	m
Λ	Period	m
Φ	Phase correction	

Chapter 1

Introduction

The main topic of this PhD work is the fabrication of nanoscale plasmonic metamaterial structures. These structures can have a multitude of potential applications including the use in lab-on-a-chip systems. As a short introduction to the nomenclature, plasmonics refer to plasmons, which are collective charge density oscillations, metamaterials are engineered, periodic materials with sub-wavelength features and the term "lab-on-a-chip" refers to the integration of several lab functionalities into a single portable chip. Although, the emphasis has been on the fabrication aspects and challenges, thought have also been put into general integration requirements relevant for potential applications. This includes compatibility with down-stream processing, and bio-compatibility, making it suitable for a wide range of bio-applications.

Here, we have explored two different systems: the silver Near-Field SuperLens (NFSL) and localized gold plasmonic resonators. The NFSL enables "diffraction-free" sub-wavelength resolution imaging in the near-field whereas the resonators give rise to an artificial magnetism where the effective permeability μ_{eff} can approach negative values. In terms of applications, the superlens may be used in surface enhanced spectroscopy and the resonators may be used for refractometric sensing.

The research time has been evenly distributed between the two research activities but the progress has been very different. This is primarily because whereas the superlens is very challenging fabrication-wise, requiring a great amount of optimization and running the fabrication equipment to the limit, the fabrication of the resonators is well within machine specs. For the latter project, the less focus on fabrication has allowed more time for the physics and testing new ideas rather than process optimization.

Note that the discussion of superlenses in this thesis is restricted to lenses operating in the near-field. There are other types on plasmonic based lenses including far-field superlenses in the literature, see e.g. [2] for details. However, they are not within the scope of this work and have therefore been left out.

1.1   Near-field superlens

The term superlens refers to a lens that enables a resolution better than the diffraction limit, which is an inherent limitation of conventional optical systems. The improved performance of the superlens relies on the excitation of surface plasmons, collective charge oscillations at the interface between two materials that fulfill the condition $\varepsilon_1(\lambda)=-\varepsilon_2(\lambda)$. In the book of Maier this is referred to as the Frölich condition [3]. Dielectric and metals are commonly employed as the constituent materials.

Research in near-field silver superlenses have primarily focused on photolithographic demonstrations of resolving powers beyond the diffraction limit of the incident light [2], see Fig. 1.1(a). Here, the NFSL is placed in between the mask and the photoresist, transmitting both evanescent fields, which include the finer image details, and the propagating fields to the photoresist. In conventional optical imaging the evanescent fields are damped out effectively limiting the resolution to about half the wavelength. By using a NFSL gratings with a period down to 60 nm have been resolved in a negative photoresist [4].

Other potential applications include remote surface enhanced spectroscopy of biomolecules such as proteins where an NFSL is combined with e.g. Surface Enhanced Raman Scattering (SERS), see Fig. 1.1(b). A SERS substrate provides local field enhancement to the Raman scattering process, amplifying the scattered intensity signal. The NFSL transmits the enhanced field to the objects of interest spatially separating the metal surface and the biomolecules. This prevents undesirable structural or functional changes such as denaturation of proteins [5] or alter the surface properties by e.g. influencing the anti-binding properties of the molecules to other molecules or prevent binding at specific downstream sites.
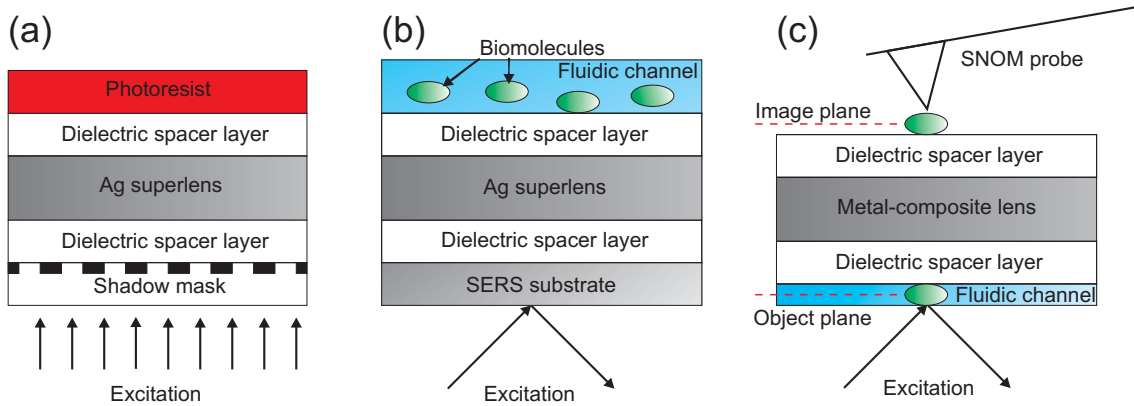
Figure 1.1: Applications of a near-field superlens. (a) Schematic of a silver NFSL enhancing the performance of photolithography beyond the diffraction limit. (b) Remote surface enhanced spectroscopy of biomolecules using a NFSL and a SERS substrate. (c) Remote, non-invasive probing of biomolecules using a metal-dielectric NFSL in combination with a SNOM.

An example of a long term goal is to use the NFSL for imaging of biomolecules with sub-

wavelength resolution, see Fig. 1.1(c). Such resolution is usually restricted to other near-field techniques such as a Scanning Near-field Optical Microscope (SNOM). Unfortunately, due the close proximity of the probes to the specism samples, there is a significant risk of perturbing the objects of interest. The idea is to insert a metal-dielectric superlens in between the biomolecules and the near-field probe. Instead of measuring directly on the biomolecules, the near-field probe measures on the image created by the superlens enabling remote, non-invasive imaging. A metal-dielectric composite superlens enables tuning of the operating frequency in response to the dielectric filling factor. This widens the tuning range compared to an Ag superlens making it easier to match the wavelength of the SNOM. However, composite materials can suffer from severe losses precluding their use for some plasmonic applications [6].

In this project, superlensing is demonstrated through photolithography [Fig. 1.1(a)]. By carefully choosing the constituent materials in terms of biocompatibility and chemical resistance towards down-stream processing, the superlens can be integrated into a fluidic platform at a later stage. This allows the superlens to potentially be used for surface enhanced spectroscopy and sub-wavelength imaging of biomolecules [Fig. 1.1(b)+(c)].

1.2 Refractometric label-free sensing

Label-free sensing is an attractive technique because it enables the objects of interest to be detected in their natural form. The labeling process can be both time consuming and can constitute a potential risk of perturbing the system such as in fluorescent labeling. Refractometry is a qualitative measurement technique to detect chemical changes that alters the refractive index from n to $n + \Delta n$. The consequent wavelength shift $\Delta \lambda$ can be detected by monitoring the spectral position of a resonance in e.g. a transmission spectrum. The wavelength shift per Refractive Index Unit (RIU), $\Delta \lambda / \Delta n$ is also termed the sensitivity. From perturbation theory, the sensitivity can be defined as [7]

$$\frac{\Delta \lambda}{\Delta n} = f \times \frac{\lambda}{n} \tag{1.1}$$

where f is the filling fraction determining the relative field intensity that overlaps with the cladding material. Consequently, (1-f) is the relative field intensity overlap with the substrate.

The performance of a refractometric sensor is characterized by the detection limit $\Delta n_{\min} = \sigma_{\mathrm{SN}} / (\Delta \lambda / \Delta n)$ where σ_{SN} is the transduction signal noise [8]. A closely related performance parameter is the Figure-Of-Merit (FOM) [9]

$$\mathrm{FOM} = \frac{|\Delta \lambda / \Delta n|}{\delta \lambda} \tag{1.2}$$

which favors a large sensitivity $\Delta \lambda / \Delta n$ and a narrow resonance linewidth $\delta \lambda$. Whereas the FOM solely describes the resonator characteristics, the detection limit takes the transduction i.e. the measurement setup into account. The FOM and the detection limit nicely supplement each other since the combination of sensitivity, transduction loss and linewidth

ultimately determines the overall sensor performance. To illustrate this point two reso-
nances with the same sensitivity but different linewidths are plotted in Fig. 1.2(a) where
the loss is zero and in Fig. 1.2(b) with moderate transduction loss.
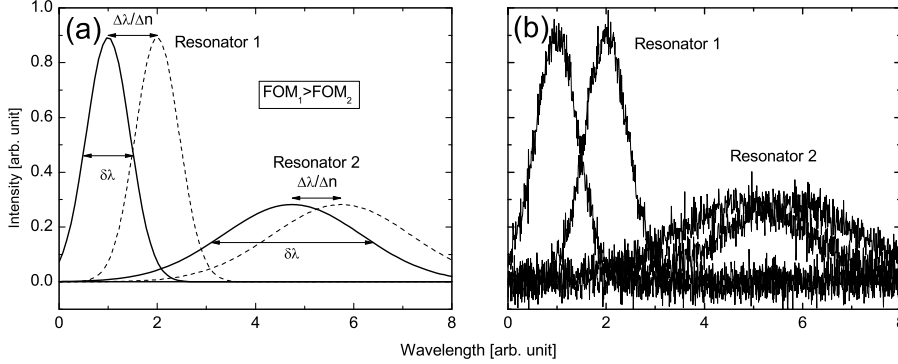
Figure 1.2: Two Gaussian shaped resonances exhibiting the same sensitivity but different
linewidths. (a) The ideal lossless case. (b) Introducing moderate white noise to mimic the
transduction noise of an actual measurement.

Despite the large difference in linewidth, the shift of both resonances are clearly ob-
servable in the lossless case. However, by introducing transduction losses, it becomes
increasingly difficult to distinguish the two peaks of resonance 2, and their spectral po-
sition. At this noise level, the two peaks of resonance 1 are still clearly distinguishable
emphasizing the importance of the linewidth in real measurements, and highlighting the
need to use both the FOM and the detection limit as performance parameters when com-
paring sensors.

Various optical structures have been investigated the past decade for label-free re-
fractometric detection including surface plasmon resonance sensors, interferometer-based
sensors and photonic crystal based sensors [8]. Whereas some techniques are still at the
research stage others have turned into commercial products [10, 11]. Localized plasmonic
based sensors are still in the research stage. Their sensor potential has often been debated,
and to some extent tested experimentally, see e.g. [12, 13]. We investigate their refracto-
metric sensors potential through a model system consisting of U-shaped gold Split-Ring
Resonators (SRRs). The nanometer-sized split-ring resonators operate at telecommuni-
cation wavelengths. At conceptual illustration of a potential SRR-based refractometric
sensor integrated into a microfluidic channel is given in Fig. 1.3.

In this project we look at the potential of SRR's-based sensors and localized plasmonic
sensors in general.

1.3 Thesis outline

This thesis consists of a general introduction to the fields of near-field silver superlenses
and gold split-ring resonators in addition to a list of five peer-review journal papers. Chap-
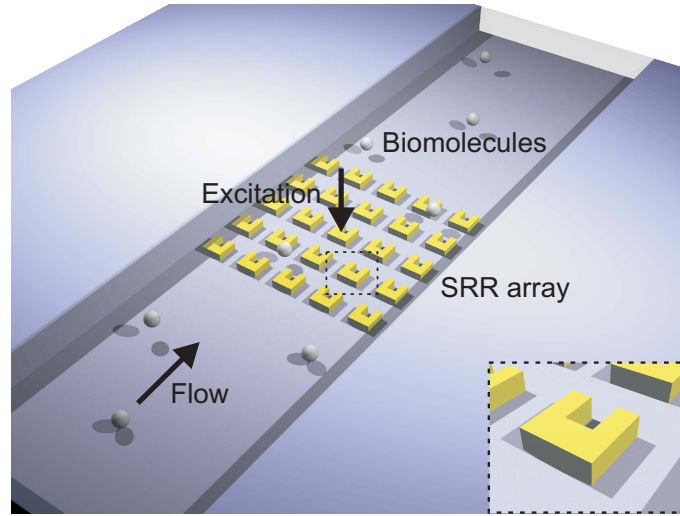
Figure 1.3: Conceptual drawing of a U-shaped split-ring resonator array integrated into a microfluidic channel to detect a refractive index change induced by biomolecules in the fluid. The excitation light induces fields in the SRR that overlap with the surrounding materials making the structure sensitive to refractive index changes of the fluid. The inset is a close-up of an individual split-ring resonator.

ter 2-5 comprises the introduction part whereas chapter 6 is devoted to a description of the articles. The articles are attached to Appendix A.

Chapter 2 - Background
To understand the superlens theory, the very basic theory of conventional optical microscopy and limitations is reviewed. After explaining the basic concepts of superlensing, the theory of split-ring resonators is introduced with emphasis on resonance tuning, the fields arising from the light excitation, and the losses that limits the sensor performance.

Chapter 3 - State-of-the-art
A review of the experimental results for a flat slab silver superlens are given. Then recently published results on split-ring resonators with particular focus on the sensor aspect. Finally, two alternative state-of-the-art refractometric sensor methods are described.

Chapter 4 - Hypothesis
The scope of this Ph.D. work is outlined.

Chapter 5 - Fabrication
The fabrication technique Electron Beam Lithography (EBL) is briefly described. EBL is central for both the superlens and the SRR project. The chapter ends by a discussion of metal and dielectric fabrication materials employed in the work.

Chapter 6 - Work summary
The content of the five published peer-review articles is summarized. The results are discussed, and compared to state-of-the-art techniques.

Chapter 7 - Conclusion & outlook
The thesis ends with concluding remarks and outlook on both the superlens and the SRR projects.

Appendix A
Publications submitted as part of the Ph.D. thesis.

Appendix B
Full list of publications.

Chapter 2

Background

This chapter revises the basic concepts of silver near-field superlenses and gold split-ring resonators. To understand near-field superlenses, it is relevant first to review the fundamentals of conventional optical imaging and describe the limitations of such systems. The foundation of metamaterials is then explained leading to split-ring resonator structures with emphasis on an analytical description, light induced fields and loss sources relevant for sensing applications.

2.1 Imaging

2.1.1 Conventional imaging system

There exists a large variety of optical imaging systems with vastly different complexities. From a single lens to microscopes consisting of multiple lenses, apertures and other optical components. The single most important component of an imaging system is the lens. A lens is typically made of an optically dense material such as glass with a refractive index n=1.5. When an incident wavefront propagating in air hits the lens, it is delayed by an amount depending on the thickness of the lens, n, and the wavelength of the light λ. The wave thereby experiences a phase delay. Depending on whether the lens is convex or concave, the phase correction will either lead to a point of focus (converging wavefronts) or the wavefronts will diverge beyond the lens, respectively. [14]

Mutual to all optical systems is that the spatial resolution r, i.e. the minimum detectable distance between two closely spaced specimen points, is limited by a number of factors. This includes aberrations of the optical components and alignment errors. For a perfect aberration-free imaging system, the ultimate resolution is determined by diffraction. Diffraction is a consequence of interference due to the wave-behavior of light, and is a limiting factor of any wave-dependent imaging system. Since most imaging systems are not perfect, the diffraction limit is the systems theoretical limit and it is determined by three system characteristics: the wavelength λ, the refractive index n between the objective and the lens, and the angular aperture half angle θ of the light cone captured by the objective, see Fig. 2.1.
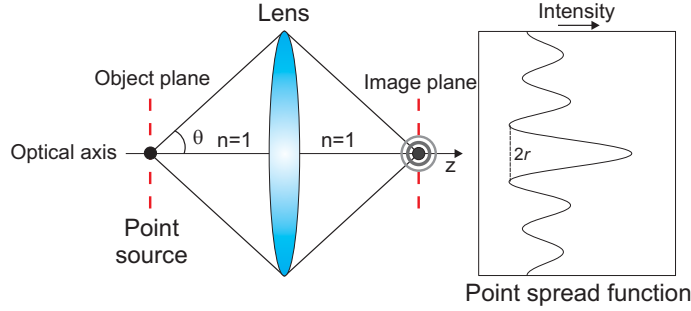
Figure 2.1: Imaging of a point source via a single convex lens with a numerical aperture equaling sinθ. The image forms an intensity distribution that can be described by a point spread function with radius r.

The diffraction limited spatial resolution for a circular aperture is defined as [15]

$$r = 0.61 \frac{\lambda}{n \sin\theta} \tag{2.1}$$

where $n \sin\theta$=NA (Numerical Aperture). The numerical aperture is an indicator used for objectives to illustrate their light gathering abilities and consequently their resolution potential. Eq. (2.1) is known as the Rayleigh criterion with r corresponding to the radius of a Point Spread Function (PSF). A point spread function represents the image of a point source. It is the overlapping of two point spread functions and whether these two distributions can be distinguished that determines the spatial resolution. By examining Eq. (2.1), it becomes apparent that the resolution is directly proportional to the wavelength and the refractive index. For optical microscopy the wavelength can be lowered to around 400 nm, which is the lower limit of the visible spectrum. The refractive index can be changed by substituting air (n_{air}=1) with immersion oil (n_{oil}=1.5), thereby collecting more light through the lens and gaining a factor of 1.5 in resolution. Finally the angular aperture can be as high as 72° corresponding to sinθ=0.95. The practical resolution of an optical system is around 200 nm for a periodic grating structures [16].

A related concept is the spatial frequency k, which is the number of structural repetitions or periods within a certain length scale. Fig. 2.2 illustrates the effect of increasing the spatial frequency on the contrast M. The objects are resolved for both spatial frequencies but there is a large contrast difference. The frequency at which the contrast is zero, hence where the image is homogeneously grey, is called the cut-off frequency k_c=2NA/λ. [16]

Eq. (2.1) states the ultimate limit for a conventional optical imaging system determined by light interference, and because these systems are only able to transmit the propagating waves. Propagating waves are waves with low spatial frequencies k. High spatial frequency waves that include the finer details of the objects can not be resolved by a conventional optical system. For a dielectric material such as glass or air ($\varepsilon > 0$ and $\mu > 0$), the low k waves propagate through the medium. These propagating waves can be described
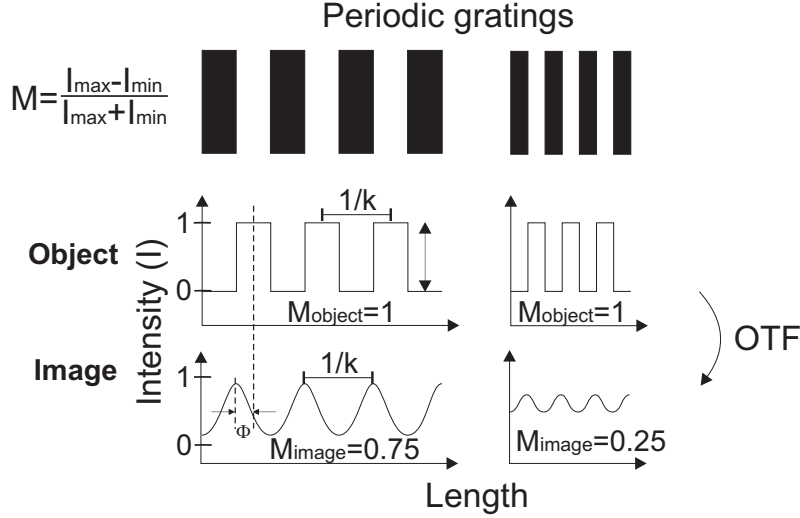
Figure 2.2: Intensity plots of two grey-scale periodic gratings with different spatial frequencies. The black and white bars represent intensities of zero or one, respectively. Hence, in both cases the object has a contrast $M_{\text{object}}=1$. The optical imaging system can be represented by an Optical Transfer Function (OTF) that encompasses both an amplitude and a phase correction Φ. The resulting image resembles a sinusoidal intensity distribution with a contrast dependent on the spatial frequency.

by the wave numbers $k_z = \sqrt{\omega^2 c^{-2} - k_x^2 - k_y^2}$ where $\omega^2 c^{-2} > k_x^2 + k_y^2$, assuming plane waves $E(\mathbf{r}, t) = E_0 \exp(i\mathbf{k} \cdot \mathbf{r} - i\omega t)$, and propagation in the +z-direction. For the high k waves, $\omega^2 c^{-2} < k_x^2 + k_y^2$ leads to $k_z = i\sqrt{k_x^2 + k_y^2 - \omega^2 c^{-2}}$, which describes an exponentially decaying wave. These waves are often referred to as evanescent waves. For a conventional optical system the evanescent waves decay before reaching the image plane and they typically do not contribute to the image. [17]

2.1.2 Contrast and resolution enhancement

In standard bright-field microscopy, the mechanism that creates contrast in a image is the absorption of light by the sample. There are various microscopy techniques that can enhance the contrast of a specific sample including dark-field microscopy that relies on light scattering and phase contrast microscopy, which relies on interference. Nevertheless, all techniques still have to abide to Eq. (2.1) and therefore do not offer a better resolution. The same can be said for fluorescence microscopy where light emitting objects smaller than r can be localized e.g. 10 nm Quantum Dots (QDs). It is the variations in fluorescent intensity that creates contrast in the image. If the objects of interest are not sufficiently auto-fluorescent to be distinguished from the background, then the specimens have to be labeled with a fluorescent dye, the so-called fluorophores. Fluorescent microscopy is great for determining the position of nanoscale objects but does not provide any finer details

and can only distinguish objects that are further than r apart [18].

There are two apparent alternatives to enhance resolution. Either to substitute the photons with particles that have a shorter wavelength such as electrons or to use near-field techniques that capture the evanescent fields as well. Fig. 2.3 summarizes various spectroscopy techniques according to their spatial resolution.
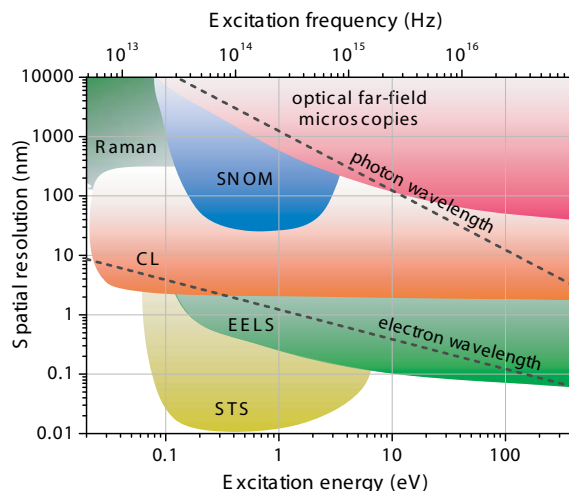
Figure 2.3: Overview of spectroscopy techniques arranged according to energy and spatial resolution. The methods include scanning probe techniques such as SNOM, and STS, electron based techniques such as EELS and CL, Raman spectroscopy and optical far-field microscopy. The dashed curves represent the wavelength of photons and electrons. Reproduced and modified from [19].

The de Broglie wavelength of an electron is a factor of 10-100 smaller than the corresponding wavelength of light at a given energy. The performance of electron based techniques including Electron Energy Loss Spectroscopy (EELS) and CathodoLuminescence (CL) depends largely on the conductivity of the sample but the resolution should still be better or comparable to optical microscopy [20]. In most bio-applications the objects of interest are only poorly conducting effectively ruling out electron based imaging techniques unless the biomolecules are in some way coated. However, a conductive coating effectively alters the biomolecules and they are no longer measurable in their natural form. Near-field techniques such as Scanning Tunneling Spectroscopy (STS) or scanning near-optical microscopy provide sub-wavelength resolution. Unfortunately, STS is restricted to metals as well. This is not a limitation of the SNOM technique, which works by collecting the samples' near-field through a hole in the tip of a metal coated probe. The probe is placed within a few nanometers of the sample and raster scanned across the sample to form the image. Hence, unlike a lens, a SNOM does not project the whole image and the scanning is typically rather slow. Furthermore, the measurements are often invasive slightly modifying or damaging the sample during scanning due to the close proximity of the SNOM probe [21, 22].

2.1.3 Negative index media

An alternative approach to obtain sub-wavelength resolution was proposed by Pendry in 2000 [17]. The idea of his theoretical paper was to make a lens out of Negative Index Material (NIM). This lens should be able to transmit both the propagating and evanescent waves to the image plane, resulting in a diffraction-free image. Pendry's ideas elaborated on the work by Veselago [23] who already in 1968 had speculated what the optical implications of a material with simultaneously $\varepsilon < 0$ and $\mu < 0$ would be. Among many interesting observations, Veselago demonstrated the focusing capabilities of a flat NIM slab by applying Snell's law of refraction, see Fig. 2.4(a). Due to the negative index, the NIM based lens does not need to be spherical to focus the light. In fact the light is focused to a spot inside the NIM as well as at a distance z beyond the NIM.
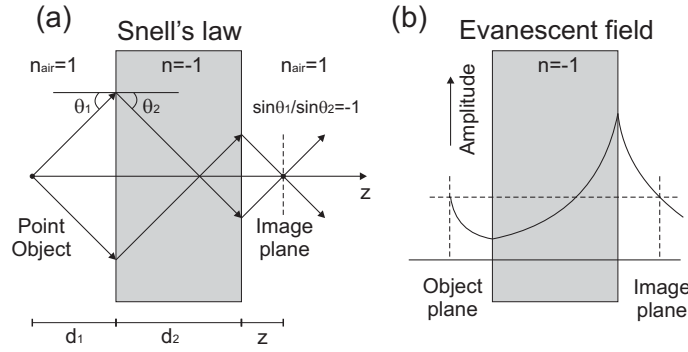
Figure 2.4: (a) Ray diagram of the light propagating through a flat slab of NIM with thickness d_2. The light is emitted from a point source a distance d_1 away from the slab. According to Snell's law, the light is refracted at a negative angle relative to the surface normal and is refocused at a distance $z = d_2 - d_1$ beyond the slab. (b) A slab of NIM restores the evanescent field amplitude of the object to the image plane.

Another relevant aspect for imaging is the negative phase velocity inside the NIM slab. Hence, the NIM is able to rewind the phase back to its original state when the light was first emitted by the source, whereby $\Phi=0$ (Fig. 2.2). When $\varepsilon_2=-\varepsilon_1$ and $\mu_2=-\mu_1$, a NIM does not only correct the phase but also amplifies the evanescent waves [Fig. 2.4(b)]. Consequently, both propagating and evanescent waves can reach the image plane and contribute to the image. The restoration of the evanescent waves paves the way for sub-wavelength imaging since both high and low spatial frequencies are represented in the image. Unfortunately, materials with simultaneous $\varepsilon < 0$ and $\mu < 0$ do not naturally occur.

2.1.4 Near-field superlens

Pendry also proposed that a material with either $\varepsilon < 0$ or $\mu < 0$ can be used as a sub-wavelength lens. However, there are two important restrictions. Firstly, the evanescent field amplification only applies to one of the orthogonal polarizations directions: Transverse Magnetic (TM) or Transverse Electric (TE). Secondly, the lens is restricted to the

near-field so that the distances between object, lens, and image plane have to be smaller than the wavelength. Fortunately $\varepsilon < 0$ can be readily obtained in a number of metals at optical frequencies and therefore Pendry suggested a lens consisting of a flat silver (ε_m) slab surrounded by air, ε_d, where $\varepsilon_d = -\varepsilon_m$ at λ_0=356 nm, see Fig 2.5(a).
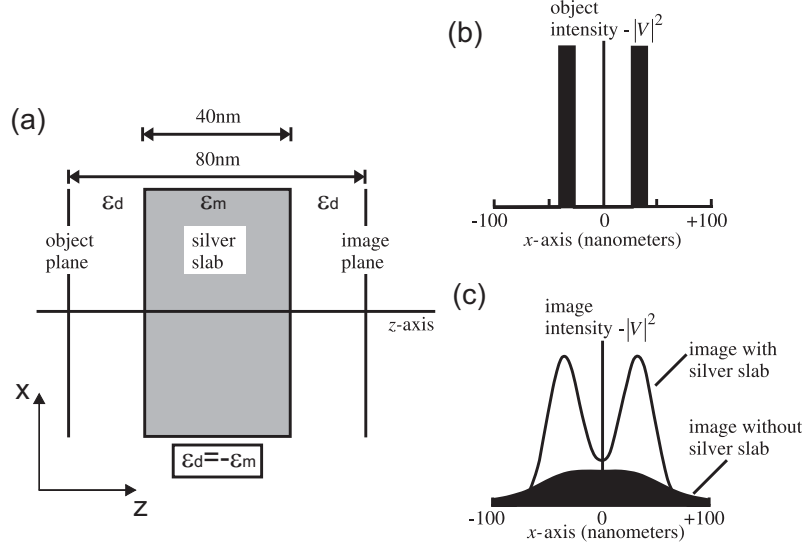
Figure 2.5: (a) Sub-wavelength near-field lens design consisting of a flat silver slab surrounded by dielectric where ε_d=-ε_m. (b) The quasi-electrostatic potential in the object plane. (c) The image of the electrostatic potential through a lens design as described in (a), and without the silver slab, hence a purely dielectric lens. Adopted and modified from [17].

The reason why the lens only works in the near-field is due to the requirement that the electric and magnetic fields have to be decoupled. Otherwise both the material parameters ε and μ have to be negative. This in turn requires that the quasistatic limit applies. In this limit the electric and magnetic fields decouple in Maxwells equations as the partial derivatives $\partial/\partial t$ go to zero, see Eq. (2.2) and Eq. (2.3)

$$\nabla \times \mathbf{E} = -\frac{\partial \mathbf{B}}{\partial t} \Rightarrow \nabla \times \mathbf{E} = 0 \tag{2.2}$$

$$\nabla \times \mathbf{H} = \mathbf{J}_f + \frac{\partial \mathbf{D}}{\partial t} \Rightarrow \nabla \times \mathbf{H} = \mathbf{J}_f \tag{2.3}$$

where $\mathbf{D} = \varepsilon_0\mathbf{E} + \mathbf{P}$ and $\mathbf{H} = 1/\mu_0\mathbf{B} - \mathbf{M}$. $\mathbf{D}$ is the electric displacement field, $\mathbf{E}$ is the electric field, $\mathbf{B}$ is the magnetic field, $\mathbf{H}$ is the magnitizing field, $\mathbf{J}_f$ is the free current density, ε_0 is the permittivity of vacuum, $\mathbf{P}$ is the polarization, μ_0 is the permeability, and $\mathbf{M}$ is the magnetization. Specifically, the evanescent field of a TM wave can be amplified in a medium with $\varepsilon < 0$ while a TE evanescent field can be amplified in a $\mu < 0$ medium.

Whereas a NIM ensures perfect imaging for an arbitrary polarization [24], a near-field lens can only restore the polarization components along a given axis.

Pendry found that the requirement ε_d=-ε_m is exactly the condition for surface plasmons to exist at the boundary between the metal and the dielectric and concluded that there must be a link between the excitation of surface plasmons and the evanescent field enhancement. He theoretically demonstrated that a flat slab of silver surrounded by dielectric material can focus light to a sub-wavelength spot, if the spatial frequencies of the light and surface plasmon match, Fig. 2.5(b) and (c). However, the resistive loss of the metal precludes a 1:1 representation of the object in the image plane.

Pendrys proposed flat lens has later been termed a near-field superlens due to the sub-wavelength resolution potential in the near-field. There are other types of plasmonic lenses including hyperlenses and far-field superlens that also offer sub-wavelength resolution but in the far-field by converting the evanescent waves into propagating waves. The design complexity, however, largely surpasses the NFSL.

2.1.5   Superlens resolution

The resolution enhancement R of a near-field superlens relative to a conventional optical imaging system, was estimated by Smith *et al.* [24] as

$$R = \frac{1}{2\pi}\ln\left(\frac{\lambda^2}{a^2\Delta^4}\right)\frac{\lambda}{d_2} \tag{2.4}$$

where a is the surface periodicity [m^{-1}], Δ is the modulation (rms roughness) and d_2 is the thickness of the metal slab. The resolution enhancement is inversely proportional to the slab thickness and for resolution enhancement, $\ln(\lambda^2/a^2\Delta^4)\gtrsim1$ is typically required. Obviously Δ is the most significant parameter. Δ should preferably be lower than 1 nm rms for both spacer and Ag surfaces since the spacer roughness largely influences the metal roughness [1]. However, a is also important since a surface plasmon (k_x) on a surface with $a \sim k_x$ will be highly dissipative rendering it impossible for the corresponding evanescent field to be sufficiently enhanced [24]. Both a, Δ, and d_2 contribute significantly to the cut-off frequency k_c.

2.2   Photonic metamaterials

The unusual optical properties of negative index media and their potential applications [17, 25] have catapulted the interest in such materials. Negative index materials do not occur naturally and the simplest engineering approach would be metal-ferromagnetic alloys, see Fig. 2.6(a). Unfortunately, metals have $\varepsilon < 0$ at terahertz frequencies whereas ferromagnetic materials provide $\mu < 0$ up to the gigahertz range. The frequency mismatch means that ε and μ cannot be negative in a metal-ferromagnetic alloy, simultaneously. Since Pendry *et al.* in 1999 [26] showed that $\mu < 0$ can be obtained in metal-dielectric sub-wavelength structures, there has been a great interest in these so-called metamaterials for realizing true negative index media.
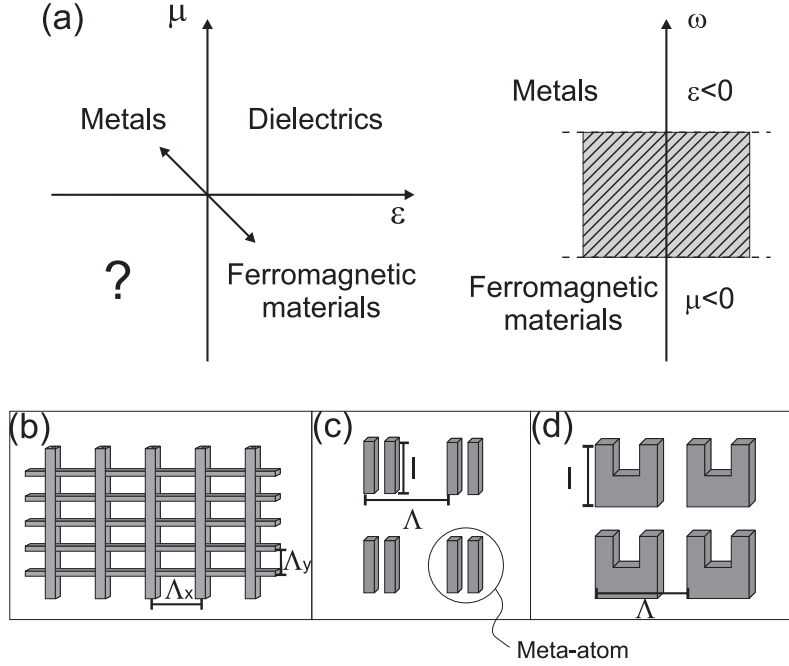
Figure 2.6: (a) Permittivity ε and permeability μ diagram including relevant material classes. The axis to the right illustrate the ranges $\varepsilon < 0$ for metals and $\mu < 0$ for ferromagnetic materials as a function of frequency ω. (b) Fish-net structure. (c) Double rod structure. (d) Split-ring resonators. The periodicity Λ is for all structures much smaller than the wavelength of light λ.

The common definition of metamaterials is that they are artificially structured, composite materials which attain their electromagnetic properties from their mesoscopic unit cell rather than the constituent materials [27]. Metamaterials are typically build up of periodic metal nano-structures, the so-called meta-atoms [Fig. 2.6(b)], surrounded by dielectric material where all characteristic length scales such as side-length ℓ and period Λ are substantially smaller than the wavelength λ. Their electromagnetic response stems from the excitation of structural resonances in the metal structures caused by moving charges [26]. There are a few different types of metamaterials including rods, fish-net, and different types of split-ring structures [28], see fig. 2.6(b)-(d) for example structures. The simplicity of the one-piece split-ring resonator combined with a simple analytic description has made the SRR a central metamaterial structure that exhibits $\mu < 0$ in the spectral vicinity of the resonance [29].

2.2.1   Split-ring resonators

In 1999 Pendry *et al.* [26] presented several examples of sub-wavelength, metal structures relying on internal circuit resonances to provide an effective negative permeability μ_{eff}. In terms of fabrication complexity, the simplest structures proposed were arrays of planar

split-ring resonators. By providing a magnetic field normal to the plane of the SRR array i.e. by excitation at grazing angles, the circuit resonance can be excited whereby the structure inhibits light propagation in a narrow band around the resonance. Different interpretations have been applied to explain the transmission stop band. Some suggest it is caused by large values of the permeability in the vicinity of the resonance while others suggest it is related to the induced circulating current within the ring that produces an artificial out-of-plane magnetic dipole that can oppose the incident field [30, 31].

In 2002 Balmaz *et al.* [32] demonstrated that a SRR can also be excited by an external electric field. The **E**-field excitation is weaker than the **B**-field excitation in terms of signal strength but provides an opportunity to excite the SRR at normal incidence. The only requirement is that the light polarization is perpendicular to the SRR arms to create an asymmetric charge distribution, which induces the circulating current. If the light is polarized parallel to the arms, current will only oscillate within the two arms and therefore the SRR does not produce a magnetic dipole but an in-plane electric dipole [33]. Finally, SRRs can also be electrically excited [30].

The SRR fundamental resonance is caused by internal capacitance and inductance. The strong circuit analogy has paved the way for an analytical inductance-capacitance (LC) model description where the resonance frequency is given as

$$\omega_0 = \frac{1}{\sqrt{LC}} \tag{2.5}$$

In the simplest approximation the two arms of the SRR mimicks a parallel plate capacitor and the actual split-ring imitates a single loop of a coil given rise to the systems inductance, see Fig. 2.7.
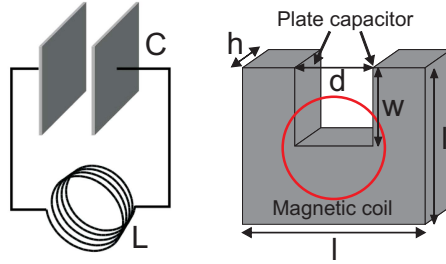
Figure 2.7: The U-shaped SRR resembling an LC circuit consisting of two parallel plates with capacitance C and a magnetic coil with inductance L. Relevant geometrical parameters are: the sidelength ℓ, the gap width d, the gap length w, and the height h.

For the U-shaped SRR depicted here

$$C = \varepsilon_0 \frac{wh}{d} \ , \ L = \mu_0 \frac{\ell \times \ell}{h} \tag{2.6}$$

Inserting L and C into Eq. 2.5 yields

$$\omega_0 = \frac{c}{l}\sqrt{\frac{d}{w}} \qquad\qquad (2.7)$$

where $c = 1/\sqrt{\varepsilon_0\mu_0}$. L is the ring inductance while C is the gap capacitance. The resonance frequency scales with the sidelength ℓ related to the inductance and the slit ratio d/w coming from the capacitance. Surprisingly ω_0 is independent of the height h. Numerical and experimental investigations have revealed that the resonance is height dependent [34, 35] but this is not accounted for in this simple model. Variations in the dielectric environment is also left out of the equation.

The linear scaling of Eq. (2.7) breaks down at high frequencies. Klein *et al.* [36] attributed this to the increasing importance of the kinetic energy of the conduction electrons. Therefore more advanced models have been proposed to describe resonances at high frequencies. These include an additional kinetic inductance term to account for the electron kinetic energy [37] and an additional capacitance term to describe contributions from local **E**-fields inside the metal [38] or at its surfaces apart from the gap region [39].

Eq. (2.7) describes the ground mode resonance of a single isolated U-shaped split-ring resonator. However, also higher order modes exist as seen in Fig. 2.8(a). In most cases the SRR sits in a vast array with many other SRRs. The light induced **E** and **B**-fields in a SRR affect neighboring SRRs, see Fig. 2.8(b). The interaction results in a resonance shift and a widening of the resonance due to coupling induced losses R_{coup} [40].
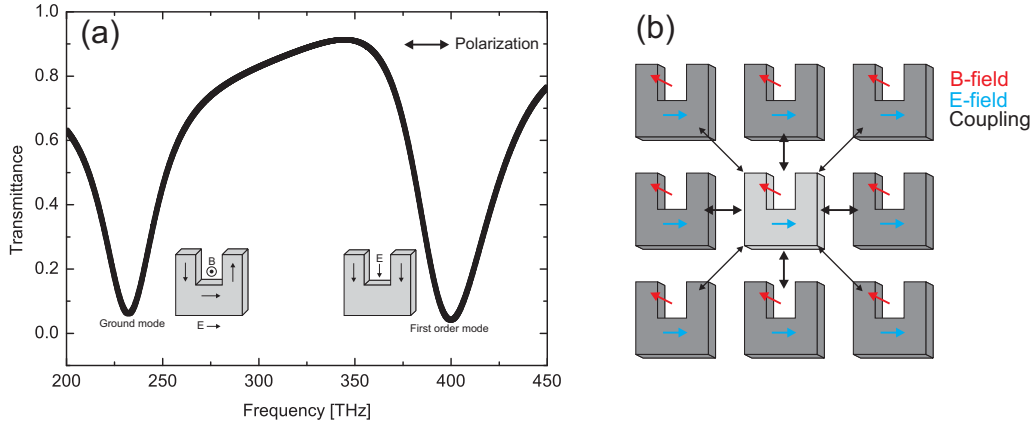
Figure 2.8: (a) Simulated transmission spectra including schematic illustration of the internal current flow for the ground and first order SRR resonances. For the ground mode a circulating current creates an out-of-plane magnetic dipole and an in-plane electric dipole. The current flow is restricted to the arms for the first order mode creating an in-plane electric dipole. (b) The light induced **E**-fields (blue) and **B**-fields (red) of the individual SRRs for the ground mode resonance. The proximity of the array leads to coupling (black) between neighboring SRRs.

Extending the LC-model to an RLC-model, a resistance R is introduced to describe the total damping but which leaves the resonance nearly invariant [41]. The quality factor

(Q) is often used to describe the energy dissipation and thereby the performance of a resonating system. For an RLC-circuit the Q-factor is defined in Eq. (2.8).

$$Q = \frac{\omega_0}{\Delta\omega} = \frac{1}{R}\sqrt{\frac{L}{C}} \tag{2.8}$$

where R is the total resistance. R consist of an internal, intrinsic ohmic resistance R_0, a radiation resistance R_{rad} stemming from the oscillating electric dipoles, a R_{inhom} describing the inhomogeneous broadening due to fabrication tolerances and finally R_{coup}. In order to narrow the resonance peak of a single SRR, losses should be minimized, and the ratio L/C should be large according to Eq. (2.8). Obviously, for sensing applications a narrow linewidth translates into a high figure-of-merit and a low detection limit, which in turn requires low losses.

Chapter 3

State-of-the-art

Recent developments in the field of near-field superlenses and split-ring resonator structures are summarized here. Some basic theoretical concepts are briefly reviewed but the main focus is on the experimental demonstrations, in order to give a good overview of the context of this Ph.D. work.

3.1 Plasmonic near-field superlens

In 2000 the theoretical foundation of the plasmonic based near-field superlens was established by Pendry *et al.* [17]. The lens consists of a silver slab surrounded by a dielectric material with $\varepsilon_{\mathrm{d}} = -\varepsilon_{\mathrm{m}}$. Negative refraction of light ensures focusing while surface plasmon excitation at the dielectric-metal interfaces amplifies the evanescent fields facilitating the finer image details to be resolved in the image plane. The lens is thereby able to image below the diffraction limit by transmitting both propagating and evanescent field components.

3.1.1 Precursors for NFSL

In 2001 the first experimental demonstration of negative refraction was presented by Shelby *et al.* [42]. Their metamaterial was built up of 2D periodic arrays of copper split-ring resonators and wires separated by a 0.25-mm thick fiber glass circuit board material. The SRRs produce a negative μ whereas the wires provide a negative ϵ. The boards were then assembled into an upright cubic 3D pattern, see Fig. 3.1(a), and the structure was cut into a prism for the beam deflection measurements. The measurements were conducted at microwave frequencies (8-12 GHz) and the transmitted intensity was collected at angles $\theta = \pm \pi/2$ within the beam plane, see Fig. 3.1(b)-(c). Whereas the teflon sample refracts the light in the expected positive direction, the metamaterial demonstrates negative refraction of light, thereby supporting the conclusions made by Veselago [23].

A step closer to the realization of a near-field superlens was taken in 2003 by Fang *et al.* [43, 44] who demonstrated growth of evanescent waves in nanometer thick silver layers. The surface roughness of the air/Ag interface was used as the coupling mechanism to optically excite surface plasmons at normal incidence, contrary to the traditional grating
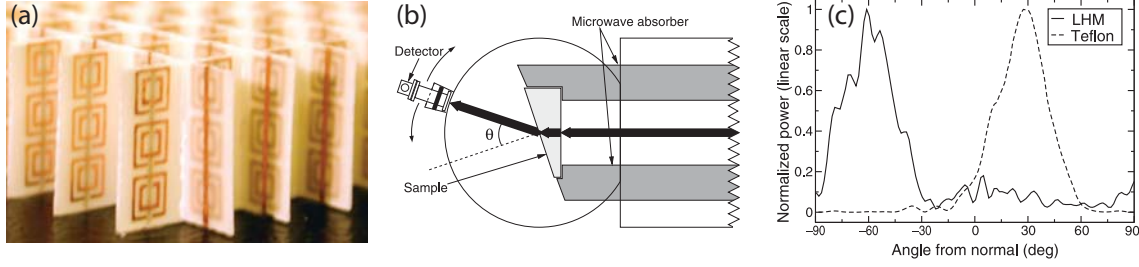
Figure 3.1: (a) 3D metamaterial cubic lattice consisting of split-ring resonators and wires on each side of a transparent circuit board material. (b) Experimental setup diagram for measuring the transmitted light intensity for angles $\theta=\pm\pi/2$. (c) The measurement results for a negative index material ("LHM") compared to a teflon reference. Adapted from [42].

or prism coupling schemes [3]. The silver was deposited onto the flat side of a glass prism, see Fig. 3.2(a). At the air/Ag interface some of the propagating waves are converted via scattering to evanescent waves described by a lateral wavevector k_x. The evanescent waves are transmitted through the silver and their amplification depends on whether $k_x \approx k_{sp}$, Fig. 3.2(b). Some of these evanescent waves are then converted back into propagating waves in the glass prism and recorded by a CCD array measuring the angle distribution near the surface-plasmon coupling angle θ_{sp}. Propagating waves transmitted directly through the silver, hence with small k_x, are blocked by a mask and therefore do not contribute to the image.

Fang observed that the range of amplified spectral frequencies strongly depends on how well the surface plasmon condition $\epsilon_{air}=-\epsilon_{Ag}$ is fulfilled. For $\epsilon_{Ag} \rightarrow -1$ the bandwidth of resolvable spatial frequencies increases. Also they noted that the amplification depends on the silver thickness since for thick silver layers the intrinsic loss of the silver starts to dominate [Fig. 3.2(c)].

3.1.2 Towards sub-diffraction resolution

In 2004 Melville *et al.* [45] tested the imaging properties of a flat silver slab. They employed a grating mask, a photolithographic readout scheme and characterized the exposed resist using an Atomic Force Microscope (AFM). The lens stack consisted of an EBL written 40 nm thick tungsten mask on glass, 60 nm Poly(Methyl Methacrylate) (PMMA) spacer layer, 120 nm Ag, and finally a 60 nm PMMA layer (60/120/60 configuration) that was brought into vacuum contact with a 50 nm resist layer on a silicon wafer, see Fig. 3.3(a). The first spacer layer was used to planarize the mask, reducing the surface roughness to 2 nm root-mean-square (rms) while the second layer sets the image plane at the PMMA/resist boundary. Using a I-line aligner ($\lambda_0=365$ nm), the Ag lens was compared to standard proximity lithography [Fig. 3.3(b)-(c)].

Whereas the standard lithography was unable to resolve 1 μm half-pitch ($\Lambda/2$) gratings due to diffraction, the silver lens slab was successful. Further exposures showed that
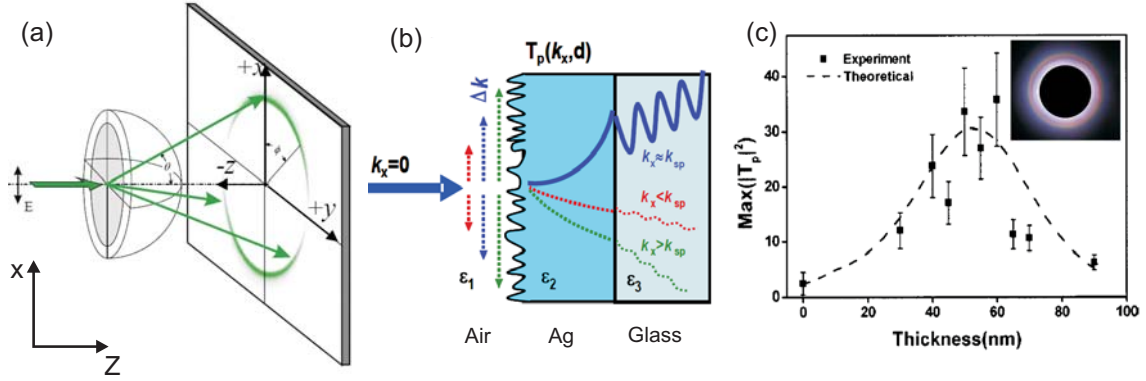
Figure 3.2: (a) Schematic illustration of the sample with a thin silver layer on the flat side of a glass prism. Normal incidence light polarized along the x-direction is scattered at the air/Ag boundary. A mask on the other side of the prism blocks light with small k_x vectors from reaching the screen (CCD array). (b) The light scattered at the air/Ag interface produce evanescent waves that can couple to surface plasmons and be amplified. Some of these amplified evanescent waves are converted into propagating waves at the Ag/glass-interface. (c) Transmissivity $|T_p|^2$ of the p-polarized evanescent field as a function of silver thickness. The inset shows the recorded image of a white light source creating a rainbow effect. Adapted from [43].

350 nm $\Lambda/2$ gratings could be resolved, which is on the order of the operating wavelength. Supported by finite-difference time domain (FDTD) simulations of the **E**-field intensity, Melville concluded that the silver lens is able to focus the light but that the layers chosen are too thick for sub-wavelength imaging.

Whether Melvilles's results could be linked to the superlens effect proposed by Pendry was later questioned [46]. Melville and co-workers answered the criticism [47] while continuing to refine their lens structure resolving 250 nm $\Lambda/2$ [48] in late 2004 by employing a asymmetric 40/80/26 PMMA/Ag/SiO2 structure with improved roughness (below 1 nm rms) to 72.5 nm $\Lambda/2$ [49] in early 2005 for a 25/50/10 PMMA/Ag/SiO2. For the latter structure they had also incorporated an anti reflection coating (ARC) layer in between the Si and resist to minimize reflections. Since the diffraction limit is $r \approx \lambda_0/2n$, this was the first real demonstration of sub-diffraction imaging using a near-field silver lens.

3.1.3 NFSL state-of-the-art

This resolution milestone was broken a month later by Fang *et al.* [1] demonstrating 60 nm $\Lambda/2$ resolution with a single stack structure. Their structure consisted of a focused ion beam written chrome mask on a quartz wafer, a 40 nm PMMA spacer layer, 35 nm Ag, 120 nm resist for recording the image, and the stack was exposed from the bottom using an I-line (365 nm) aligner, see Fig. 3.4(a).

For a grating structure only a single spatial frequency k_x of the evanescent field has
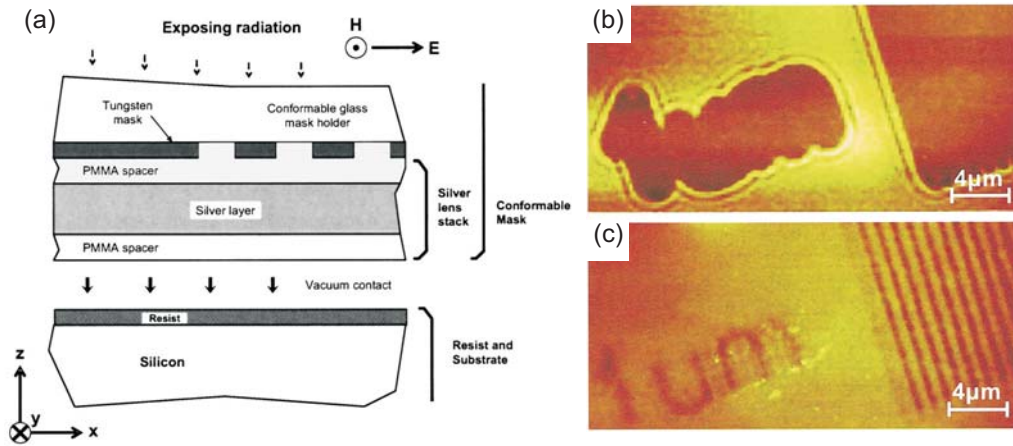
Figure 3.3: (a) Schematic illustration of the imaging setup comprising a mask/lens stack and a resist stack. The lens stack consists of a glass/tungsten mask, a planar silver lens and two PMMA spacer layers. The stack is brought into vacuum contact with a resist coated Si wafer and the combined structure is illuminated from the top at 365 nm. (b) AFM image of an exposed 1 μm grating structure using standard proximity lithography. (c) AFM image of an exposed 1 μm grating structure using the stack depicted in (a). Adapted from [45].
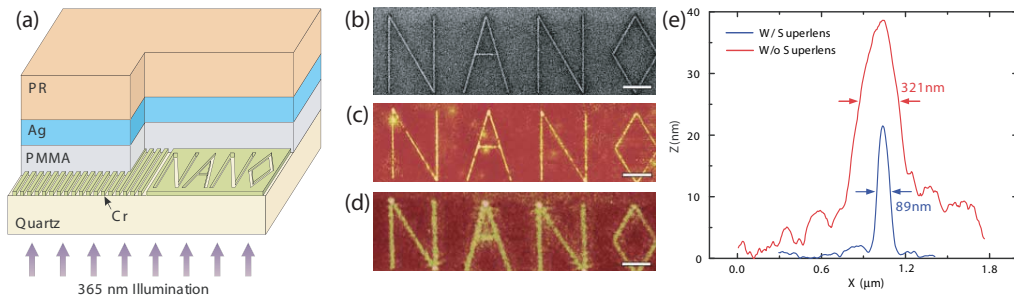
Figure 3.4: (a) The stack for the superlensing experiment consisting of a quartz/chrome mask, PMMA spacer layer, Ag, and a photoresist. The resist was exposed from below at λ_0=365 nm. (b) SEM image of the object. The linewidth is 40 nm. (c) AFM image of the exposed resist. (d) AFM image of a control structure where the Ag layer in (a) is replaced by PMMA. (e) Cross-sectional scan of the letter "A" for the superlens and control structure. Adapted from [1].

to be restored. For an arbitrary object a whole band of spatial frequencies have to be restored. Besides resolving the 60 nm $\Lambda/2$ gratings, Fang *et al.* tested their superlens on the arbitrary object "NANO", see Fig. 3.4(b)-(e). They observed a linewidth improvement from 321 nm to 89 nm compared to the control experiment. However, the lack of 1:1

reproduction demonstrated the limitations of their near-field superlens unable to restore the full bandwidth of k_x.

The resolution benchmark of the near-field superlens was further improved in 2010 by Chaturvedi *et al.* [4] resolving 30 nm $\Lambda/2$ gratings in a photoresist, see Fig. 3.5(b). The 40 nm mask modulations were planarized by NanoImprint Lithography (NIL) of a thick spacer layer using a flat Si stamp. Subsequently, the spacer layer was dry etched down to 6 nm in thickness. Then a 35-nm chrome layer with windows defined by photolithography, 1 nm germanium (Ge) to reduce the surface roughness of the subsequent 15 nm Ag layer to 0.8 nm rms, and a photoresist on top completes the stack, see Fig. 3.5(a). The exposure was done using an LED at λ_0=380 nm.
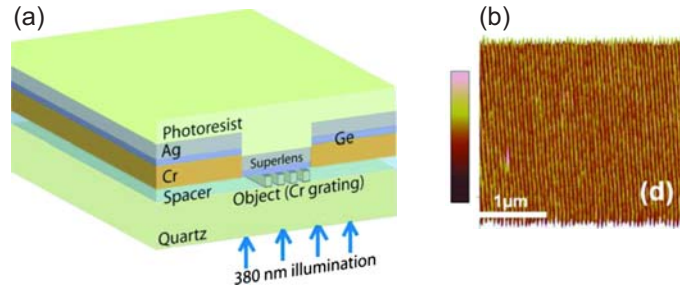
Figure 3.5: (a) Schematic illustration of the lens stack consisting of a quartz wafer with an embedded 30 nm $\Lambda/2$ chrome mask within a spacer layer. On top a Cr layer, a Ag layer, and finally the photoresist. The resist is exposed through the back side at λ_0=380 nm. (b) AFM image of the developed photoresist after exposure. Adapted from [4].

3.1.4   NFSL readout mechanism

A different read-out technique was introduced by Taubner *et al.* [50] using a scattering version of the scanning near-field optical microscope (s-SNOM) to probe the near-field light intensity directly at infrared frequencies. The superlens was operated in reflection with the s-SNOM providing the excitation around λ_0=11 μm and recording the amplitude and phase of the reflected signal. The stack consisted of circular holes in a 60 nm thick Au film, two 220 nm SiO_2 spacer layers, and the 440 nm SiC lens, see Fig. 3.6(a)-(b). Holes down to 540 nm were resolved resulting in $\lambda_0/20$ resolution [Fig. 3.6(c)-(d)]. A control experiment at λ_0=9.25 μm, hence where the plasmon condition is unfulfilled, showed no significant contrast [Fig. 3.6(e)].

3.2   Photonic metamaterials

As with the area of superlenses, it was a theoretical paper by Pendry *et al.* [26], which kick-started the field of metamaterials. In the past years photonic metamaterials have demonstrated a broad range of intriguing optical properties and potential applications including nanoscale light concentration and focusing in addition to miniaturization of
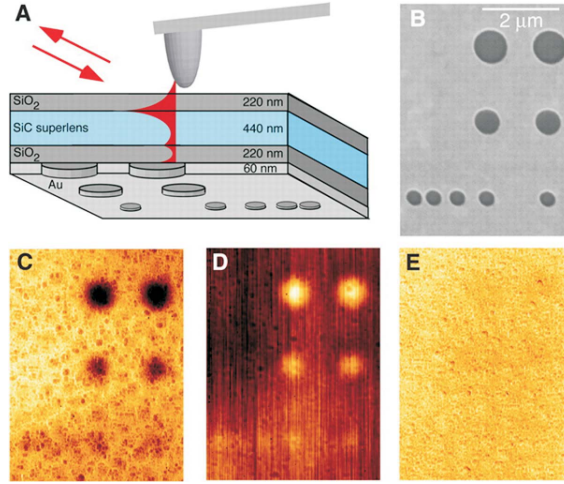
Figure 3.6: (a) The experimental setup showing the s-SNOM tip and the stack of Au holes, SiO$_2$ spacer layers, and the SiC lens. (b) SEM image of the different sized holes in the Au film. (c) Measured reflected amplitude. (d) Measured reflected phase contrast. (e) Control experiment at wavelength which is off the plasmons resonance. (λ_0=9.25). Adapted from [50].

devices such as antennas [51]. Fig. 3.7 summarizes the development for fishnet, rods and split-ring resonator structures towards visible wavelengths for the ground resonance mode. The following sections focus entirely on the split-ring resonator structure.

3.2.1   Split-ring resonators

The resonances of sub-wavelength metal structures are caused by internal capacitance and inductance [26]. For the single SRR geometry the capacitor is represented by the two arms forming the two plates of a parallel capacitor with capacitance C and the ring forms a single loop coil with inductance L. This leads to the well known LC circuit resonance, $\omega = 1/\sqrt{LC}$, which can be used to estimate the ground mode resonance frequency.

Well aware that the simple model has some shortcomings, attempts have been made to extend or refine the model e.g. for high aspect ratio SRR. Guo *et al.* [52] looked at the SRR as a folded wire and added a certain length δ to the wire length whereby the model accuracy improved when compared to experimentally observed resonances. Corrigan *et al.* [35] included the Indium-Tin-Oxide (ITO) adhesion layer when defining an effective permittivity ϵ_{eff} rather than just using the vacuum permittivity ϵ_0. They also derived more complex analytical expressions for L and C by modeling the ring structure as four connected sheets (L) and the parallel arms as two spheres (C).

Various SRR designs and arrangements have been tested through the past decade beginning with the double SRR consisting of a inner and outer square ring rotated 180° relative to each other, see Fig. 3.7. During miniaturization the single SRR design emerged [29],
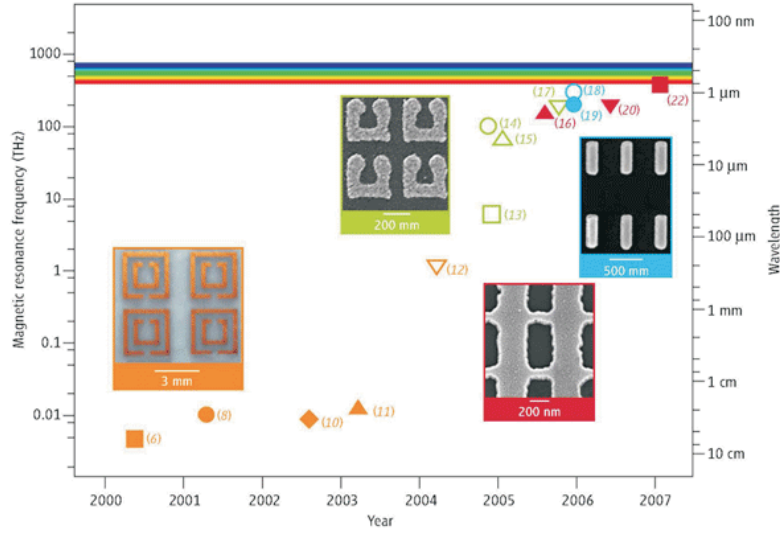
Figure 3.7: Overview of the downscaling of metamaterial structures from the GHz to THz range from year 2000 to 2007. The graph summarizes the progress for split-ring resonators (yellow and green), rods (blue), and fish-net structures (red). The numbers correspond to the references in [51]. Adapted from [51].

which like the double SRR exhibits an artificial magnetism. There are numerous variations of the single split-ring design including U-shaped [28], circular [53], and split-rings with multiple slits [37], see Fig. 3.8(a)-(e). The SRRs are commonly arranged in planar arrays with a single or multiple orientations [29, 54] [Fig. 3.8(f)-(g)] but SRRs have also been arranged in multilayers [55] [Fig. 3.8(h)]. The response of individual SRRs has also been experimentally investigated [56].
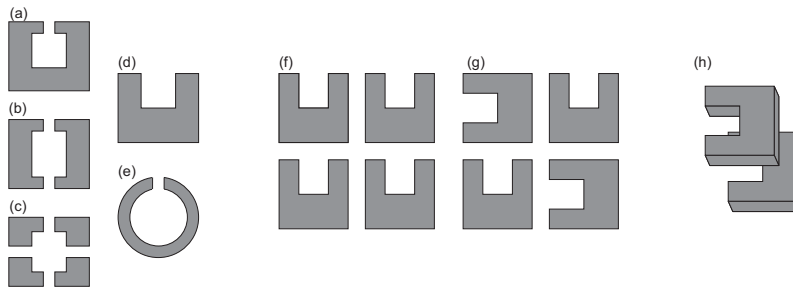
Figure 3.8: (a) Single slit SRR. (b) Double slit SRR. (c) Quadruple slit SRR. (d) U-shaped SRR. (e) Circular SRR. (f) SRR array oriented in one direction. (g) SRR array with two SRR orientations. (h) Multilayer SRRs.

Tuning of the resonance by geometrical scaling and altering the materials is well de-

scribed in literature. Rockstuhl *et al.* [57] carried out a systematic study of the geometrical tuning of square SRRs whereas Aydin *et al.* [58] tried a similar exercise for circular SRRs. Frequency tuning can also be done by altering the constituent materials. This was clearly highlighted by the work of Klein *et al.* [36] and Lahiri *et al.* [59] both attempting to tests the limits of scaling. While Klein *et al.* fabricated Au SRRs with a resonance at 900 nm and concluded that further downscaling would not decrease the resonance wavelength significantly, Lahiri *et al.* fabricated the SRRs out of aluminium lowering the resonance to 530 nm. Both groups attribute the scaling break-down to the finite kinetic energy of electrons imposing a fundamental limit on the resonance. However, the plasmon frequency of Al is higher than Au effectively lowering the overall inductance and consequently the resonance wavelength [59]. Finally, Padilla *et al.* [60] and Sun *et al.* [61] tuned the resonance by altering the dielectric environment either by photoexciting carriers in the underlying GaAs substrate or by using a fluid as the cladding layer replacing air, respectively.

Decker *et al.* [62] noticed that for SRRs arranged in 2x2 cell with half of the SRRs turned 90°(Fig. 3.8(h)), the array causes a waveplate behavior, which can lead to rather large optical activity [62]. The same SRR configuration leads to the the concept of bright and dark meta-atoms [63]. The bright elements couple directly to the incoming light, hence their arms are perpendicular to the polarization. The SRRs oriented parallel to the polarization do not couple but are excited indirectly by the magnetic dipole of the bright element inducing a current in the dark element circuits.

Some of the problems facing SRRs and metamaterials in general, are losses including the intrinsic material losses, radiation losses, and losses caused by the interaction between neighboring elements. They all contribute to widen the resonance, which for some applications such as refractive index sensors is undesired. Different attempts to compensate for the losses including incorporating gain into the metamaterial structures [64], fabricating metamaterials out of superconducting materials [65], exploiting the lower loss of dark elements compared to bright elements [66], and suppressing radiation damping by changing the resonator geometry [67].

3.2.2   Split-ring resonator sensors

Sun *et al.'s* [61] fluidic tuning experiments demonstrate one of the potential applications of SRRs, namely to be used as refractive index sensors. SRR based devices have already been employed in refractometric sensing used to detect thin layers of PMMA spincoated directly onto the SRRs detecting a 120 nm spectral shift for 30 nm PMMA [68]. Driscoll *et al.* [69] applied drops of Si nanospheres in an ethanol solution onto a surface containing SRRs. After the ethanol was evaporated, measurements revealed a ground mode frequency shift of 0.03 THz per drop.

Another potential sensing application of the SRR is related to strong field enhancement in the vicinity of the structure. For the ground resonance mode, the field is particularly strong in the gap region. The field enhancement has been used to detect small concentrations of DNA molecules using the polarization of the incident light to individually address two resonant modes enabling detection of two indepedent sensing events [70]. Cubukcu *et al.* [12] detected a self-assembled monolayers of 1-octadecanthiol with zeptomole sensitiv-

ity [Fig. 3.9(a)]. Detection is made possible when the SRR resonance and the molecules vibrational modes spectrally overlap, see Fig. 3.9(b)-(c). The molecules form a 2.4 nm thick monolayer with thiol end-groups binding to the gold surface. Assuming that the majority of the signal comes from the gap region, 40 zeptomoles of 1-octadecanthiol per SRR is required to obtain a detectable signal.
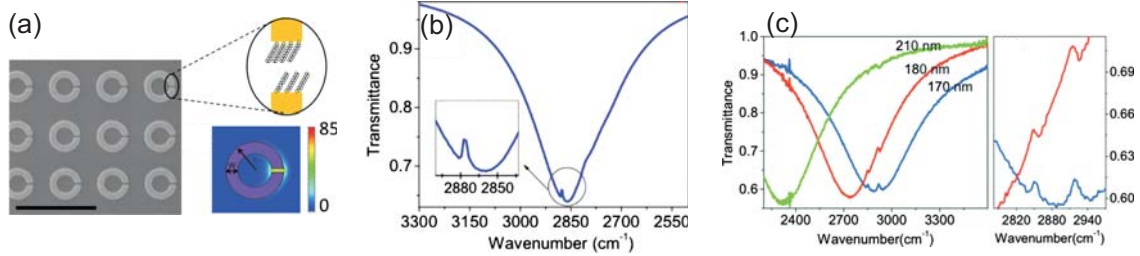
Figure 3.9: (a) SEM image of the fabricated split-ring resonator structures, the simulated **E**-field amplitude, and sketch of monolayers residing in the gap region. (b) The simulated far-field transmission spectrum with close-up on the absorption peak of the molecule. (c) Measured spectra for SRR's with different diameter. Inset shows a close-up of the molecules' absorption. Adapted from [12].

SRR's have also been used as wireless strain sensors fabricated onto a flexible substrate to enhance sensitivity [71]. By gradually increasing an applied load, the induced frequency shift was detected via transmission measurements. SRR's were used due to their large sensitivity to geometrical variations. Besides sensing applications, SRRs have also been used as notch filters [30] and as one part of the unit cell in perfect absorber materials [72].

3.2.3 State-of-the-art refractometric sensors

Two of the most widespread and sensitive commercial label-free detection techniques are based on surface plasmon resonance (SPR) and interferometers. In SPR sensing, a surface plasmon propagates along an interface typically between a metal and a dielectric where $\epsilon_d = -\epsilon_m$, see Fig. 3.10(a). The evanescent field of the plasmon decays into the sample solution with a characteristic nanometer decay length. Minute changes in refractive index influence the wavelength coupling to the surface plasmon and/or the coupling angle. By monitoring either of these, a sensing event can be detected. The surface plasmon is subjected to the high losses of the metal significantly limiting the propagation length, and hence sensitivity. This problem can to some extend be solved by Long Range Surface Plasmons (LRSP), where plasmons on both sides of a thin metal film couple. LRPS devices have been demonstrated with sensitivities up to 3.2×10^4 nm/RIU and detection limits down to 2.5×10^{-8} RIU [73]. A drawback of SRP sensing is the necessity of additional optical components such as a light coupling scheme (e.g. a prism) and a polarizer, which makes it rather difficult to integrate and miniaturize onto a chip.

Interferometers detect via the interference of light. In a Mach-Zehnder Interferometer [MZI, Fig. 3.10(b)] monochromatic light is coupled into a single mode fiber and the light
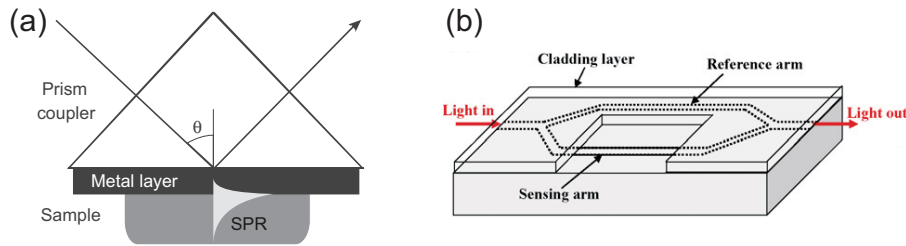
Figure 3.10: (a) A SPR-based refractometric sensor using prism coupling for excitation of plasmons at the metal-dielectric boundary. The light-coupling to the plasmon depends on the refractive index at the boundary. (b) Mach-Zehnder interferometer. Monochromatic, coherent light is split up at the input and recombined at the output. The output intensity is a function of the phase difference of the light in the two branches, which depends on the refractive index of the analyte surrounding the sensing arm. Adapted from [74, 75].

is split equally at a Y-junction. The evanescent field of one arm is allowed to interact with the analyte whereas the other arm is not. The two arms recombine and interfere at the output where the intensity is monitored by a photodetector. A refractive index change at the surface of the sensor branch changes the optical phase, the interference when the arms recombine and thereby the intensity at the output. The sensitivity of a Mach-Zehnder interferometer depends on the length of the sensing arm, which means there is a trade-off between size and sensitivity with integrated versions typically being millimeter to centimeter long. To enhance the sensitivity, a modulator can be added to the reference arm. A Mach-Zehnder interferometer with integrated modulator and centimeter long arms has demonstrated a 1×10^{-7} RIU detection limit [76]. Obviously, a modulator adds to the chip complexity whereas coupling to a single mode fiber with a core diameter of ~ 100 nm complicates operation.

Chapter 4

Hypothesis

This Ph.D. work is divided into the following two topics: high resolution imaging via a superlens and localized refractometric sensing using plasmonic resonators. The sensing potential of these systems is investigated with later integration in mind. This taken into account, not only is the sensing performance important but the fabricated structures should also enable down-stream processing without degrading the structures significantly and alter their performance. This directly translates into the choice of materials where biocompatibility as well as chemical and mechanical stability over a longer period of time is favored. This should ease the integration of either superlens or plasmonic resonators into an e.g. chip based fluidic platform.

The scope of the work can be summarized in the following form:

- The superlens project focuses on investigating the near-field silver superlens design demonstrated by Fang *et al.* [1]. The design consists of a flat silver slab, it operates at a free-space wavelength λ_0=365 nm, and superlensing is verified through photolithography with sub-wavelength resolution. However, the superlens design here is prepared for later integration into e.g. a lab-on-a-chip environment. Therefore it is paramount that the materials involved are resistant towards down-stream processing and biocompatible. This is where our work differs from Fang *et al.* allowing the superlens to potentially be used in non-invasive surface enhanced spectroscopy.

- The refractometric sensor project focuses on localized plasmonic structures as an alternative sensing platforms to already established sensing techniques. The split-ring resonator geometry has been chosen as a model system due to its fabrication simplicity, its relatively high sensitivity compared to other plasmonic structures, and an intuitive analytical description via equivalent circuit theory. The circuit model both gives an insight into the frequency scaling but also into the loss mechanisms, which are crucial for the optimization of the sensor performance in terms of figure-of-merit and detection limit.

Chapter 5

Fabrication

Electron-beam lithography is the fabrication workhorse for both the superlens and the split-ring resonator project. This fabrication technology is briefly described in the following section with the theory taken from [20]. Material choices are then discussed concerning the metals used for the plasmonic structures and the relevant surrounding dielectrics of the superlens design.

5.1   Electron beam lithography

Electron-beam lithography is a serial, top-down lithographic technique utilizing negatively charged electrons to expose a polymer resist material. Fig. 5.1 provides a schematic illustration of an EBL system.
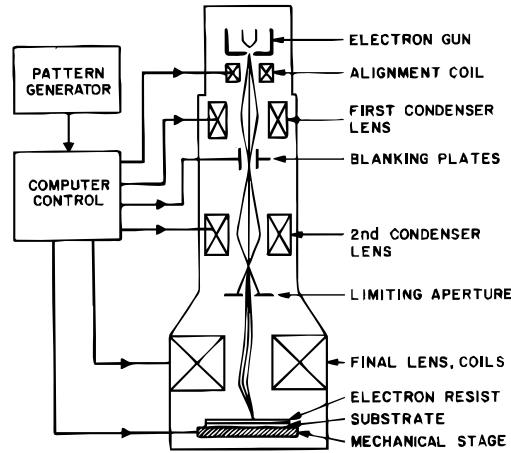

Figure 5.1: Schematic illustration of the EBL system. The central part is the colunm (right) where the electron beam is shaped and focused via electromagnets and apertures. The substrate resides on a mechanical stage that can be moved in a step-like motion. Reprinted from [77].

The electrons are extracted from a filament, accelerated by a voltage drop V_{acc}, and focused using electromagnetic lenses onto the substrate positioned on a mechanical stage. Apertures control the current I and the beam shape whereas beam deflectors determine the area that can be exposed without moving the stage. The column is kept under vacuum to minimize scattering.

In conventional photolithography, the resolution is proportional to the wavelength and limited by the diffraction of light. In the wave description of electrons the much shorter de Broglie wavelength λ_e is applied

$$\lambda_e = \frac{h}{p} = \frac{h}{\sqrt{2m_0 e V_{acc}}} \tag{5.1}$$

where h is Planck's constant, p is the electron momentum, m_0 is the electron mass, and e is the electron charge. For large acceleration voltages such as V_{acc}=100 kV, λ_e=0.1 nm meaning that the resolution is highly unaffected by diffraction. The beam size can be reduced to a few nanometers depending on the electromagnetic lenses and apertures.

Electrons experience forward- and back-scattering when penetrating the resist material and into the substrate. The scattering of electrons in the resist as well as the substrate defines the resolution limit of electron beam lithography together with material properties and processing conditions. Forward scattering describes small angle scattering events caused by electron-electron collisions, which broadens the effective beam diameter. Backscattering originates from electron-nuclei collisions whereby resist areas can be exposed several micrometers away from the beam position. This is known as the proximity effect putting a practical limit on the structure density.
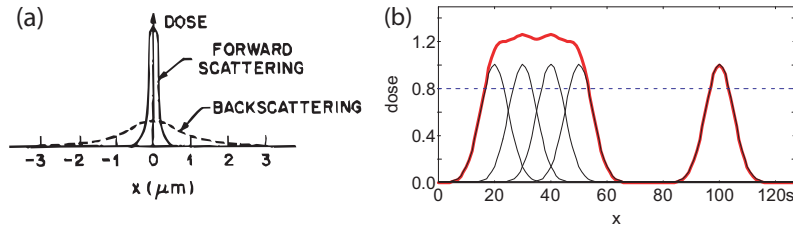
Figure 5.2: (a) Spatial dose distribution of the forward scattering and backscattering at the resist-substrate interface. (b) Effective dose (red line) for high density structures (left) and an isolated structure (right). The difference in effective dose is caused by the proximity efffect. Reprinted from [20].

There are two tones of resist: positive and negative. Exposing a positive resist results in bond breakage of the polymeric chains reducing the average molecular weight. This subsequently increases the solubility and exposed ares can be dissolved in the following development step. The contrary happens for a negative resist where bonds are formed in exposed areas reducing their solubility and they remain after development.

Apart from the tone of the resist there are two other important parameters: the contrast, and the sensitivity of the resist. The contrast is the slope of a resist thickness vs.

electron dose plot and the sensitivity is the dose to fully expose the resist. A resist with a higher contrast will in general have more vertical sidewall profiles but typically also higher sensitivity. The contrast is an important parameter for the final pattern resolution.

5.2 Plasmonic materials

Most plasmonic components for telecommunication and optical frequencies are made out of metals. Metals have large electrical conductivities as a result of high free electron densities, and the high plasma frequencies enables surface plasmon excitation (ε_d=-ε_m) at THz frequencies. Unfortunately, metals also have relatively large losses in this frequency region, which primarily arises from the free electron scattering and from interband transitions of bound electrons. For the free charges losses come from scattering effects caused by other electrons, phonons, lattice defects or grain boundaries [78]. For most naturally occurring materials, $\mu \sim 1$ and the material loss is described by the imaginary part of the permittivity ε''. Fig. 5.3 shows ε'' for the metals Ag, Al, Au and Cu.
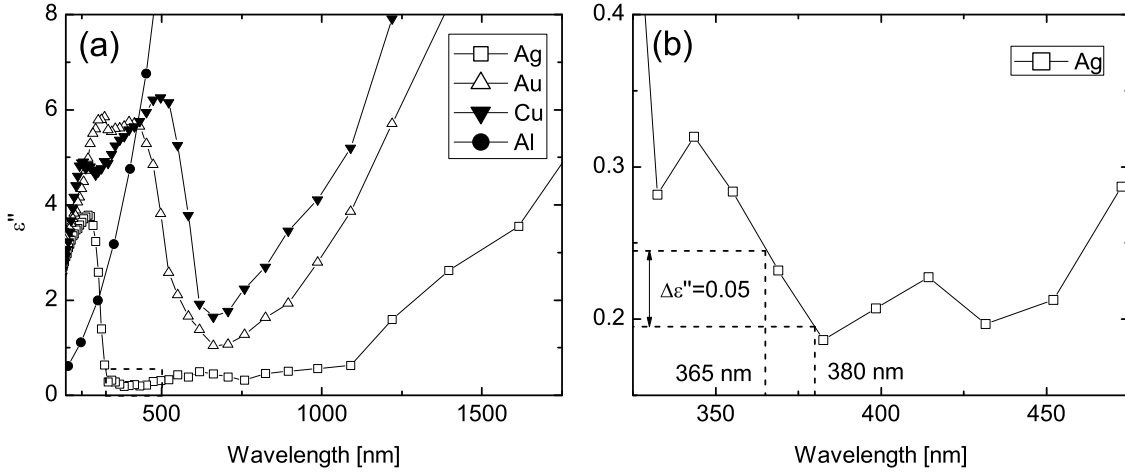
Figure 5.3: (a) The imaginary part of the permittivity ε'' for four metals Ag, Al, Au and Cu at visible and near-infrared wavelengths. (b) Zoom-in on Ag in the 325-475 nm range relevant for the near-field superlens. The data has been taken from [79, 80]

Fig. 5.3(a) shows that Al is the material of choice for wavelengths below 300 nm. In the visible to NIR, silver has the lowest loss with a minimum around 380 nm [Fig. 5.3(b)]. In terms of fabrication, silver degrades relatively fast in an ambient environment, which renders it less suitable for some applications. Gold has the second lowest loss and it has the advantage compared to both silver and copper of being chemically stable. Silver and gold are the two preferred metals for plasmonic structures. Alternatives have been proposed but for the majority of the materials, they can not compete in terms of loss and ease of fabrication at these frequencies. For a detailed discussion see West *et al.* [78].

Besides loss, another important parameter is biocompatibility in the context of chip

based sensing. For the refractometric sensing using localized plasmonic resonators, the sensitivity is typically inversely proportional to the distance between resonators and analyte. Hence, surface immobilization of the analyte on the metal is required. This is often enabled using a Self-Assembled Monolayer (SAM), which links the analyte to the surface. The most extensively studied case of SAMs is the alkenethiols binding to metal surfaces. Out of the metals, gold is the most studied and therefore the standard material. There are multiple reasons for that including the inertness of gold whereby experiments can be conducted in a ambient atmosphere, the high quality SAM films formed on gold, and the fact that gold is compatible with living cells. Contrary, silver it toxic to cells, and copper oxidizes even faster than silver. [81]

5.3 Polymers of superlens stack

Besides the quartz/chrome mask and the Ag layer, the superlens stack also consists of a planarizing spacer layer and a resist. For the original work by Fang *et al.* [1] they used I-line (365 nm) light, PMMA (ε'=2.301) as spacer layer and the negative resist NFR105G (ε'=2.301, JSR Micro), which is produced in industrial scale. Large quantities are usually not required for fundamental research, which is why we looked for another UV sensitive resist. However, the two conditions: compatibility with PMMA and high resolution UV resist are difficult to combine [82]. Besides, PMMA is easily dissolved in polar organic solvents, which are commonly used in standard micro- and nano-fabrication. Hence, a spacer material better suitable for downstream fabrication while still being biocompatible and having comparable optical properties, would be more attractive. It was decided to use the polymer Mr-I T85 (ε'=2.415, Microresist Gmbh [83]) over other common dielectrics such as SiO_2 (ε'=2.25) and Al_2O_3 due to better match of ε' as well as based on initial planarization tests. Mr-I T85 is compatible with a range of high resolution resists including the chosen mr-UVL 6000 negative resist (ε'=2.719, Microresist Gmbh [84]). It should be noted that both the spacer layer and the resist are closer to fulfilling the plasmon condition $\varepsilon'_{\mathrm{dielectic}} \approx \varepsilon'_{\mathrm{Ag}}$=2.401 than Fang's material choice. Also, PMMA and mr-UVL 6000 are not compatible since the solvent of mr-UVL 6000, dissolves PMMA.

5.3.1 Mr-I T85

Mr-I T85 is a Cyclo-Olefin Copolymer (COC). COCs have excellent optical properties and transmission even at wavelengths below 260 nm [85]. COC was originally developed as an alternative to polymers such as PMMA to improve some of its deficiencies while maintaining the optical properties. COC has a higher chemical resistance to acids and organic polar solvents, e.g. acetone and methanol, and a higher moisture barrier. In terms of the molecular structure, COC consists of two monomers ethylene and norbornene, see Fig. 5.4.

The COC materials are divided into grades that largely depend on the the relative content of the two monomers. The content influences both mechanical and thermal properties including the glass transition temperature T_g, which spans a temperature range of 78 to 178°C. The transmission of UV light in COC is comparable or better than PMMA [85].
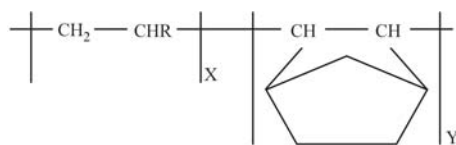
Figure 5.4: The molecular structure of the cyclo-olefin copolymer consisting of ethylene (left) and norbornene (right). The subscripts X & Y indicate that additional monomers may follow in a random order. Reprinted from [85].

The material is dispersive and the permittivity can be calculated from the Cauchy coefficients provided by the supplier where $n^2=\varepsilon$ for a dielectric [Eq. (5.2)].

$$n(\lambda) = 1.515 + \frac{5.25 \times 10^3}{\lambda^2} \tag{5.2}$$

where λ is the vacuum wavelength in nm.

5.3.2 Mr-UVL 6000

Mr-UVL 6000 is a negative, epoxy-based UV-sensitive resist. The name "epoxy" refers to a particular chemical group where one oxygen atom is bonded to two carbon atoms, which already have other bonds. Fig. 5.5 depicts a typical epoxy molecule.
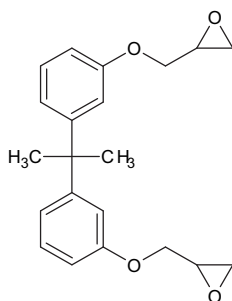
Figure 5.5: The molecular structure of a typical epoxy.

The epoxy molecule is formed from a long chain with reactive sites at either end. Mr-UVL 6000 is chemically amplified to increase the sensitivity to the exposure energy. An acid released by the exposure process, breaks up bonds of the epoxy molecule leaving OH-groups dangling. These OH^- groups then bind to OH^- groups on other epoxy molecules forming a long chain, thereby cross-linking the polymer and reducing the solubility drastically. The main part of the acid diffusion takes place during the subsequent post-exposure bake step where a single acid molecule can take part in multiple reactions. The acid diffusion length can in itself limit the resolution [86]. The two ring groups at its center are able to absorb mechanical and thermal stresses better than linear groups and

therefore give the epoxy based polymer a higher stiffness, toughness and heat resistance. The permittivity of mr-UVL 6000 can be calculated from the Cauchy coefficients provided by the supplier [Eq. (5.3)]

$$n(\lambda) = 1.57 + \frac{1.049 \times 10^4}{\lambda^2} \tag{5.3}$$

The version of the mr-UVL 6000 resist dedicated to EBL is sold under the trade name mr-EBL 6000 (earlier mr-L 6000XP). EBL exposures show that mr-EBL 6000 has a better resolution than SU-8, which is a commonly used UV/EBL sensitive resist. Since the two resists have comparable sensitivity and contrast, the resolution difference might be a result of a shorter acid diffusion length for mr-UVL 6000. The diffusion length is known to be a limiting factor for the resolution of SU-8 [86]. Since most photoresists are also sensitive to electrons [20], the resolution results should in theory be translatable to UV lithography. This is the reason why mr-UVL 6000 was chosen instead of SU-8.

Chapter 6

Work summary

6.1 Paper I - near-field superlens

The objective of the near-field superlens article is to reproduce the results of Fang *et al.* [1] by using their superlens stack design including layer thicknesses but employing a spacer material, mr-I T85, that is more suitable for integration, see Fig. 6.1(a). The superlens' performance is measured indirectly by employing a lithographic readout scheme using an I-line photoresist, mr-UVL 6000, and then measuring the surface modulation using an AFM [see Fig. 6.1(b)].
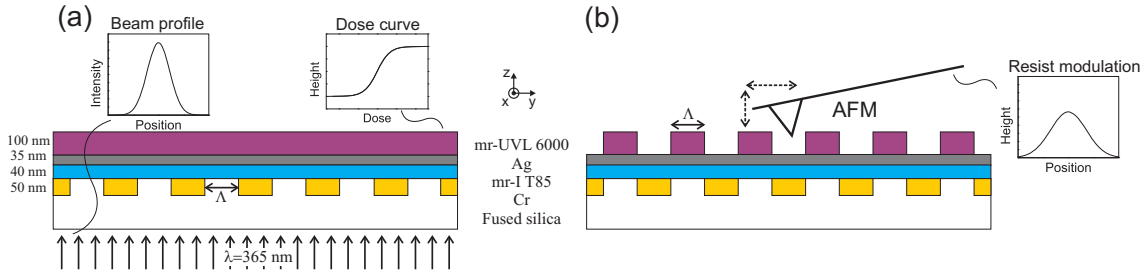
Figure 6.1: (a) The near-field superlens stack design with relevant materials and thicknesses. The fused silica/chrome mask patterns are reproduced in the photoresist by UV-lithography through the stack whereby the intensity modulations of the incoming beam are converted into topographical modulations via the dose curve of the resist. (b) After exposure and development, an AFM is used to characterize the surface.

The read-out method is not ideal since the light intensity is measured indirectly through the modulations of the remaining resist. The dose curve thereby acts as a transfer function of the light intensity with the resist properties i.e. contrast and acid diffusion length putting a limit on the resolvable feature size. Hence, the resolution obtained can be viewed as a minimum of the particular superlens design. Detecting the light intensity directly is preferable but this requires a near-field measuring technique operating at λ_0=365 nm, which we did not have access to during the course of this project.

6.1.1   Numerical calculations

To support the grating structure design, full-wave simulations of the transmitted field was employed. A commercially available finite-element method (Comsol Multiphysics) was used to solve the wave equation, Eq. (6.1)

$$\nabla \times \nabla \times E = \frac{\omega^2}{c^2}\varepsilon E, \tag{6.1}$$

In Comsol the RF-module, TM/TE waves, and scattered harmonic propagation were employed. The superlens stack is depicted in Fig. 6.2 where perfectly-matched layers (PMLs) are used for the horizontal domain boundaries (z-direction) while periodic boundary conditions are employed for the vertical domain boundaries (x-direction). For the material properties we employ $n = 1.475$ for the quartz, $n = 1.40 + i3.25$ for Cr, $n = 0.407 + i4.43$ for Al, $n = 1.554$ for mr-I T85 corresponding to $\varepsilon = 2.415$, $\varepsilon = -2.401 + i0.2488$ for Ag, and $n = 1.649$ for mr-UVL 6000. Figure 6.2 shows the intensity-distribution $(|E|/|E_0|)^2$ for 365 nm radiation in the resist layer for TE/TM polarization with and without a 80 nm half-pitch grating structure. TE is polarized along the x-direction whereas TM is polarized along the y-direction.
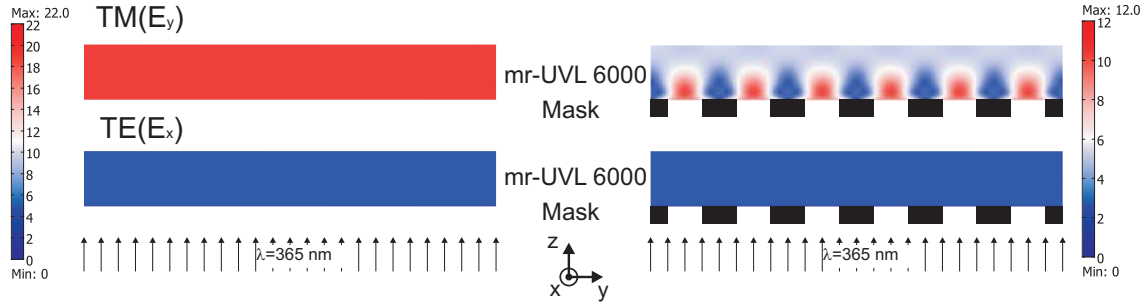
Figure 6.2: Finite-element modeling of the intensity-distribution $(|E|/|E_0|)^2$ for transverse magnetic and transverse electric incident light. Two scenarios are compared: superlens stack without the grating mask (left) and superlens stack including a 80 nm half-pitch grating mask (right).

As seen in Fig. 6.2 only a minor fraction of TE modes are transmitted compared to the TM modes. The UV aligner used for the exposure sends out a random polarization with a somewhat even distribution of TM and TE components. Recalling that the evanescent field enhancement is restricted to TM polarized light [17], the strong attenuation/reflection of the TE modes prevents an over-representation of propagating modes in the image plane. The addition of a 80 nm half-pitch grating structure reduces the overall intensity by approximately one half.

When the collimated light from the UV-aligner hits the grating structure at normal incidence, the light diverges into the spacer material. The divergence is primarily in the y-direction perpendicular to the grating lines since $\Lambda <<$ grating length ($\sim 20~\mu$m). The divergent beam is symmetrical around the z-direction but the individual plane-wave

components experience angled incidence. This leads to a difference in transmission and reflection of TE and TM polarized waves [22] with the TM modes being transmitted and focused beyond the lens, as evident in Fig. 6.2.

The transmission of the TM modes is sufficient for imaging 1D modulations with sub-wavelength resolution but when light impinges onto arbitrary structures, it diverges in all directions. Imaging arbitrary structures therefore requires enhancement and focusing of both TE and TM modes. A material with simultaneously $\varepsilon < 0$ and $\mu < 0$ can act as a near-perfect lens for arbitrary structures. However, its performance is still limited by the loss mechanisms described in Eq. (2.4).

6.1.2 Process optimization

The superlens design sets rather stringent demands on the processing. Nanometer thick layers with sub-nanometer roughness requires some process optimization. The mask fabrication is rather trivial but the proximity effect inherent to EBL limits the feature size to 60 nm half-pitch and $30{\times}30\ \mu m^2$ arrays for the employed positive resist, ZEP520A [see Appendix A.1, Fig. (4)]. By an anisotropic Reactive Ion Etch (RIE), the chrome layer is embedded into the fused silica to reduce surface modulation from 40 nm to about 12 nm prior to spincoating of the spacer layer, mr-I T85. By standard UV-lithography and metal deposition an aluminum cover lid is fabricated with $20{\times}20\ \mu m^2$ windows to the gratings. This concludes the mask fabrication.

A 300 nm thick mr-I T85 is spincoated onto the mask, RIE etched to 40 nm, and re-flowed/etched using a mild oxygen plasma. The RIE process increases the surface roughness of the mr-I T85 layer. mr-I T85 consists of two monomers (see section 5.3.1) and the etch might be selectively favoring one of the monomers. This can lead to local variations in etch rate thereby increasing the roughness. The oxygen plasma is an isotropic chemical etch, which reduces the surface roughness to the initial level after spincoating. The RIE etch rate is 1.7 nm/s and it therefore requires extreme process control to obtain a thickness of 40 nm (t_{T85}). Unfortunately, the mr-I T85 thickness could not be determined directly by optical techniques due to the restrictive micrometer sized grating arrays. Instead we employed an indirect technique, measuring the window profiles by AFM with and without mr-I T85 corresponding to $t_{Al,AFM}$ and $t_{T85,AFM}$, respectively [see Fig. 6.3(a)]. Combining these values with the thickness of the mr-I T85 on top of the Al lid measured by an ellipsometer, $t_{T85,Ellip}$, t_{T85} could be determined. Both the AFM and the ellipsometer have sub-nm vertical resolution. This measuring technique should ensure that the correct thickness is measured eventhough the etch rate above the silica/chrome mask might be slightly different than above the aluminum cover lid. The RIE etch and oxygen plasma cycle is repeated two to three times in order to reach a thickness of 40 nm$\pm$5 nm.

Then the 35 nm$\pm$2 nm Ag lens is deposited at an optimized rate of 1.5 Å/s to ensure a sub-nm rms roughness (typically 0.8-0.9 nm over a $5{\times}5\ \mu m^2$ area). To avoid oxidation of the silver, which increases the material loss, the mr-UVL 6000 resist is immediately spincoated onto the silver, exposed and developed. To enhance the contrast the resist is exposed with a dose corresponding to the maximum slope of the resist dose curve, see Fig. 6.3(b). This should provide the best contrast between the exposed and "unexposed"
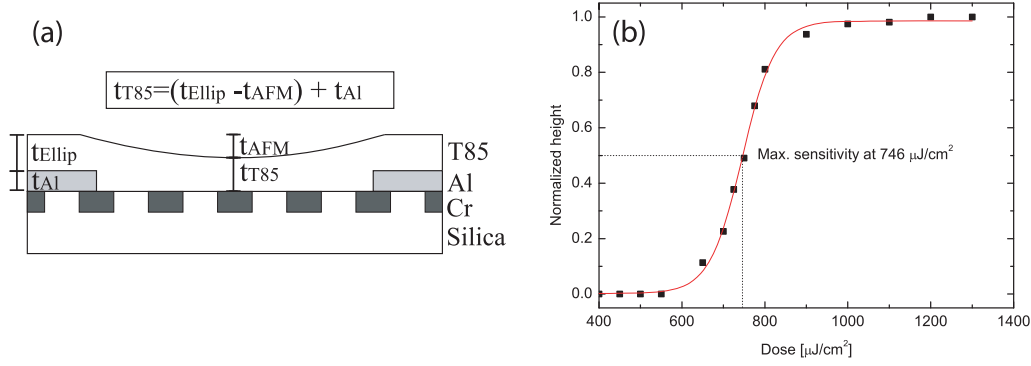
Figure 6.3: (a) Determining the layer thickness t_{T85} by AFM ($t_{T85,AFM}$ and $t_{Al,AFM}$) and ellipsometry ($t_{T85,Ellip}$). (b) Dosecurve for UV-exposure of 70 nm mr-UVL 6000 through 35 nm Ag. The data represent average values measured on 2×2 μm^2, and 5×5 μm^2 squares. The fitted sigmoidal curve has a maximum slope at $746\pm2\mu C/cm^2$.

areas. The clearing dose through the Ag layer is about 2 times the normal dose without a 35 nm silver layer [84]. The mr-UVL 6000 layer is then AFM scanned. 80 nm half-pitch gratings with 1-2 nm topographic modulations were resolved using the superlens stack.

6.1.3   Discussion

There can be many reasons for the resolution limit of our superlens stack and why we were not able to reproduce the 60 nm half-pitch reported by Fang *et al.* [1]. The rms roughness of the mr-I T85 is equivalent to their PMMA layer and we have a lower rms roughness of the Ag layer, ~ 0.9 as opposed to 1.5 nm [87]. Nevertheless, the surface periodicity a also affects the resolution but there is no comparable data. In terms of photoresist, we can only speculate that there might be a difference in resolution. An important aspect of our design is embedding the chrome mask to planarize the surface but whether that has an influence is also speculative.

There is some uncertainty regarding the thicknesses of the spacer and the metal layer. To test the superlens's sensitivity to height variations, a series of finite-element simulations were conducted where the thicknesses were altered in 10 nm intervals for a 60 nm $\Lambda/2$ grating, see Fig. 6.4. The data was retrieved via a line scan 15 nm into the resist, hence allowing the lens to somewhat focus the light. By altering the thicknesses, the focus position z also shifts, which means the comparison should be done with care. The lens fabricated here is asymmetric, but the expression for a symmetric lens proposed by Pendry [17] can still be used as a guideline (focus point beyond the lens $z = d_2 - d_1$, d_2 is the metal thickness and d_1 is the spacer thickness).

For the metal thicknesses, t_{Ag}=25 nm has the highest contrast but with poorest resolution. This can not be explaining by focusing action but is because the thin silver layer is unable to sufficiently enhance the evanescent fields whereby the finer details do not reach the image plane. The contrast is very low for t_{Ag}=45 nm due to material losses, which
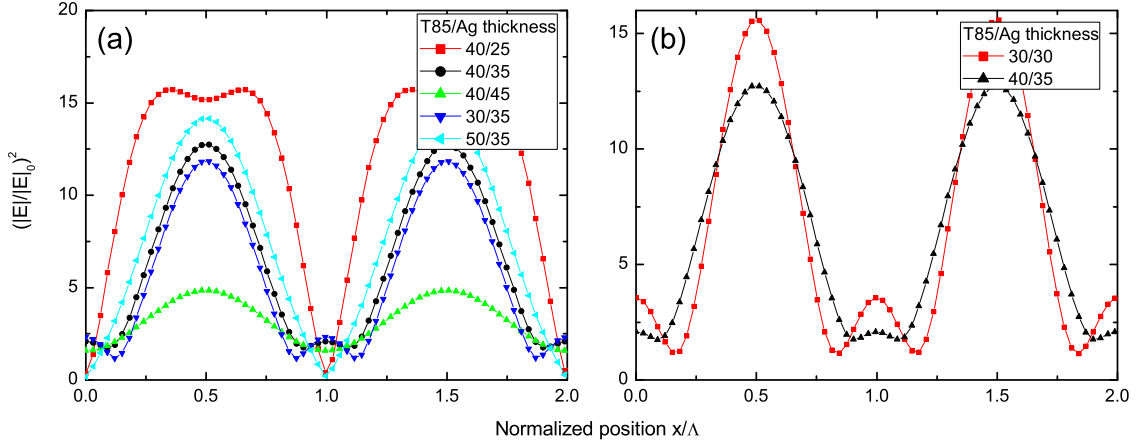
Figure 6.4: (a) & (b) Finite-element modeling of the intensity cross-section $(|E|/|E_0|)^2$ 15 nm into the resist for TM polarized light. Different layer thicknesses t_{T85}=30-50 nm and t_{Ag}=25-45 nm in steps of 10 nm are compared. The x-axis is the normalized position x with respect to the grating period Λ=120 nm.

are supported by the observations of Lee *et al.* [87]. When increasing the spacer thickness to 50 nm, the focus point moves closer to the lens and fewer high k components reach the silver lens, thereby decreasing the cut-off frequency. The reason for the slight increase in contrast, might be explained by moving closer to the focusing apex. The results for t_{T85}=30 nm are exactly opposite, higher resolution but lower contrast, using the above argumentation. The configuration 40/35 T85/Ag seems to be a good compromise between resolution and contrast. However, if the spacer layer can be reduced, the Ag layer can also be reduced yielding an improved contrast and resolution, see Fig. 6.4(b). For some samples, the initial mask modulation was sufficiently low to allow a 30 nm spacer layer.

One fundamental error was discovered "post project" concerning the exposure dose. The dose curve in Fig. 6.3(b) was made without the grating structure but using a mask with micrometer sized structures down to 1-2 μm. For a UV exposure where $\lambda < \Lambda$, the light intensity is not significantly attenuated by the mask but when $\lambda > \Lambda$, Fig. 6.2 shows that the intensity is drastically damped for $\Lambda/2$=80 nm. For 60-70 nm half pitch the attenuation is expected to be even stronger. Instead of using the dose corresponding to the maximum slope of the dose curve in Fig. 6.3(b), a dose above the clearing dose should have been used specified by the attenuation of the mask structure. Whether this would have improved the resolution is speculative but it would probably have had an influence on the height of the resist modulations. Due to the proximity effect, the grating periodicity would nevertheless be restricted to about 60 nm half-pitch for the employed e-beam resist (ZEP520A), which in itself would not present an improvement to the original results of Fang *et al.* [1].

6.1.4   Conclusion & outlook

Superlensing was demonstrated by resolving 80 nm half-pitch gratings in a negative photoresist employing light with a vacuum wavelength of 365 nm. The obtained resolution is below the diffraction limit and the results were supported by finite-element modelling of the field distribution in the resist. The resolution in itself is not impressive compared to the results of Fang *et al.* [1] and Melville *et al.* [49] resolving 60 nm and 72.5 nm, respectively. However, the choice of materials makes it suitable for later integration into e.g. a nanofluidic system where it can provide the advantages of surface enhanced spectroscopy without perturbing the sample molecules. Examples include a lab-on-a-chip device with integrated superlens and plasmonic nanoantennas proposed by Liu *et al* [88].

However, the project indicates that the integration into a lab-on-a-chip platform will be rather challenging due to the extreme fabrication tolerances regarding thickness and roughness. In addition, there are no apparent material alternatives to silver at the required wavelengths to obtain a resolution below 200 nm obtained by conventional optical microscopy [78]. As pointed out earlier, the problem with silver is that is quickly oxidizes in an ambient atmosphere. Eventhough COC-based polymers such as mr-I T85 are excellent moisture barriers, they are only moderately good as oxygen barriers. This is probably insufficient for a 40 nm membrane to prevent the silver from significantly degrading before the measurements can be carried out. Alternative dielectric materials include liquid crystal polymers and ethylene vinyl alcohols [85] but obviously they might have their own drawbacks conflicting with the application.

The resolution capabilities of near-field superlenses is astonishing but as have been pointed out earlier this resolution is limited to grating structures, hence structures with 1D periodic modulations where only a narrow range of k values have to be restored. This is sufficient for the superlens to improve the resolution of arbitrary structures but it does not give 1:1 imaging since not all k values are restored [1]. For near-perfect imaging of arbitrary structures both ε and μ have to be negative, simultaneously. This has been reported in fishnet structures with gain material to compensate for the material losses [64].

6.2   SRR articles

The 200×200 nm^2 split-ring resonators are fabricated by electron beam lithography in the positive resist ZEP520A, followed by metal deposition of 30-90 nm gold with/without a 2-5 nm adhesion layer, metal lift-off, and then the wafers are cut into samples that fit the measurement sample holder. The process is fast, within machine specs and simple allowing day-to-day testing of new designs. The resonances are measured using a far-field transmission setup, see Fig. 6.5(a).

The free space measurement setup uses a supercontinuum light source (500-1700 nm, SuperK SCB-Compact 100-PC) and an Optical Spectrum Analyzer (OSA) (500-1700 nm, Ando AQ-6315E). The output beam is collimated and broadened to a 200 μm spot via a parabolic mirror. Then the light is linearly polarized by a Glan-Thompson polarizer before it reaches the sample. After traversing the sample, the beam is focused by another parabolic mirror and collected with an output fiber with a 10 μm core diameter leading
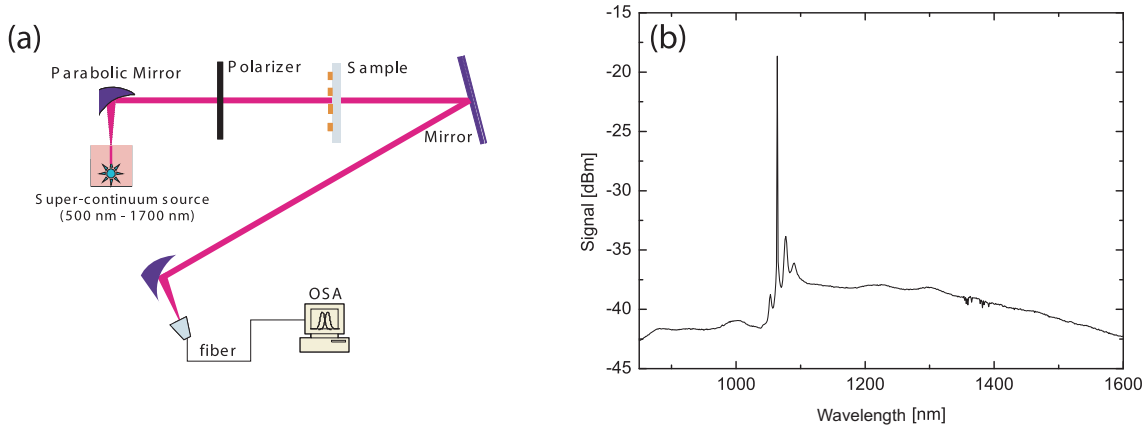
Figure 6.5: (a) Sketch of the free-space transmission measurement setup containing a supercontinuum light source (SuperK SCB-Compact 100-PC), and an OSA (Ando AQ-6315E). Reproduced from [64]. (b) The light source spectrum measured with the OSA via an optical fiber.

to the OSA. The peak at 1064 nm in Fig. 6.5(b) of the light source spectrum is an artifact attributed to the pump laser of the supercontinuum source. Intensity fluctuations around the pump laser frequency is a well known drawback of supercontinuum light sources [89], which is why care was taken into designing SRRs with resonances away from the range 1050-1100 nm.

The supporting numerical calculations were carried out using the general-purpose electromagnetic simulator, CST Microwave Studio, which is based on the Finite Integration Technique (FIT). The numerical method uses spatial discretization to split up the calculation domain into small grid cells, either in a tetrahedral or hexahedral pattern. Discretized Maxwells equations are then solved for each grid point. There is a choice of four different solvers domains: time, frequency, eigenmode or integral. For our SRR simulations we used the frequency domain, which is relevant for time-harmonic fields. The frequency domain solves the problem for a single frequency at a time, for a number of frequency samples. The solution comprises the field distribution as well as the S-parameters at the given frequency. We used the "FSS Unit cell (FD)" template, which automatically sets up unit cell boundary conditions in the x- and y-directions and sets up plane wave (TE/TM) port excitation in the z-direction. A typical SRR unit cell is illustrated in Fig. 6.6(a).

The calculation domain is divided into a tetrahedral mesh with a 1×10^{-6} accuracy, and adaptive mesh refinement. For a 100 THz range, 1000-10000 frequency samples are calculated giving a discretization of 10-100 THz^{-1}.

The dielectric dispersion of gold is commonly described in the metamaterial literature through either a Drude or Drude-Lorentz model [27, 90]. The Drude model is given in Eq. (6.2)
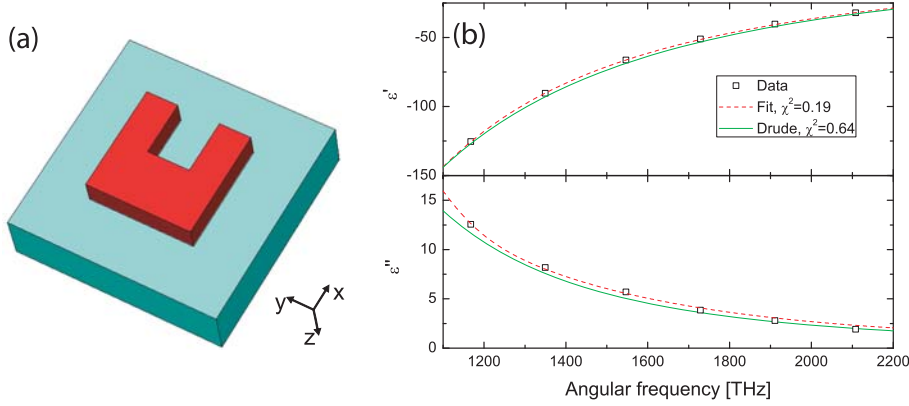
Figure 6.6: (a) A typical SRR unit cell used in the numerical modeling. It consists of a gold SRR on a fused silica substrate ($\varepsilon_{\text{silica}}$=2.1). (b) Johnson and Christy's [79] experimental data for ε' and ε'' as a function of angular frequency fitted with the Drude model and a higher order model native to CST.

$$\varepsilon(\omega) = \varepsilon_{\text{inf}} - \frac{\omega_p^2}{\omega(\omega + i\omega_c)} \tag{6.2}$$

where ω_{p} is the plasma frequency, ω_{c} is the collision frequency, and ε_{inf} is the background permittivity. We have to a large extend used the Drude model describing the free electrons of a metal as an electron plasma with parameters $\omega_p = 1.3673 \times 10^{16}$ s^{-1}, $\omega_c = 1.0027 \times 10^{14}$ s^{-1} and $\varepsilon_{\text{inf}} = 9.0$ [27]. The Drude model is a reasonable approximation in the wavelength range 850-1700 nm to the experimental data of Johnson and Christry [79]. Lately, we have applied a fit to the data using a higher order function native to CST. The Drude and higher order functions are compared in Fig. 6.6(b). χ^2 is an indicator of the goodness of the fit summing over the relative differences [91]. χ^2 for the higher order function is three times smaller compared to the Drude model, indicating an improvement in this particular frequency range 175-350 THz ($\sim$850-1700 nm).

6.2.1   Paper II - capacitance tuning

The circuit resonance in split-ring resonators relies on internal inductance and capacitance. In the simplest approximation the resonance is $\omega_0 = 1/\sqrt{LC} = c/\ell\sqrt{d/w}$ (Eq. 2.7) for a U-shaped SRR where c is the speed of light, ℓ is the sidelength, d is the slit gap, and w is the slit width. Acknowledging that ℓ stems from the inductance L and the slit ratio d/w comes from the capacitance C, the resonance can be linearly tuned by adjusting d/w without affecting the area, or interaction to neighboring meta-atoms. The overall shape and unit cell design therefore remains constant. Note that the resonance frequencies are well below the scaling limit for this design and material choice, see discussion in section 2.2.1.

The fabricated SRRs have ℓ=200 nm, d/w=0.76-0.88, Λ=440 nm, height h=30 nm plus a 5 nm Titanium (Ti) adhesion layer. The recorded resonances are compared to

the simple LC-model in a $(k_0\ell)^2$ vs. d/w plot with good quantitative agreement. We acknowledge that the adhesion layer, SRR-SRR coupling, surrounding dielectric materials, and the SRR height h influence the resonance position. Altering on of these parameters will inevitably affect the results and the agreement with the model. We therefore stress that this simple LC-model applies in this special case but we do not expect it to apply if the above parameters are significantly altered.

6.2.2 Paper III - extended LC-model

The simple LC-model breaks down at high frequencies, for high aspect ratio structures [35, 52], and when altering the dielectric constant of the surrounding materials significantly. By tuning all geometrical parameters including the height h, and replacing the cladding material with oils of different indexes, we were able to empirically verify an expansion to the existing model. The fluidic tuning tool allows for extensive testing of the parameter space while keeping the sample geometries constant. The expanded model builds on Eq. (2.7) adding two additional terms: a geometry dependent constant S and an effective permittivity ε_{eff} that incorporates a parameter f, which from the definition is the same f as in Eq. (1.1). f and S are perceived as geometrical corrections to the original shortcomings of the plate capacitor (C) and the single-loop coil (L) picture of the SRR geometry. The values of f and S can be derived from the tuning measurements, first determining f and then S.

There is good quantitative agreement between the model and the collected data with an error of about 3 %. The expanded model can be used as a general guideline to predict the resonance for a single SRR with arbitrary geometry and dielectric host materials. The model also confirms the results for the special case (Paper II).

A 5 nm Ti adhesion layer is used for the gold SRRs in this paper. The adhesion layer red-shifts the resonance compared to all-gold SRRs. This is a source of error for these measurements and the model derived. It is difficult to fabricate two arrays with exactly the same dimensions and the SRRs are very sensitive to geometrical changes. The impact of the 5 nm titanium layer is therefore better investigated by numerical tools. Fig. 6.7 shows the results of cladding tuning experiments with and without 5 nm Ti.

The cladding induced frequency shift does not change by introducing a thin Ti layer. The resonance red-shifts by 22 THz for 50 nm high SRRs, which corresponds to about 2 %. Further modelling show that this is a characteristic value for the geometries presented in the paper. If the samples had been fabricated without the 5 nm Ti layer they should in theory shift the same 2 %, which would alter the slope of the $(kl/S)^2$ vs. $d/\varepsilon_{\text{eff}}w$ graph by about the same percentage increasing the error from 3 % to about 5 %. Despite adjusting for the titanium layer, the model is still able to describe the resonance behavoir of SRRs in various dielectric host materials within a 5 % error.

6.2.3 Paper IV - adhesion layer

Adhesion promoters are commonly applied to ensure sufficient adhesion of gold layers on Si/SiO$_2$. The performance of two commonly used adhesion promoters, titanium and in-
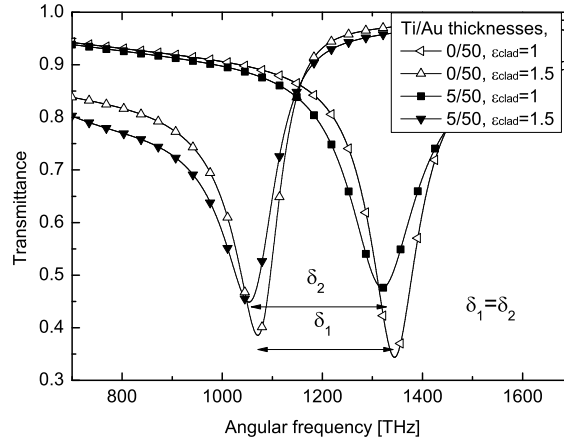
Figure 6.7: Simulated spectra of the ground mode SRR resonance with and without a 5 nm Ti adhesion layer for two cladding materials (n=1 and n=1.5). The SRR geometry has ℓ=200 nm, d/w=0.8, h=50 nm, and Λ=500 nm.

dium tin oxide (weight ratio 80/20 indium/tin, DC sputtered), are explored with respect to spectral shift and quality factor relative to an all-gold reference sample for SRR structures. The results are in agreement with perturbative considerations and show that both materials induce a spectral shift. The shift is expected since by introducing an adhesion layer, the local dielectric environment is altered, and as evident in Paper III the SRR's are very sensitive to such changes. For Ti the spectral shift is accompanied by a significant broadening, the results confirmed by numerical modeling (Fig. 6.8). The numerical data support the experimentally observed line broadening of 33% (29% simulations) and wavelength shift of 4% (2% simulations). The small quantitative discrepancy can be interpreted as small geometrical deviations from sample to sample.

Contrary to Ti, a thin ITO adhesion layer does not induce a broadening that can be detected by the current setup. The good insulating properties of ITO results in a high resistivity ρ compared to Au, ρ_{Au}= 3×10^{-8} $\Omega\cdot$m and ρ_{ITO}= 2×10^{-5} $\Omega\cdot$m measured by a four-point probe of 60 nm thick layers. This minimizes leak currents into the ITO during excitation. Ti has a comparable but higher resistivity than Au (ρ_{Ti}= 7×10^{-7} $\Omega\cdot$m), leading to a significant contribution to the ohmic damping. We acknowledge that the thicknesses for the resistivity measurement are not exactly the same as for the physical samples. However, it is difficult to characterize 2-5 nm layers accurately and the purpose of the investigation was only to give an order of magnitude estimation. For thinner layers the resistivity is expected to be even larger due to a larger surface to volume ratio.

The main conclusion of the adhesion layer investigation was that even 2 nm thin adhesion layers significantly contribute to the resonance position, and therefore have to be included in the numerical modeling. Concerning the use of ITO, we emphasize the well established fact that the electronic and optical properties are highly dependent on stoichiometry and fabrication details, as discussed in e.g. Lai *et al.* [92]. This precludes
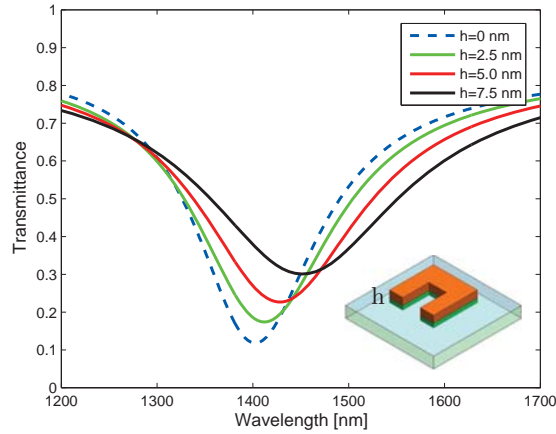
Figure 6.8: Numerical transmission data for a SRR structure with ℓ=200 nm, d/w=0.8, h_{Au}=50 nm, and Λ=500 nm. The thickness of the Ti adhesion layer is changed from h_{Ti}=0-7.5 nm.

quantitative numerical modeling of such systems unless the specific film is well characterized, which is difficult for such thin films. ITO is therefore sometimes simply neglected in numerical models, see e.g. Gansel *et al.* [93], and the physical parameters are "fudge fitted" to fit the simulations to experimentally observed data, see e.g. Klein *et al.* [94]. Hence, the fabrication and stoichiometric dependent optical properties of ITO precludes a general quantitative benchmarking of such samples.

For all-gold samples some of the SRRs will detach during the lift-off process, see Fig. 6.9.
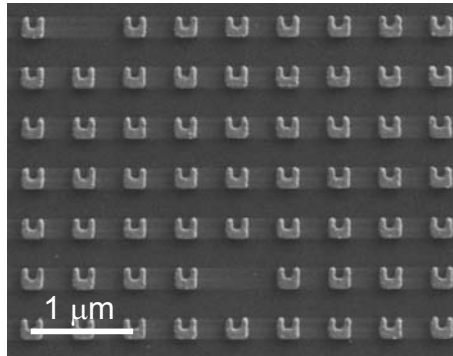
Figure 6.9: SEM micrograph of Au SRRs on a fused silica substrate. The structures have a sidelength ℓ=200 nm and a height h=50 nm, while the period is Λ=500 nm.

A small investigation was made to estimate the yield. Since a typical 2×2 mm^2 sample contains ∼10^7 resonators a full SEM inspection is not practically feasible but checking a

200×200 μm^2 area reveals a yield of $97\% \pm 1.8\%$. The detached SRRs should therefore not change the overall signal amplitude significantly in the transmission measurements. Indeed, if we focus a light beam to a 10 μm spot size and measure an average transmittance dip of 0.38 ± 0.008. The 0.008 modulation corresponds to a 2.1% variation, which is attributed to the yield variations. Since the numbers are in reasonable agreement they are seen as representative for the whole 2×2 mm^2 sample.

For applications of SRRs e.g. as refractive index sensors in a microfludic channel the poor adhesion of all-gold SRRs may result in additional detachment caused by e.g. fluid flow. An adhesion layer with a high optical quality such as ITO might then be favorable but the induced spectral shift must be accounted for if the resonance position is critical.

6.2.4   Paper V - refractometric sensing

The combination of sensitivity, transduction loss and linewidth ultimately determines the sensor performance of the SRR's. It is important to address the loss sources since they influence the resonance linewidth. The main contributions come from inhomogeneity, SRR-SRR coupling, radiation, and intrinsic loss. The inhomogeneity stems from the fabrication reproducibility. This term becomes increasingly important as the SRR's are downscaled and fabrication tolerances decrease. The coupling losses depend on the period Λ and on the overall unit cell design. The radiation losses are related to the SRR operating as an antenna, which receives and emits electromagnetic radiation. These processes are lossy with a large impact on the linewidth compared to intrinsic losses [56]. Since the radiation losses are related directly to the excitation, they can be minimized but not completely avoided. Finally, the intrinsic losses are the internal ohmic losses of the metal and presents the ultimately limit of localized SRR based sensors.

Based on the work by Wang and Shen [95], a figure-of-merit has been derived for plasmonic localized resonances in the quasi-static limit, hence where all characteristic length scales are much smaller than the wavelength. The FOM is of a universal nature, independent of geometry and directly linked to the intrinsic material losses, see Eq. (6.3)

$$\text{FOM} = \frac{|\varepsilon'_m|}{\varepsilon''_m}, \quad k\Lambda \ll 1. \tag{6.3}$$

where $\varepsilon_m = \varepsilon'_m + i\varepsilon''_m$ is the complex permittivity of the metal. The characteristic length scales of metamaterials are often comparable to the wavelength, hence $k\Lambda \sim 1$, and the quasi-static limit no longer explicitly applies. The predicted FOM values should therefore not be considered as absolute values for metamaterials but rather as estimates, beyond which large improvements ($> 10^2$) are not expected.

The theory is tested using a SRR model system where the concept of bright and dark modes is exploited by rotating the SRRs by $\pm\pi/2$, see section 2.2.1 for further explanation. Bright elements are directly excited by the incident radiation leading to large radiation dissipation whereas dark elements couple to the bright elements, their resonance linewidth being independent of radiation damping. By increasing the number of dark elements in a 2×2 unit cell, the radiation losses are reduced as well as the bright element coupling. To the contrary, the dark element coupling is enhanced but since the magnetic dipoles

arising from bright elements is stronger than for dark elements, the overall coupling is reduced. A FOM of 54 is obtained for a highly optimized unit cell design with a sensitivity $\Delta\lambda/\Delta n$=568.3 nm/RIU and a linewidth $\delta\lambda$=10.6 nm. Numerical modeling show that the sensitivity for a similar structure can be as high as 760 nm/RIU, which was partly confirmed by yielding a maximum of 704 nm/RIU experimentally.

A loss mechanism that remains to be addressed is the material loss. One way to reduce the material loss is simply to anneal the samples. Annealing increases the average grain size to reduce the number of grain boundaries in the SRR, and reduces the surface roughness. Chen *et al.* [96] demonstrated a linewidth improvement for square gold nanoantennas but also stressed that the results were highly dependent on the particle size, and aspect ratio. Systematic annealing tests using a rapid thermal annealling in the temperature range 200-400 °C did not show any significant improvement. Small improvements on the order of 10% were observed when annealing at 350 °C for 1 min but the results were not reproducible and for the majority of samples the linewidth increased. This confirms the observations of Chen *et al.*. Annealing was therefore generally not applied in the fabrication.

The sensor potential of the first higher order mode was also investigated. The linewidth may be slightly better than the ground mode but the field overlap into the cladding material is smaller, whereby the sensitivity is significantly reduced to about 370 nm/RIU based on experiments. Adding to the sometimes deform/asymmetric resonance (see Appendix A.5, Fig. 3), the ground mode was preferred for sensing purposes.

According to "Paper III", the sensitivity can be enhanced by increasing the height of the structures, since the height and f are somewhat proportional. Structures with $h_{\mathrm{Au}} >$ 90 nm were fabricated but any sensitivity enhancement was outweighed by additional inhomogeneous broadening. The results could indicate that the limits have been reached for this particular choice of materials, SRR design, and fabrication process.

The detection limit Δn_{min} was not experimentally tested but for $\Delta\lambda/\Delta n$=568.3 nm/RIU and $\delta\lambda$=10.6 nm, we estimate that $\Delta\lambda$=0.5-1 nm should be detectable with the current setup. This would yield $\Delta n_{\mathrm{min}} \sim 1\times10^{-3}$, which is factor of 10^4-10^5 larger than LSPR or interferometer based techniques [8]. The accuracy of the measurement setup can be improved by reducing the transduction losses. Still, vast improvement for localized surface plasmons based sensors is needed to present a competitive sensing platform. Losses have to be addressed by careful design and material choices [78], and then sensitivity must be significantly enhanced [97].

If the detection limit of these SRR sensors is sufficient for a particular application, the structure provides some advantages over state-of-the-art refractometric sensors such as LRSPR sensors and Mach-Zehnder interferometers. Its simplicity reduces the number of processing steps and imprinting techniques such as nanoimprint lithography, can be applied to significantly reduce the fabrication cost. However, imprinting is expected to introduce additional inhomogeneous broadening lowering the overall performance. For LR-SPR sensor and Mach-Zehnder interferometers, additional optical components are needed for for in- and/or out-coupling of light (beam expanders/lenses/prisms), polarizers for polarization control, collimators, and careful alignment either to obtain accurate angle control (LRSPR) or to avoid large losses (MZI). The advantage of SRR sensors is that no aligning is needed neither regarding the in-coupling of the light nor the excitation angle

since excitation at oblique angles is possible [98]. If every second SRR is rotated 90°, the sample becomes polarization independent [54]. However, such a structure reduces the FOM by a factor of three compared to the best case scenario (Appendix A.5, Fig. 3). If the in- and output fiber are close to the sample, and fibers with large core diameters are used to minimize beam divergence, collimators may not be necessary. Since the samples are typically 2×2 mm^2, the light beam does not require focusing either. A sensing device can therefore be made that does not require any additional optical components but only a broadband light source, a photodetector, and two fibers.

6.2.5   Conclusion & outlook

The limitations of metamaterial localized resonance sensors have been investigated theoretically and experimentally. Gold split-ring resonators have been employed as the model system yielding a figure-of-merit of up to 54. The high quality factor has been accomplished through the unit cell design by reducing the SRR-SRR coupling losses and the radiation damping. The measured values are comparable to the quasi-static predictions of Eq. (6.3), suggesting incremental improvements beyond this point. Equation (6.3) shows that the performance of localized plasmon based sensors scales with the material loss of the metal. Attempts have been made to reduce losses [96] or compensate for the losses using gain material [64]. However, with present knowledge, localized plasmonic resonance sensors do not appear as a competitive refractometric sensing platform based on FOM and detection limit [8]. However, for applications that only require a moderate detection limit, the SRR based sensor presents a simple, cheap alternative that does not require a complicated measurement architecture of external optical components.

Nevertheless, localized plasmonic resonances might still be useful in hybrid sensor systems such as the one demonstrated by Kabashin *et al.* [99]. Kabashin *et al.* used a closely spaced nanorod array supporting propagating and localized plasmons to achieve a FOM of 330. The structure have comparable merits to a pure LRSP device with the same setup requirements but with the advantage of a larger surface array making it more sensitive to actual biological samples.

Chapter 7

Conclusion

A near-field superlens was fabricated consisting of a thin silver slab sandwiched between a spacer layer, mr-I T85, and a photoresist, mr-UVL 6000. Superlensing was demonstrated using a photolithographic read-out scheme where a 80 nm half-pitch gratings of a chrome/glass shadow mask was transferred into height modulations of the resist. By using light with a vacuum wavelength of 365 nm, the obtained resolution is below the diffaction limit, which is approximately 120 nm for the given wavelength and materials. The resolution is comparable to the results of Fang *et al.* [1] and Melville *et al.* [49] but somewhat below recent advances in the field (30 nm half-pitch [4]). However, the mr-I T85 spacer material makes the superlens stack more suitable for later integration into a remote, non-invasive sensing platform. Nevertheless, this project indicates that the actual integration process will be very challenging due to the extreme fabrication tolerances in terms of layer roughness and thickness. Furthermore, the lens material silver degrades quickly in a ambient atmosphere due to oxidation, which increases its overall loss and thereby reduces its lens performance. Unfortunately, there seems to be no apparent material alternative that combines excitation of surface plasmons with low loss at terahertz frequencies required for the superlens to outperform conventional optical lenses where the state-of-the-art resolution limit is around 200 nm. Using silver, the ultrathin spacer layers have to be excellent barriers for any atmospheric substance that can potentially degrade the lens. We do not expect that the mr-I T85 used here, provides a sufficient oxygen barrier for a 40 nm thick layer nor that is will be easy finding a suitable spacer material that fulfills all criteria. That is also why there is a vast interest in finding/developing new low-loss plasmonic materials to replace the silver [78] and/or spacer material.

For imaging of arbitrary structures that requires amplification of a broad band of spatial frequencies, the permittivity and permeability must be negative simultaneously. This has been reported in fishnet structures with gain material to compensate the large material loss [64] but whether it can be for sub-diffraction imaging still needs to be demonstrated. Furthermore, to obtain 1:1 imaging it is necessary that the optical transfer function is relative flat for the all the relevant spatial frequencies [100]. If not, such as in the vicinity of the surface plasmon frequency, some frequencies will be over-represented in the image plane, which will degrade the image.

In the second part of the Ph.D. work nanoscale gold split-ring resonators were employed as a model system to investigate the potential of localized plasmonic refractometric sensors. The SRRs were fabricated by electron beam lithography and characterized via far-field transmission measurements. Prior to optimizing the sensor design, the influence of two commonly used adhesion layers, titanium and indium tin oxide, was investigated in terms of spectral position and quality factor. The results showed a vast difference in the optical quality between the two materials. An extended circuit model describing the ground mode resonance was also developed and empirically verified through fluidic tuning experiments. The extended model distinguishes itself by describing the resonance position as a function of all geometrical parameters and host materials without altering the equation complexity significantly. This ensures that the simple scaling description of the original circuit model is maintained.

For highly optimized SRR structures a figure-of-merit of 54 was achieved for the ground mode resonance. The high figure-of-merit was accomplished by addressing two of the loss mechanisms: radiation damping and SRR-SRR coupling losses. This was done through the unit cell design consisting of high loss bright elements and low loss dark elements. The results are superior compared to other localized metamaterial structures [101, 102]. According to quasi-static predictions the performance of localized plasmonic based sensors scales with the material loss of the metal, and only incremental improvements are expected beyond this point. The material losses of the gold was not specifically addressed in the investigation here but attempts have been made in literature to reduce or compensate for these intrinsic losses [96, 64].

By combining the resonance linewidth and the spectral resolution of the measurement setup, a detection limit of 1×10^{-3} RIU was estimated. This is factor of 10^4-10^5 larger than for state-of-the-art refractomeric sensors [8]. Hence, vast improvement are required for this sensing platform to represent a real alternative to e.g. LRSP sensors and interferometers, which with present knowledge seems unlikely. However, a recent direct comparison of localized and propagating plasmon sensors by Svedendahl *et al.* [103], reveal similar performance in an actual biosensing experiment, despite a much larger sensitivity and FOM of the latter. They explain the results by a better utilization of the bulk sensitivity for localized plasmonic sensors. This is in agreement with observations by Kabashin *et al.* [99] seeing the localized sensors as more biosensitive.

Some of the advantages of the SRR sensors studied here include their fabrication simplicity, their cost (when imprint techniques are used), and that they do not require extensive use of external optical components, which makes them suitable for portable devices. Whether localized plasmonic sensors will mature as a sensing platform is speculative. However, their large biosensitivity is undoubtedly useful in hybrid sensor systems such as the one proposed by Kabashin *et al.* [99].

Bibliography

[1] N. Fang, H. Lee, C. Sun, and X. Zhang, "Sub-diffraction-limited optical imaging with a silver superlens," Science **308**(5721), 534–537 (2005).

[2] X. Zhang and Z. Liu, "Superlenses to overcome the diffraction limit," Nat. Mater. **7**(6), 435–441 (2008).

[3] S. A. Maier, *Plasmonics: fundamentals and applications* (Springer, 2007).

[4] P. Chaturvedi, W. Wu, V. J. Logeeswaran, Z. Yu, M. S. Islam, S. Y. Wang, R. S. Williams, and N. X. Fang, "A smooth optical superlens," Appl. Phys. Lett. **96**(4), 043102 (2010).

[5] G. Smulevich and T. Spiro, "Surface enhanced Raman-spectroscopy evidence that adsorption on silver particles can denaturate heme-proteins," J. Phys. Chem.-US **89**(24), 5168–5173 (1985).

[6] R. B. Nielsen, M. D. Thoreson, W. Chen, A. Kristensen, J. M. Hvam, V. M. Shalaev, and A. Boltasseva, "Toward superlensing with metal-dielectric composites and multilayers," Appl. Phys. B-Lasers. O. **100**(1, Sp. Iss. SI), 93–100 (2010).

[7] N. A. Mortensen, S. Xiao, and J. Pedersen, "Liquid-infiltrated photonic crystals: enhanced light-matter interactions for lab-on-a-chip applications," Microfluid. Nanofluid. **4**(1-2), 117–127 (2008).

[8] X. Fan, I. M. White, S. I. Shopoua, H. Zhu, J. D. Suter, and Y. Sun, "Sensitive optical biosensors for unlabeled targets: A review," Anal. Chim. Acta **620**(1-2), 8–26 (2008).

[9] L. J. Sherry, R. Jin, C. A. Mirkin, G. C. Schatz, and R. P. Van Duyne, "Localized surface plasmon resonance spectroscopy of single silver triangular nanoprisms," Nano Lett. **6**(9), 2060–2065 (2006).

[10] BIAcore owned by GE Healthcare, http://www.biacore.com.

[11] Thorlabs, Inc., http://www.thorlabs.com/newgrouppage9.cfm?objectgroup_id=2913.

[12] E. Cubukcu, S. Zhang, Y.-S. Park, G. Bartal, and X. Zhang, "Split ring resonator sensors for infrared detection of single molecular monolayers," Appl. Phys. Lett. **95**(4), 043113 (2009).

[13] N. Liu, T. Weiss, M. Mesch, L. Langguth, U. Eigenthaler, M. Hirscher, C. Soennich-sen, and H. Giessen, "Planar Metamaterial Analogue of Electromagnetically Induced Transparency for Plasmonic Sensing," Nano Lett. **10**(4), 1103–1107 (2010).

[14] J. Goodman, *Introduction to Fourier Optics*, pp. 97–102, 2nd ed. (McGraw-Hill, 1996).

[15] M. Born and E. Wolf, *Principles of optics*, p. 419, 7th ed. (Cambridge University Press, 1999).

[16] M. W. Davidson, "Resolution," www.microscopyu.com/articles/formulas/formulasresolution.html.

[17] J. B. Pendry, "Negative refraction makes a perfect lens," Phys. Rev. Lett. **85**(18), 3966–3969 (2000).

[18] J. Lichtman and J. Conchello, "Fluorescence microscopy," Nat. Methods **2**(12), 910–919 (2005).

[19] F. J. Garcia de Abajo, "Optical excitations in electron microscopy," Rev. Mod. Phys. **82**(1), 209–275 (2010).

[20] M. A. McCord and M. J. Rooks, *Handbook of microlithography, micromachining, and microfabrication. - 1: Microlithography*, vol. 1, chap. 2, pp. 139–250 (SPIE Publications, 1997).

[21] W. Cai and V. Shalaev, *Optical Metamaterials*, pp. 148–149 (Springer, 2010).

[22] F. L. Pedrotti, L. S. Pedrotti, and L. M. Pedrotti, *Introduction to Optics*, pp. 619–621, 3rd ed. (Prentice Hall International, 2007).

[23] V. Veselago, "Electrodynamics of substances with simultaneously negative values of sigma and mu," Sov. Phys. Uspekhi. **10**(4), 509–514 (1968).

[24] D. R. Smith, D. Schurig, M. Rosenbluth, S. Schultz, S. A. Ramakrishna, and J. B. Pendry, "Limitations on subdiffraction imaging with a negative refractive index slab," Appl. Phys. Lett. **82**(10), 1506–1508 (2003).

[25] J. Valentine, J. Li, T. Zentgraf, G. Bartal, and X. Zhang, "An optical cloak made of dielectrics," Nat. Mat. **8**(7), 568–571 (2009).

[26] J. B. Pendry, A. J. Holden, D. J. Robbins, and W. J. Stewart, "Magnetism from conductors and enhanced nonlinear phenomena," IEEE Trans. Microwave Theory Tech. **47**(11), 2075–2084 (1999).

[27] V. M. Shalaev, W. S. Cai, U. K. Chettiar, H. K. Yuan, A. K. Sarychev, V. P. Drachev, and A. V. Kildishev, "Negative index of refraction in optical metamaterials," Opt. Lett. **30**(24), 3356–3358 (2005).

[28] C. Jeppesen, N. A. Mortensen, and A. Kristensen, "Capacitance tuning of nanoscale split-ring resonators," Appl. Phys. Lett. **95**(19), 193108 (2009).

[29] S. Linden, C. Enkrich, M. Wegener, J. F. Zhou, T. Koschny, and C. M. Soukoulis, "Magnetic response of metamaterials at 100 terahertz," Science **306**(5700), 1351–1353 (2004).

[30] I. Gil, J. Garcia-Garcia, J. Bonache, F. Martin, M. Sorolla, and R. Marques, "Varactor-loaded split ring resonators for tunable notch filters at microwave frequencies," Electron. Lett. **40**(21), 1347–1348 (2004).

[31] D. Smith, W. Padilla, D. Vier, S. Nemat-Nasser, and S. Schultz, "Composite medium with simultaneously negative permeability and permittivity," Phys. Rev. Lett. **84**(18), 4184–4187 (2000).

[32] P. Gay-Balmaz and O. Martin, "Electromagnetic resonances in individual and coupled split-ring resonators," J. Appl. Phys. **92**(5), 2929–2936 (2002).

[33] N. Katsarakis, T. Koschny, M. Kafesaki, E. N. Economou, and C. M. Soukoulis, "Electric coupling to the magnetic resonance of split ring resonators," Appl. Phys. Lett. **84**(15), 2943–2945 (2004).

[34] H. C. Guo, N. Liu, L. W. Fu, H. Schweizer, S. Kaiser, and H. Giessen, "Thickness dependence of the optical properties of split-ring resonator metamaterials," Phys. Stat. Sol. (b) **244**(4), 1256–1261 (2007).

[35] T. D. Corrigan, P. W. Kolb, A. B. Sushkov, H. D. Drew, D. C. Schmadel, and R. J. Phaneuf, "Optical plasmonic resonances in split-ring resonator structures: an improved LC model," Opt. Express **16**(24), 19850–19864 (2008).

[36] M. W. Klein, C. Enkrich, M. Wegener, C. M. Soukoulis, and S. Linden, "Single-slit split-ring resonators at optical frequencies: limits of size scaling," Opt. Lett. **31**(9), 1259–1261 (2006).

[37] J. Zhou, T. Koschny, M. Kafesaki, E. Economou, J. Pendry, and C. Soukoulis, "Saturation of the magnetic response of split-ring resonators at optical frequencies," Phys. Rev. Lett. **95**(22), 223902 (2005).

[38] S. Tretyakov, "On geometrical scaling of split-ring and double-bar resonators at optical frequencies," Metamaterials **1**(1), 4043 (2007).

[39] V. Delgado, O. Sydoruk, R. Tatartschuk, E. Marques, and L. Freire, M.J. Jelinek, "Analytical circuit model for split ring resonators in the far infrared and optical frequency range," Metamaterials **3**(2), 5762 (2009).

[40] I. Sersic, M. Frimmer, E. Verhagen, and A. F. Koenderink, "Electric and Magnetic Dipole Coupling in Near-Infrared Split-Ring Metamaterial Arrays," Phys. Rev. Lett. **103**(21), 213902 (2009).

[41] P. A. Tipler and G. Mosca, *Physics for scientists and engineers*, pp. 944–947, 5th ed. (W. H Freeman and Company, 2004).

[42] R. Shelby, D. Smith, and S. Schultz, "Experimental verification of a negative index of refraction," Science **292**(5514), 77–79 (2001).

[43] N. Fang and X. Zhang, "Imaging properties of a metamaterial superlens," Appl. Phys. Lett. **82**(2), 161–163 (2003).

[44] N. Fang, Z. Liu, T. Yen, and X. Zhang, "Regenerating evanescent waves from a silver superlens," Opt. Express **11**(7), 682–687 (2003).

[45] D. O. S. Melville and R. J. Blaikie, "Near-field optical lithography using a planar silver lens," J. Vac. Sci. Technol. B **22**(6), 3470–3474 (2004).

[46] S. Durant, N. Fang, and X. Zhang, "Comment on "Submicron imaging with a planar silver lens" [Appl. Phys. Lett. 84, 4403 (2004)]," Appl. Phys. Lett. **86**(12), 126101 (2005).

[47] D. Melville and R. Blaikie, "Response to "Comment on 'Submicron imaging with a planar silver lens' " [Appl. Phys. Lett. 86, 126101 (2005)]," Appl. Phys. Lett. **86**(12), 126102 (2005).

[48] R. J. Blaikie and D. O. S. Melville, "Imaging through planar silver lenses in the optical near field," J. Opt. A-Pure Appl. Opt. **7**(2) (2005).

[49] D. O. S. Melville and R. J. Blaikie, "Super-resolution imaging through a planar silver layer," Opt. Express **13**, 2127–2134 (2005).

[50] T. Taubner, D. Korobkin, Y. Urzhumov, G. Shvets, and R. Hillenbrand, "Near-field microscopy through a SiC superlens," Science **313**(5793), 1595–1595 (2006).

[51] C. M. Soukoulis, S. Linden, and M. Wegener, "Negative refractive index at optical wavelengths," Science **315**(5808), 47–49 (2007).

[52] H. C. Guo, N. Liu, L. W. Fu, T. P. Meyrath, T. Zentgraf, H. Schweizer, and H. Giessen, "Resonance hybridization in double split-ring resonator metamaterials," Opt. Express **15**(19), 12095–12101 (2007).

[53] A. W. Clark, A. K. Sheridan, A. Glidle, D. R. S. Cumming, and J. M. Cooper, "Tuneable visible resonances in crescent shaped nano-split-ring resonators," Appl. Phys. Lett. **91**(9), 093109 (2007).

[54] M. Decker, S. Linden, and M. Wegener, "Coupling effects in low-symmetry planar split-ring resonator arrays," Opt. Lett. **34**(10), 1579–1581 (2009).

[55] N. Liu, H. Liu, S. Zhu, and H. Giessen, "Stereometamaterials," Nat. Photonics **3**(3), 157–162 (2009).

[56] M. Husnik, M. W. Klein, N. Feth, M. Konig, J. Niegemann, K. Busch, S. Linden, and M. Wegener, "Absolute extinction cross-section of individual magnetic split-ring resonators," Nature Photonics **2**(10), 614–617 (2008).

[57] C. Rockstuhl, T. Zentgraf, H. Guo, N. Liu, C. Etrich, I. Loa, K. Syassen, J. Kuhl, F. Lederer, and H. Giessen, "Resonances of split-ring resonator metamaterials in the near infrared," Appl. Phys. B-Lasers. O. **84**(1-2), 219–227 (2006).

[58] K. Aydin, I. Bulu, K. Guven, M. Kafesaki, C. M. Soukoulis, and E. Ozbay, "Investigation of magnetic resonances for different split-ring resonator parameters and designs," New J. Phys. **7**(168), 1367–2630 (2005).

[59] B. Lahiri, S. G. McMeekin, A. Z. Khokhar, R. M. De la Rue, and N. P. Johnson, "Magnetic response of split ring resonators (SRRs) at visible frequencies," Opt Express **18**(3), 3210–3218 (2010).

[60] W. Padilla, A. Taylor, C. Highstrete, M. Lee, and R. Averitt, "Dynamical electric and magnetic metamaterial response at terahertz frequencies," Phys. Rev. Lett. **96**(10), 107401 (2006).

[61] Y. Sun, X. Xia, H. Feng, H. Yang, C. Gu, and L. Wang, "Modulated terahertz responses of split ring resonators by nanometer thick liquid layers," Appl. Phys. Lett. **92**(22), 221101 (2008).

[62] M. Decker, R. Zhao, C. M. Soukoulis, S. Linden, and M. Wegener, "Twisted split-ring-resonator photonic metamaterial with huge optical activity," Opt. Lett. **35**(10), 1593–1595 (2010).

[63] S. Zhang, D. A. Genov, Y. Wang, M. Liu, and X. Zhang, "Plasmon-induced transparency in metamaterials," Phys. Rev. Lett. **101**(4), 047401 (2008).

[64] S. Xiao, J. Zhang, L. Peng, C. Jeppesen, R. Malureanu, A. Kristensen, and N. A. Mortensen, "Nearly zero transmission through periodically modulated ultrathin metal films," Appl. Phys. Lett. **97**(7), 071116 (2010).

[65] V. A. Fedotov, A. Tsiatmas, J. H. Shi, R. Buckingham, P. de Groot, Y. Chen, S. Wang, and N. I. Zheludev, "Temperature control of Fano resonances and transmission in superconducting metamaterials," Opt. Express **18**(9), 9015–9019 (2010).

[66] M. Stockman, S. Faleev, and D. Bergman, "Localization versus delocalization of surface plasmons in nanosystems: Can one state have both characteristics?" Phys. Rev. Lett. **87**(16), 167401 (2001).

[67] M. G. Nielsen, A. Pors, R. B. Nielsen, A. Boltasseva, O. Albrektsen, and S. I. Bozhevolnyi, "Demonstration of scattering suppression in retardation-based plasmonic nanoantennas," Opt. Express **18**(14), 14802–14811 (2010).

[68] B. Lahiri, A. Z. Khokhar, R. M. De La Rue, S. G. McMeekin, and N. P. Johnson, "Asymmetric split ring resonators for optical sensing of organic materials," Opt. Express **17**(2), 1107–1115 (2009).

[69] T. Driscoll, G. O. Andreev, D. N. Basov, S. Palit, S. Y. Cho, N. M. Jokerst, and D. R. Smith, "Tuned permeability in terahertz split-ring resonators for devices and sensors," Appl. Phys. Lett. **91**(6), 062511 (2007).

[70] A. W. Clark, A. Glidle, D. R. S. Cumming, and J. M. Cooper, "Plasmonic split-ring resonators as dichroic nanophotonic DNA biosensors," J. Am. Chem. Soc. **131**(48), 17615–17619 (2009).

[71] R. Melik, E. Unal, N. K. Perkgoz, C. Puttlitz, and H. V. Demir, "Flexible metamaterials for wireless strain sensing," Appl. Phys. Lett. **95**(18), 181105 (2009).

[72] N. I. Landy, S. Sajuyigbe, J. J. Mock, D. R. Smith, and W. J. Padilla, "Perfect metamaterial absorber," Phys Rev. Lett. **100**(20), 207402 (2008).

[73] R. Slavik and J. Homola, "Ultrahigh resolution long range surface plasmon-based sensor," Sensor. Actuat. B-Chem. **123**(1), 10–12 (2007).

[74] J. Homola, H. Vaisocherova, J. Dostalek, and M. Piliarik, "Multi-analyte surface plasmon resonance biosensing," Methods **37**(1), 26–36 (2005).

[75] P. Chaturvedi, K. Hsu, S. Zhang, and N. Fang, "New frontiers of metamaterials: design and fabrication," MRS Bull. **33**(10), 915–920 (2008).

[76] R. Heideman and P. Lambeck, "Remote opto-chemical sensing with extreme sensitivity: design, fabrication and performance of a pigtailed integrated optical phase-modulated Mach-Zehnder interferometer system," Sensor. Actuat. B-Chem. **61**(1-3), 100–127 (1999).

[77] S. Sze, *Semiconductor devices : Physics and technology* (Wiley, 1985).

[78] P. West, S. Ishii, G. Naik, N. Emani, V. Shalaev, and A. Boltasseva, "Searching for better plasmonic materials," Laser Photonics Rev. **4**(6), 795–808 (2010).

[79] P. B. Johnson and R. W. Christy, "Optical constants of noble metals," Phys. Rev. B **6**(12), 4370–4379 (1972).

[80] E. D. Palik, *Handbook of Optical Constants of Solids* (CRC Press, San Diego, 1998).

[81] J. Love, L. Estroff, J. Kriebel, R. Nuzzo, and G. Whitesides, "Self-assembled monolayers of thiolates on metals as a form of nanotechnology," Chem. Rev. **105**(4), 1103–1169 (2005).

[82] M. Vogler, micro resist technology GmbH, e-mail correspondence April 2008.

[83] micro resist technology GmbH, "mr-I T85 Thermoplastic Polymer for Nanoimprint Lithography," Material datasheet.

[84] micro resist technology GmbH, "Negative Tone Photoresists mr-UVL 6000," Material datasheet.

[85] TOPAS Advanced Polymers GmbH, "UV Transmission," http://www.topas-us.com/tech/data/uv.htm.

[86] B. Bilenberg, M. Scholer, P. Shi, M. S. Schmidt, P. Boggild, M. Fink, C. Schuster, F. Reuther, C. Gruetzner, and A. Kristensen, "Comparison of high resolution negative electron beam resists," J Vac. Sci. Technol. B **24**(4), 1776–1779 (2006).

[87] H. Lee, Y. Xiong, N. Fang, W. Srituravanich, S. Durant, M. Ambati, C. Sun, and X. Zhang, "Realization of optical superlens imaging below the diffraction limit," New J. Phys. **7**, 255 (2005).

[88] Z. Liu, M. D. Thoreson, A. V. Kildishev, and V. M. Shalaev, "Translation of nanoantenna hot spots by a metal-dielectric composite superlens," Appl. Phys. Lettt. **95**(3), 033114 (2009).

[89] J. M. Dudley and J. R. Taylor, "Ten years of nonlinear optics in photonic crystal fibre," Nat. Photonics **3**(2), 85–90 (2009).

[90] Z. Liu, A. Boltasseva, R. H. Pedersen, R. Bakker, A. V. Kildishev, V. P. Drachev, and V. M. Shalaev, "Plasmonic nanoantenna arrays for the visible," Metamaterials **2**(1), 4551 (2008).

[91] J. R. Taylor, *An Introduction to Error Analysis*, 2nd ed. (University Science Books, 1997).

[92] F. Lai, L. Lin, R. Gai, Y. Lin, and Z. Huang, "Determination of optical constants and thicknesses of In2O3 : Sn films from transmittance data," Thin Solid Films **515**(18), 7387–7392 (2007).

[93] J. K. Gansel, M. Thiel, M. S. Rill, M. Decker, K. Bade, V. Saile, G. von Freymann, S. Linden, and M. Wegener, "Gold Helix Photonic Metamaterial as Broadband Circular Polarizer," Science **325**(5947), 1513–1515 (2009).

[94] M. W. Klein, C. Enrich, M. Wegener, and S. Linden, "Second-harmonic generation from magnetic metamaterials," Science **313**(5786), 502–504 (2006).

[95] F. Wang and Y. R. Shen, "General properties of local plasmons in metal nanostructures," Phys. Rev. Lett. **97**(20), 206806 (2006).

[96] K.-P. Chen, V. P. Drachev, J. D. Borneman, A. V. Kildishev, and V. M. Shalaev, "Drude Relaxation Rate in Grained Gold Nanoantennas," Nano Lett. **10**(3), 916–922 (2010).

[97] J. Homola, S. Yee, and G. Gauglitz, "Surface plasmon resonance sensors: review," Sensor. Actuat. B-Chem. **54**(1-2), 3–15 (1999).

[98] C. Enrich, M. Wegener, S. Linden, S. Burger, L. Zschiedrich, F. Schmidt, J. F. Zhou, T. Koschny, and C. M. Soukoulis, "Magnetic metamaterials at telecommunication and visible frequencies," Phys. Rev. Lett. **95**(20), 203 (2005).

[99] A. V. Kabashin, P. Evans, S. Pastkovsky, W. Hendren, G. A. Wurtz, R. Atkinson, R. Pollard, V. A. Podolskiy, and A. V. Zayats, "Plasmonic nanorod metamaterials for biosensing," Nat. Mat. **8**(11), 867–871 (2009).

[100] E. Shamonina, V. Kalinin, K. Ringhofer, and L. Solymar, "Imaging, compression and Poynting vector streamlines for negative permittivity materials," Electron. Lett. **37**(20), 1243–1244 (2001).

[101] F. Hao, P. Nordlander, Y. Sonnefraud, P. Van Dorpe, and S. A. Maier, "Tunability of Subradiant Dipolar and Fano-Type Plasmon Resonances in Metallic Ring/Disk Cavities: Implications for Nanoscale Optical Sensing," ACS Nano **3**(3), 643–652 (2009).

[102] N. Liu, T. Weiss, M. Mesch, L. Langguth, U. Eigenthaler, M. Hirscher, C. Soennichsen, and H. Giessen, "Planar Metamaterial Analogue of Electromagnetically Induced Transparency for Plasmonic Sensing," Nano Lett. **10**(4), 1103–1107 (2010).

[103] M. Svedendahl, S. Chen, A. Dmitriev, and M. Kall, "Refractometric Sensing Using Propagating versus Localized Surface Plasmons: A Direct Comparison," Nano Lett. **9**(12), 4428–4433 (2009).

Appendix A

Ph.D. publications

Publications submitted as part of the Ph.D. thesis. The publications are referred to in the text by roman numerals.

I. **C. Jeppesen**, R. B. Nielsen, A. Boltasseva, S. Xiao, N. A. Mortensen, and A. Kristensen, *Thin film Ag superlens towards lab-on-a-chip integration*, Opt. Express, **17**(25), 22543-22552 (2009). Selected for the Virtual Journal for Biomedical Optics, Volume 5, Issue 1, Jan. 4, 2010.

II. **C. Jeppesen**, N.A. Mortensen, and A. Kristensen, *Capacitance tuning of nanoscale split-ring resonators*, Appl. Phys. Lett., **95**(19), 193108 (2009). Selected for the Virtual Journal of Nanoscale Science & Technology, Nov. 16, 2009.

III. **C. Jeppesen**, S. Xiao, N.A. Mortensen, and A. Kristensen, *Extended verification of scaling behavior in split-ring resonators*, Opt. Commun., **284**, 799-801 (2011).

IV. **C. Jeppesen**, N.A. Mortensen, and A. Kristensen, *The effect of Ti and ITO adhesion layers on gold split-ring resonators*, Appl. Phys. Lett., Accepted (2010).

V. **C. Jeppesen**, S. Xiao, N.A. Mortensen, and A. Kristensen, *Metamaterial localized resonance sensors: prospects and limitations*, Opt. Express, **18**(24), 25075-25080 (2010).

A.1 Paper I

- **C. Jeppesen**, R. B. Nielsen, A. Boltasseva, S. Xiao, N. A. Mortensen, and A. Kristensen, *Thin film Ag superlens towards lab-on-a-chip integration*, Opt. Express, **17**(25), 22543-22552 (2009).

Thin film Ag superlens towards lab-on-a-chip integration

C. Jeppesen,[1] R. B. Nielsen,[2] A. Boltasseva,[2] S. Xiao,[2]
N. A. Mortensen,[2] and A. Kristensen[1]

[1]*Department of Micro and Nanotechnology, Technical University of Denmark, DTU
Nanotech, DTU-building 345 east, DK-2800 Kongens Lyngby, Denmark*
[2]*Department of Photonics Engineering, Technical University of Denmark, DTU Fotonik,
DTU-building 345 west, DK-2800 Kongens Lyngby, Denmark*

anders@mailaps.org

Abstract: A thin metal film near-field superlens, as originally suggested by Pendry and realized by Fang *et al.* and Melville *et al.*, is investigated with emphasis on materials suitable for integration on a lab-on-a-chip platform. A chemically resistant cyclo-olefin copolymer (COC), mr-I-T85 from microresist technology, is applied as dielectric matrix/spacer for an Ag thin film superlens. The superlens successfully resolves 80 nm half-pitch gratings when illuminated with UV radiation at a free space wavelength of 365 nm. The superlens design, fabrication and characterization is discussed.

© 2009 Optical Society of America

OCIS codes: (250.5403) Plasmonics, (220.0220) Optical design and fabrication, (220.4241) Nanostructure fabrication

---

References and links

1. J. B. Pendry and D. R. Smith, "Reversing light with negative refraction," Phys. Today **57**, 37 – 43 (2004).
2. J. B. Pendry, "Negative refraction makes a perfect lens," Phys. Rev. Lett. **85**, 3966 – 3969 (2000).
3. N. Fang, H. Lee, C. Sun, and X. Zhang, "Sub-diffraction-limited optical imaging with a silver superlens," Science **308**, 534 – 537 (2005).
4. D. O. S. Melville and R. J. Blaikie, "Super-resolution imaging through a planar silver layer," Opt. Express **13**, 2127 – 2134 (2005).
5. V. M. Shalaev and M. I. Stockman, "Optical properties of fractal clusters (susceptibility, surface enhanced Raman scattering by impurities)," Sov. Phys. JETP **65**, 509–522 (1987).
6. Z. T. Liu, M. D. Thoreson, A. V. Kildishev, and V. M. Shalaev, "Translation of nanoantenna hot spots by a metal-dielectric composite superlens," Appl. Phys. Lett. **95**, 033 114 (2009).
7. R. Holt and T. Cotton, "Surface-enhanced resonance Raman and electrochemical investigation of Glucose oxidase catalysis at a silver electrode," J. Am. Chem. Soc. **111**, 2815–2821 (1989).
8. M. Yang, F. Chung, and M. Thompson, "Acoustic network analysis as a novel technique for studying protein adsorption and denaturation at surfaces," Anal. Chem. **65**, 3713–3716 (1993).
9. K. Brown, A. Fox, and M. Natan, "Morphology-dependent electrochemistry of cytochrome c at Au colloid-modified SnO2 electrodes," J. Am. Chem. Soc. **118**, 1154–1157 (1996).
10. T. A. P. GmbH, "TOPAS Advanced Polymers," www.topas.com (2009).
11. R. R. Lamonte and D. McNally, "Uses and processing of cyclic olefin copolymers," Plast. Eng. **56**, 51–55 (2000).
12. O. Gustafsson, K. B. Mogensen, and J. P. Kutter, "Underivatized cyclic olefin copolymer as substrate material and stationary phase for capillary and microchip electrochromatography," Electrophoresis **29** (2008).
13. M. J. Weber, *Handbook of optical materials* (CRC Press, Boca Raton, 2003).
14. M. Scholer and R. J. Blaikie, "Simulations of surface roughness effects in planar superlenses," J. Opt. A: Pure Appl. Opt. **11**, 105 503 (2009).
15. H. Lee, Y. Xiong, N. Fang, W. Srituravanich, S. Durant, M. Ambati, C. Sun, and X. Zhang, "Realization of optical superlens imaging below the diffraction limit," New J. Phys. **7**, 255 (2005).
16. P. Chaturvedi, K. Hsu, S. Zhang, and N. Fang, "New frontiers of metamaterials: design and fabrication," MRS Bull. **33**, 915 – 920 (2008).

17. L. Vj, N. P. Kobayashi, M. S. Islam, W. Wu, P. Chaturvedi, N. X. Fang, S. Y. Wang, and R. S. Williams, "Ultra-smooth Silver Thin Films Deposited with a Germanium Nucleation Layer," Nano Lett. **9**, 178–182 (2009).

1. Introduction

The diffraction limit is traditionally considered to impose a fundamental obstacle for optical imaging of nanometer scale objects and macro-molecules. The emergence of metamaterial concepts is challenging this classical prejudice [1] — in particular, the superlens, as originally proposed by Pendry [2]. A flat silver slab interfaced with a dielectric layer that has a matching real part of the relative permittivity ($\varepsilon_{metal} = -\varepsilon_{dielectric}$) can serve as a superlens in the UV to IR region. Such a lens can image objects in the near-field below the classical diffraction limit. As an example Fang *et al.* [3] demonstrated near-field imaging resolving 60 nm features using UV radiation at a vacuum wavelength of 365 nm. Fang's superlens structure consisted of a quartz wafer, a focused ion beam (FIB) written grating pattern in a 50 nm Cr film, a 40 nm polymethyl-methacrylate (PMMA) spacer layer, a 35 nm thick Ag film, and finally 100 nm of the negative photoresist NFR105G. The image of the grating structures was recorded in the photoresist by UV-exposure - at wavelength 365 nm - through the grating and the thin film superlens, see Fig. 1. The exposure took place using a standard I-line aligner and they managed to resolve 60 nm half-pitch (Λ) gratings corresponding to features of the order $\lambda/6$. Almost simultaneously Melville *et al.* [4] demonstrated near-field superlensing by employing the same lithography readout mechanism.

These investigations have focused on demonstrating the sub-wavelength imaging capabilities and exploring their fundamental nature rather than actual applications of such devices. The non-invasive nature of optical probing is inherently attractive in biotechnology and lab-on-a-chip. One such application could be spatial translation of localized electromagnetic fields, also known as "hot spots" [5] for enhanced flourescence microscopy. Hot spots are produced by metal nanoantennas and can be used in sensing applications including surface-enhanced Raman scattering (SERS) and enhanced fluorescence microscopy [6]. The field enhancement is inversely proportional to the distance between the nanoantennas and the fluorophores. Direct contact, however, might result in undesirable structural or functional changes of the biomolecules [7] such as the denaturation of proteins [8, 9]. This can be avoided by using a Ag near-field superlens to transfer the "image" of the hot spots to the biomolecules, thereby enabling a spatial distance between the nanoanteannas and the molecules. In this way chemical interaction, between the biomolecules and the antenna is suppressed. This motivates our investigations of superlens concepts in lab-on-a-chip systems, reported in this paper. We therefore consider the choice of materials, which should be compatible with the down-stream micro-fabrication steps, required to integrate the superlens with micro and nanofluidic components in a lab-on-a-chip.

In comparison to Fang's device [3], we have replaced PMMA by a likewise biocompati-
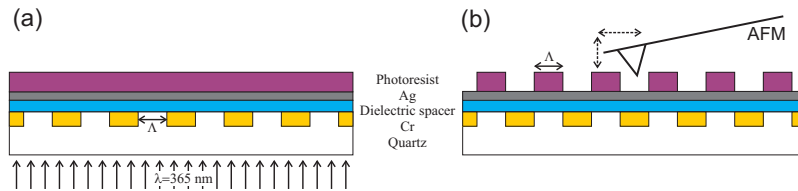

Fig. 1. Near-field superlens design using UV-lithography readout. (a) Exposure of negative photoresist through the quartz/Cr mask and the Ag superlens of a grating pattern with period 2Λ. (b) AFM scan of the exposed and developed photoresist.
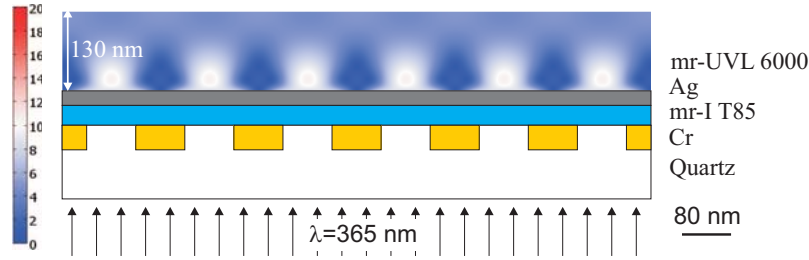
Fig. 2. Finite element simulation of the intensity-distribution $(|E|/|E_0|)^2$ for six grating periods illuminated by 365 nm radiation. The grating has a half-pitch of 80 nm.

ble, but highly chemical resistant cyclic-olefin copolymer (COC) called mr-I T85. The relative permittivity of mr-I T85 is $\varepsilon_{T85} = 2.415$ at 365 nm and thereby matches the value of silver ($\varepsilon_{Ag} = -2.401$) better than that of PMMA ($\varepsilon_{PMMA} = 2.301$). Compared to PMMA, COC based materials are more heat resistant, have a lower water absorption, and are more chemically resistant [10, 11]. COC materials have demonstrated superior transmission in the UV region [10], thereby enabling absorption measurements in lab-on-a-chip systems at λ=254 nm [12]. These combined properties make COC materials far more suitable than PMMA for lab-on-a-chip applications. Due to the well matching permittivities of silver and mr-I T85, mr-I T85 was preferred compared to common dielectrics such as SiO$_2$ ($\varepsilon_{SiO_2} = 2.25$ [4]) or Al2O3 ($\varepsilon_{Al_2O_3} = 3.217$ [13]).

In addition are a different photoresist, the mr-UVL 6000 ($\varepsilon_{mr6000} = 2.719$) and the patterns are e-beam written instead of FIB written. Furthermore, the chrome pattern is embedded into the quartz wafer to ease the planarization process. In the following, the design considerations and fabrication issues are discussed together with the optical performance of the COC based superlens devices.

2. Design considerations

To support our design of the grating structure we take advantage of full-wave simulations of the transmitted field. We employ a commercially available finite-element method (Comsol Multiphysics) which solves the wave equation, Eq. 1

$$\nabla \times \nabla \times E = \frac{\omega^2}{c^2} \varepsilon E, \tag{1}$$

with an incident electrical field E_0 polarized perpendicular to the grading lines. The system is depicted in Fig. 2 where we apply perfectly-matched layers (PMLs) for the horizontal domain boundaries while periodic boundary conditions are employed for the vertical domain boundaries. The figure shows the intensity-distribution $(|E|/|E_0|)^2$ for 365 nm radiation normally incident on a half-pitch of Λ=80 nm. For the material properties we employ $n = 1.475$ for the quartz, $n = 1.40 + i3.25$ for Cr, $n = 0.407 + i4.43$ for Al, $n = 1.554$ for mr-I T85 corresponding to $\varepsilon = 2.415$, $\varepsilon = -2.401 + i0.2488$, and $n = 1.649$ for mr-UVL 6000. The different length scales correspond to those of the fabricated structure, as discussed in the fabrication section.

In Fig. 2, the intensity distribution shows six "peaks" that can be associated with the six windows in the chrome mask. If the peaks are given an above-threshold dose, some residual layer exposure is to be expected. In Fig. 3(a)-(c) we summarize further modeling of structures with different grating periods, Λ=60-80 nm.
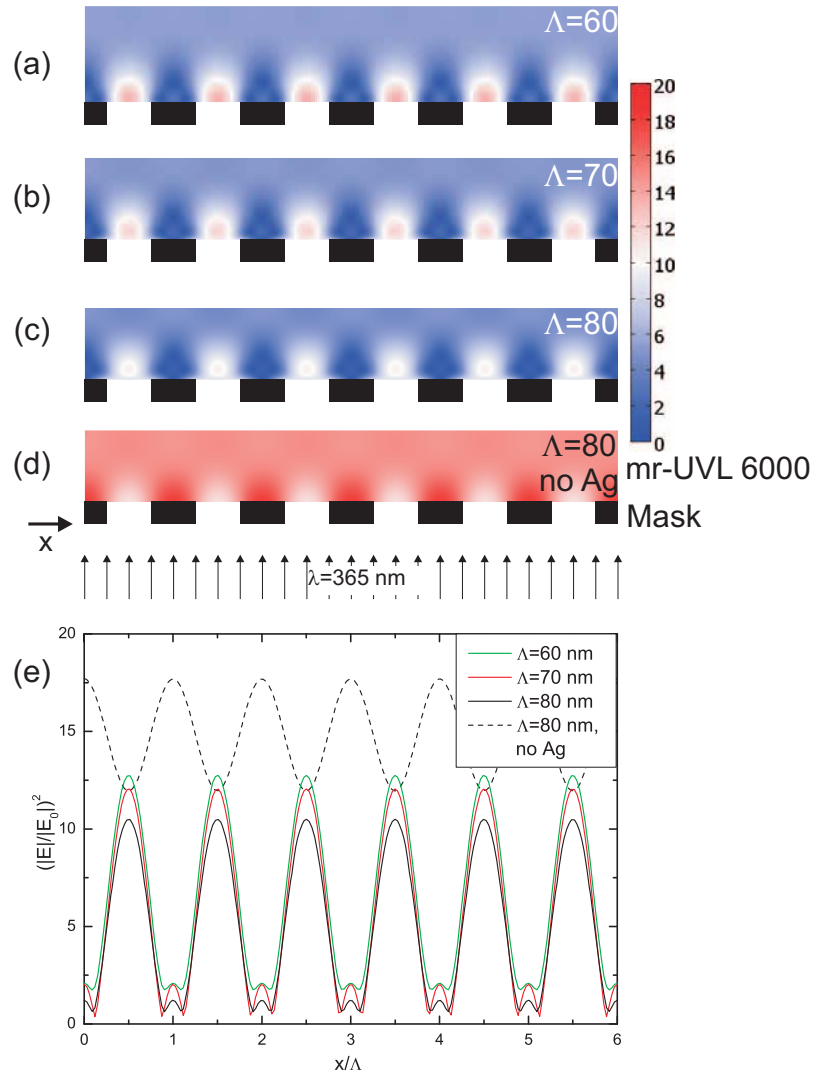
Fig. 3. Finite-element modeling of the intensity-distribution $(|E|/|E_0|)^2$ above the super-lens when illuminated through gratings of different period. To simplify the plot and ease comparison, the mr-I T85 and the silver layers are not depicted. Panels (a)-(c) are with Λ=60, 70, and 80 nm and a silver superlens film. Panel (d) is a reference with Λ=80 nm where the 35 nm Ag layer has been replaced by 35 nm of mr-I T85. Panel (e) is the intensity cross-section 15 nm into the resist as a function of the normalized position x with respect to the grating period Λ.

As the period increases, the six intensity peaks in the resist are gradually smeared out illustrated by the slight decrease in contrast. We emphasize that for the particular design of the grading structure, the 80 nm grating is the largest period where six individual peaks are easily identifiable. For demonstration purposes we have thus pursued a silver superlens design which is able to resolve features corresponding to a grating with an 80 nm half-pitch. As a control structure, Fig. 3(d) illustrates the situation where the silver is replaced by mr-I T85. The six peaks are visible but the contrast is poor compared to the silver superlens, see Fig. 3(e). The high intensity peaks are positioned in front of the mask instead of the mask openings contrary to Fig. 3(a)-(c). This indicates that without the silver film we obtain a diffraction pattern.

3. Fabrication

The fabrication, see Fig. 4, can be split into two parts: The fabrication of the mask and the fabrication of the superlens stack. A 100 nm ZEP520A (3.6%, Zeon Corp., Tokyo, Japan) layer is spincoated onto a 1 mm fused silica substrate. Subsequently, a 15 nm aluminium layer is thermally deposited on top of the ZEP layer to prevent charge accumulation during the following electron beam lithography (EBL) step. The proximity corrected EBL exposure is done with a 100 kV JEOL JBX-9300FS EBL tool (120 μC/cm^2 dose, 0.6 nA current, 4 nm spot-size). The pattern consists of 30×30 μm areas of 70-120 nm half-pitch gratings and 30-150 nm isolated lines. The aluminium layer is removed in 1 min of undiluted MF-322 (Rohm and Haas, Coventry, UK) and the positive ZEP resist is developed 1 min in ZED-N50 (Zeon Corp.) developer followed by an IPA rinse. Then a brief descum process (asher, 5 min, 70 sccm O2, 70 sccm N2, 150 W) is carried out to remove any residual resist. Subsequently, a reactive ion etching (RIE, 1 min 40 s, 24 sccm CF4, 42 sccm CHF3, 24 W, 16 mTorr) process is used to etch 50 nm into the glass. 50 nm Cr is then embedded into the fused silica by electron beam deposition and the wafer is immersed into Remover 1165 (Rohm and Haas) with ultrasound for 2 hours, which dissolves the ZEP layer. Embedding the Cr mask ensures a more even surface and thereby simplifies the later planarization process. The wafer is placed in a HMDS-oven and 1.5 μm of positive photoresist AZ5214e is spincoated on. The wafer is exposed in an I-line aligner with a dose of 70 mJ/cm^2 through a mask with 20×20 μm windows and subsequently developed. A 50 nm Al cover is thermally deposited to block all light that does not go through the quartz/chrome mask from reaching the mr-UVL 6000 layer. This is to minimize waveguiding in the photoresist during the exposure. The AZ5214e layer is removed in acetone, which marks the conclusion of the mask structure, see Fig. 5.

The height of the Al layer is then measured by AFM. The next step is the superlens stack, which consists of a 40 nm mr-I T85 planarization layer, a 35 nm Ag layer and 70 nm mr-UVL 6000. The thickness of the mr-UVL 6000 is chosen to minimize waveguiding within the resist. First 300 nm mr-I T85 is spincoated onto the wafer, etched in the RIE (2 min, 20 sccm O2, 99 sccm N2, 20 W), given a 1 min oxygen plasma (asher) to planarize the surface and to reflow the mr-I T85. The thickness of the mr-I T85 layer is measured by ellipsometry and the profile across the mask areas is measured. By combining this information with the height of the aluminium layer and the etch rate, the remaining etch time can be estimated. The wafer is RIE etched again and given 1 min oxygen plasma. The thickness is measured by ellipsometry to 40 nm$\pm$2.5 nm and the roughness Rq over a 5×5 μm area is 0.5 nm. Then 35 nm of Ag is deposited by e-beam deposition at a rate of 1.5 Å/s and 70 nm of mr-UVL 6000 is spincoated on top. The Rq roughness of the Ag layer is 0.8 nm, see Fig. 6. Spincoating of mr-UVL 6000 concludes the fabrication process.
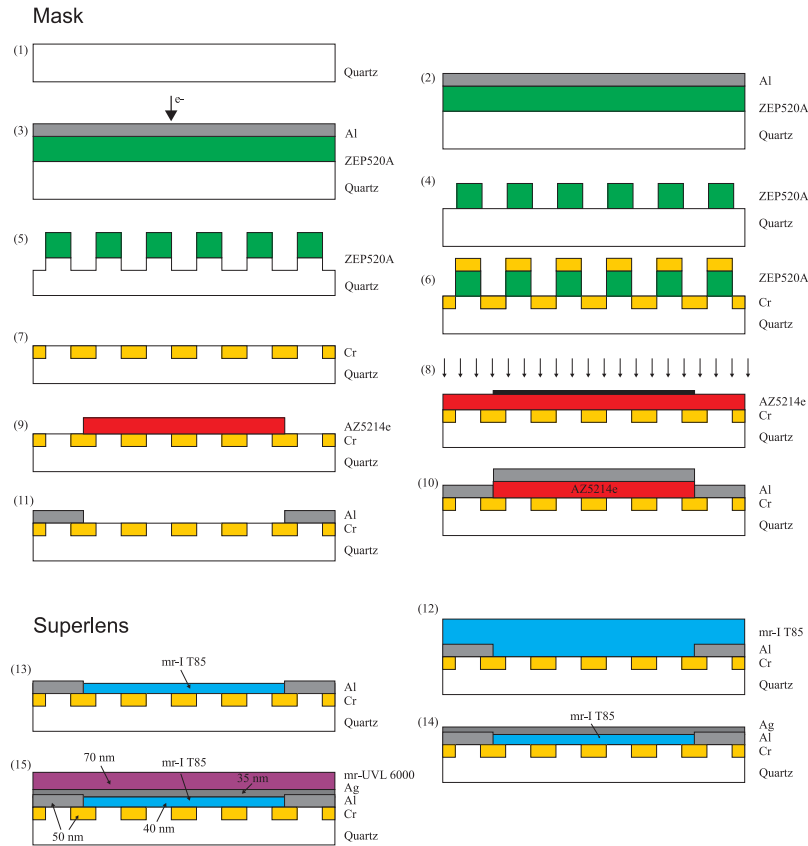
Fig. 4. Schematic drawing of the processflow. (1) Quartz wafer. (2) Spincoat of ZEP520A and deposition of Al. (3) EBL exposure. (4) Development. (5) RIE etch quartz. (6) Deposition of Cr. (7) Removal of ZEP520A. (8) UV-lithography of AZ5214e. (9) Development. (10) Al deposition. (11) Lift-off. (12) Spincoat mr-I T85. (13) RIE etch mr-I T85. (14) Ag deposition. (15) Spincoat mr-UVL 6000.
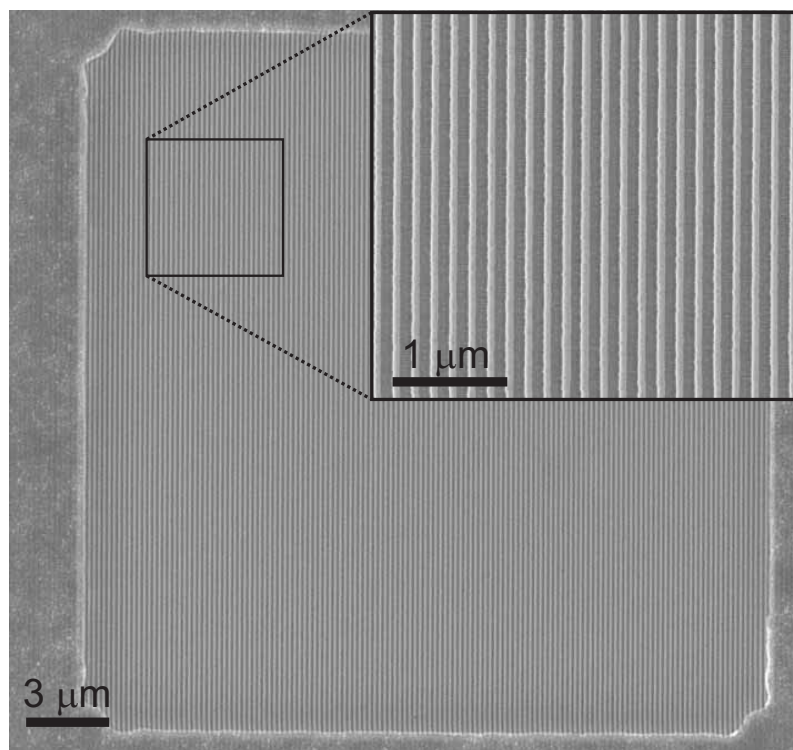
Fig. 5. SEM image of the 20×20 μm opening in the Al layer to the 80 nm half-pitch quartz/chrome gratings.

4. Results

The fabricated superlens devices were optically characterized by I-line (365 nm) UV flood exposure in a contact aligner applying a dose of 750 mJ/cm^2. After exposure, the mr-UVL 6000 was given a post exposure bake at 120°C for 5 min followed by a 50 s development step in Propylene Glycol Methyl Ether Acetate (PGMEA). The exposed and developed structures were then characterized by AFM, see Fig. 7. To verify that the periodic structure was indeed due to a superlensing effect, a control wafer was made where the silver layer was replaced by mr-I T85. This gives the same distance between the mask and the resist, but without the silver it should not be possible to reproduce the grating structure in the photoresist. The result can be seen in Fig. 7(b).

As seen in Fig. 7(a) and (c), the 80 nm half-pitch gratings are well reproduced in the photoresist. The image of the gratings is clearly of a lower quality than the original mask, see Fig. 6(a). This could indicate that the superlens was unable to restore all the Fourier components e.g. fast decaying high order components. Furthermore, photolithography represents an indirect and far from ideal readout mechanism of the incident light intensity where the resist's dose-response curve acts as the transfer function from the light intensity to the exposed resist. Additionally, the surface roughness of the silver has a large effect on the resolution and thereby image quality. The peak to valley distance in the AFM scan is only around 1 nm. Several factors may have
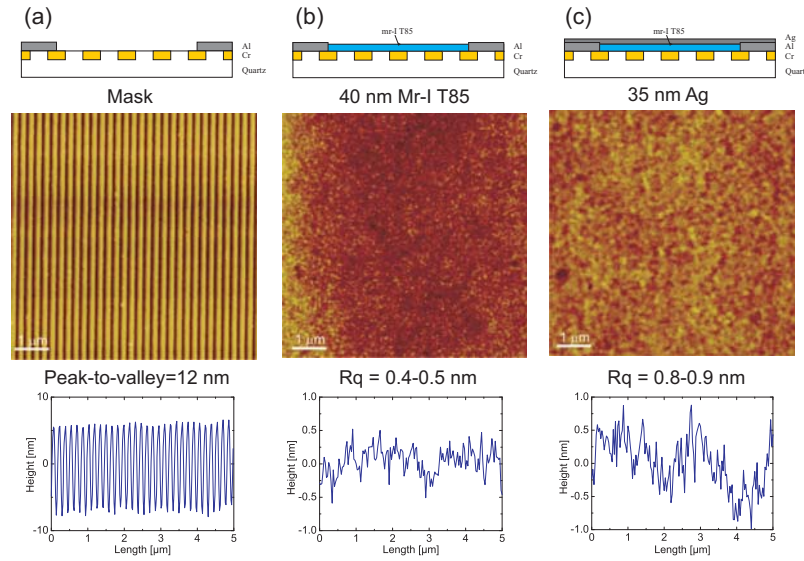
Fig. 6. The fabricated near-field superlens. AFM micrographs and surface profiler scans after different process steps: (a) Cr mask with 80 nm half-pitch on glass substrate. (b) Spin-coating and back-etch of 40 nm thick mr-I T85 film, which serves as dielectic matrix/spacer. A surface roughness Rq below 0.5 nm is achieved. (c) 35 nm Ag film, with a Rq below 0.9 nm.

contributed to this. AFM tip convolution can result in shallower valleys since the tip has a finite size and taper. A large contribution can also be ascribed to the residual layer exposure, which can be clearly seen in the simulations, see Fig. 2.

From the simulations it is expected that more than half of the resist height is a result of residual layer exposure assuming that the threshold of the resist is reached at half maximum of the intensity. Other factors relate to the chemical processes occurring in the resist during exposure, baking and development. Out of the different grating sizes, the 80 nm half-pitch gratings are the easiest to identify. Pattern defects are caused by height variations of the mr-I T85 layer and areas of higher surface roughness. For the 70 nm gratings the Ag roughness might be too large for the gratings to be properly resolved since there is an inverse proportionality between resolution and surface roughness [14, 15, 16]. The control wafer with 75 nm mr-I T85 instead of 40 nm mr-I T85 and 35 nm Ag shows no sign of image contrast, see Fig. 7(c). The missing grating structure evidently supports that the previous results were caused by enhancement of the evanescent field at the metal/dielectric interfaces due to surface plasmons. We measured the dose-response curve (retention height vs. exposure dose) and have used a dose corresponding to maximum slope on the dose curve. Although no systematic study was made, we have tested different doses around the maximum slope point. However, we did not observe any contrast improvements.

The evanescent wave has a characteristic decay length, Eq. 2 [15]

$$Z = \frac{1}{4\pi} \frac{1}{\sqrt{a^{-2} - \varepsilon \lambda^{-2}}},$$ (2)

where a is the period and λ is the free space wavelength. In the present case we get 17 nm
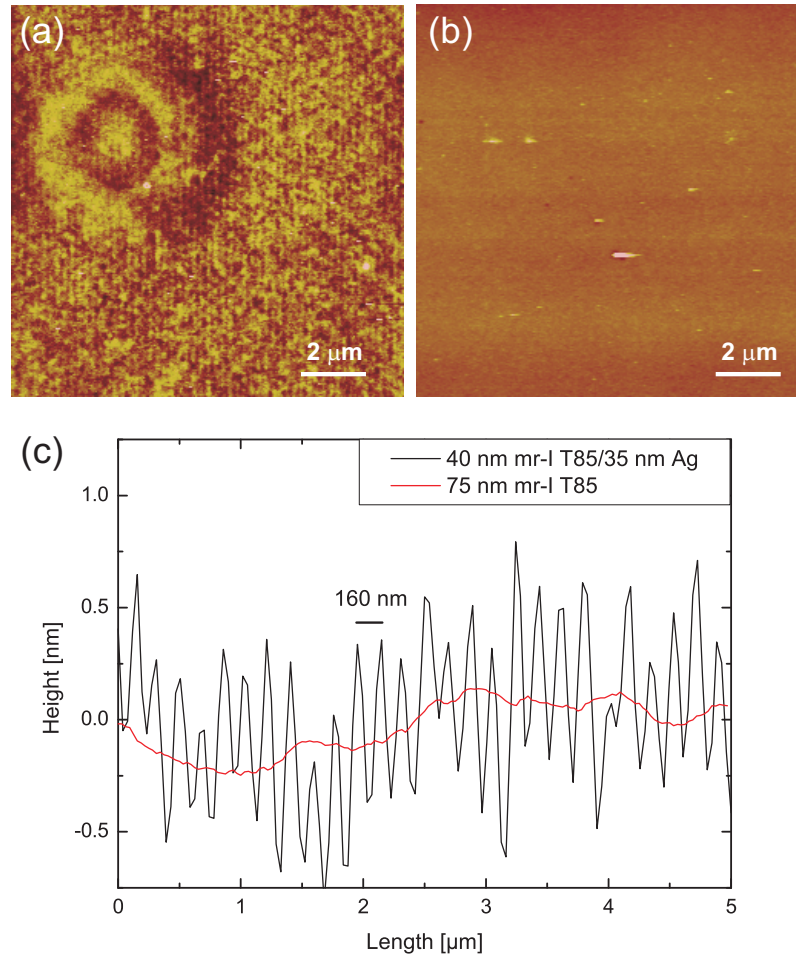
Fig. 7. (a) 8×8 μm AFM scan of the recorded image of 80 nm half-pitch gratings in the mr-UVL 6000 resist. The exposure was done through the Ag superlens. (b) 8×8 μm AFM scan of the obtained image of 80 nm half-pitch gratings in the resist where the Ag layer was replaced with mr-I T85. (c) Height scan of the images (a) and (b).

so that the field intensity is reduced to $1/e = 0.37$ of its original value within the first 17 nm beyond the mask. After 75 nm the intensity of the evanescent wave is therefore expected to be minor. An advantage of embedding the structure is that a single mr-I T85 layer can be used for planarization but also that the dielectric planarization layer can be reduced in thickness. According to Lee *et al.* [15], a thinner spacer layer than the 40 nm would drastically increase the transmissivity of evanescent waves. Initial tests have shown that the mr-I T85 thickness can be reduced below 40 nm without compromising the surface roughness. 30 nm spacer layers should be possible, which should improve the quality of the recorded image significantly. Recent developments in Ag deposition can further improve the image quality [17].

5. Conclusion

We have demonstrated superlensing by reproducing a 80 nm half-pitch grating structure in a negative photoresist using 365 nm vacuum wavelength UV radiation. The results were supported by finite-element modeling of the field-distribution in the resist. With the current materials the superlens is suitable for integration in nanofluidic systems but further optimization and initial tests on arbitrary objects should be carried out in advance.

The integrated silver superlens will provide all the advantages of surface enhanced spectroscopy without having the sample molecules in the vicinity of the metal surfaces causing the field enhancement. As examples, the microfluidic device with integrated thin film superlens and plasmonic nanoantennas, will enable field enhanced remote probing of biomolecules without pertubing the electrochemical environment of the suspended biomolecules. The lab-on-a-chip with integrated superlens therefore has high potential impact on chip based protein detection, where the remoteness of lens and nanoantennas may prevent undesirable structural or functional changes of the biomolecules such as the denaturation of proteins.

Acknowledgments

A.2 Paper II

- **C. Jeppesen**, N.A. Mortensen, and A. Kristensen, *Capacitance tuning of nanoscale split-ring resonators*, Appl. Phys. Lett., **95**(19), 193108 (2009).

Capacitance tuning of nanoscale split-ring resonators

Claus Jeppesen,[1] Niels Asger Mortensen,[2] and Anders Kristensen[1,a)]
[1]*Department of Micro and Nanotechnology, Technical University of Denmark, DTU Nanotech,
Building 345 East, DK-2800 Kongens Lyngby, Denmark*
[2]*Department of Photonics Engineering, Technical University of Denmark, DTU Fotonik, Building 345 West,
DK-2800 Kongens Lyngby, Denmark*

We investigate the capacitance tuning of nanoscale split-ring resonators. Based on a simple inductor-capacitor circuit model, we derive an expression, where the inductance is proportional to the area while the capacitance reflects the aspect ratio of the slit. The resonance frequency may thus be tuned by the slit aspect ratio leaving the area, the lattice constant Λ, and nearest-neighbor coupling in periodic structures invariant. Experimental data follow the predictions of the simple LC-model. © 2009 American Institute of Physics. [doi:10.1063/1.3263191]

Metamaterials are artificially structured electromagnetic materials with exceptional optical properties inherited from the structure of the subwavelength, mesoscopic unit-cell. By carefully designing the unit-cell, materials can be facilitated with a negative effective index supporting negative refraction of incident waves.[1] The realization of negative-index media combines structures supporting a negative permittivity ϵ_{eff} as well as a negative permeability μ_{eff}. While the plasmonic response of metals already supports the former at optical frequencies, there is a call for geometries also supporting an artificial negative magnetic response. Cut-wires,[2] "fish-net" structures,[3] and particularly different types of split-ring resonator geometries[4–6] are central in this context.

Since the seminal work by Pendry *et al.*,[7] artificial magnetism has been demonstrated at yet higher frequencies.[8] Recently, split-ring resonators (SRR) have been realized at terahertz frequencies,[4,9] near-infrared, and visible frequencies.[6,10] Scaling properties and coupling effects have been subject to numerous theoretical, numerical, and experimental studies.[11–16]

The strong analogy with inductor-capacitor (LC) circuits has motivated substantial efforts in establishing simple circuit models, allowing for an estimate of the resonance frequency

$$\omega_0 \simeq 1/\sqrt{LC}, \qquad (1)$$

in terms of geometrical parameters of the SRR structure, see, e.g., Refs. 14 and 16 and references therein. In particular, a linear scaling of the structure causes a simple scaling of the resonance frequency [Eq. (1)], which is inversely proportional to the scale factor.[17] The concept of scaling applies as long as the metal can be perceived as an ideal metal. Deviations of linear scaling have been observed at optical frequencies.[10] At lower frequencies the kinetic inductance of the electrons may be neglected and the artificial magnetic response has a purely geometrical origin.[18] The capacitive response of the SRRs has also been investigated by applying a voltage across the SRRs.[19,20]

In this letter we consider single-slit SRRs and emphasize how the inductance L mainly probes the area $\ell \times \ell$ of the

SRR, while the capacitance C relates to the slit dimension. Obviously, the latter property allows tuning of the frequency, while leaving the area, the lattice constant Λ, and nearest-neighbor coupling in periodic structures invariant.

We apply a simple model of the scaling for the resonance frequency with the slit aspect-ratio d/w. Predictions are confirmed by measurements on a large range of SRR samples fabricated by electron-beam lithography (EBL).

In the simplest approach, the SRR geometry in Fig. 1 resembles a plate capacitor with capacitance $C = \varepsilon_0 wh/d$, where h is the metal-film thickness, d is the slit width, and w is the slit length.

Inductance wise, the SRR geometry mimics a single-loop coil with inductance $L = \mu_0(1/h)^2(\ell \times \ell)h$, where $\ell \times \ell$ is the area of the coil. This yields a resonance frequency[14]

$$\omega_0 = \frac{c}{\ell}\sqrt{\frac{d}{w}}, \qquad (2)$$

where $c = 1/\sqrt{\epsilon_0\mu_0}$.

To assess this simple model we have prepared eight samples with arrays of SRR, see Fig. 2, each covering an area of 2 mm $\times$ 2 mm. The transmission is measured using a 1 mm diameter laser spot, thus effectively probing an ensemble of 10^8–10^9 SRRs.

In fabrication, a 100 nm thick layer of EBL resist, ZEP520A (3.6%, Zeon Corp., Tokyo, Japan) is spincoated onto a 1 mm fused silica substrate. A 15 nm aluminum layer is thermally deposited on top of the ZEP layer to prevent charge accumulation during EBL. The proximity corrected EBL exposure is performed with a 100 kV JEOL JBX-
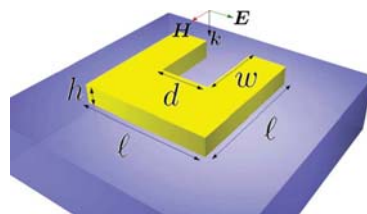

FIG. 1. (Color online) Schematic drawing of the SRR design, indicating central geometrical parameters as well as the polarization configuration of the excitation.

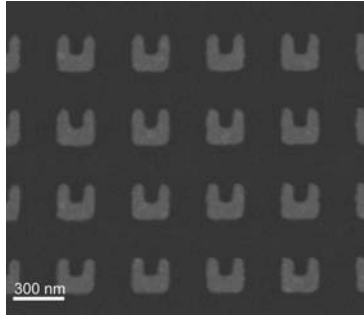a)Author to whom correspondence should be addressed. Electronic mail: anders@mailaps.org.

95, 193108-1

FIG. 2. Micrograph of a SRR array with pitch $\Lambda=440$ nm. The fabricated samples have $\ell=200$ nm, $w=90–110$ nm, $d=80$ nm, and $h=30$ nm.

9300FS EBL tool (200 μC/cm^2 dose, 2 nA current, and 6 nm spotsize). The aluminum layer is then removed in MF-322 (Rohm and Haas, Coventry, U.K.) and the positive ZEP resist is developed in ZED-N50 (Zeon Corp.) developer. A brief O$_2$ plasma descum process is applied to remove residual resist before 5 nm Ti/30 nm Au is deposited by electron beam deposition. The final lift-off is performed by using Remover 1165 (Rohm and Haas) in an ultrasound bath.

Figure 3 shows normal-incidence transmittance spectra for four samples with the polarization given in Fig. 1. The spectra show a resonance shift toward shorter wavelengths, hence larger frequencies ($\lambda_0=2\pi c/\omega_0$) as a function of as-
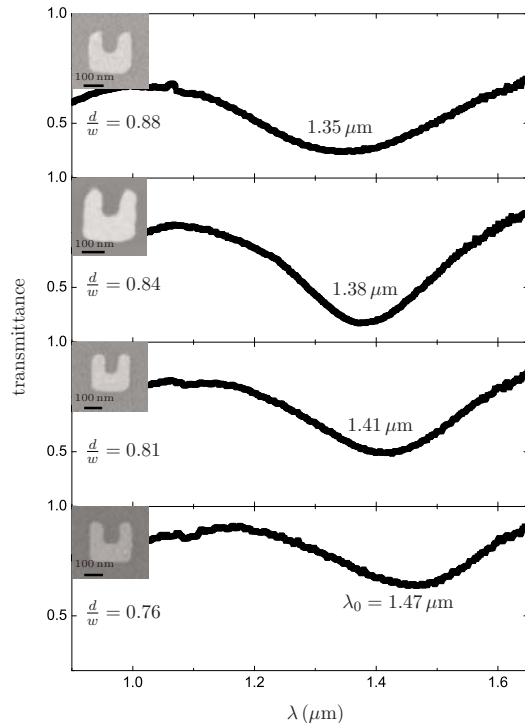

FIG. 3. (Color online) Measured normal incidence transmittance spectra for four samples with $\ell=200$ nm and $d=80$ nm. The resonance wavelength λ_0, the ratio d/w, and a micrograph for each sample is given.
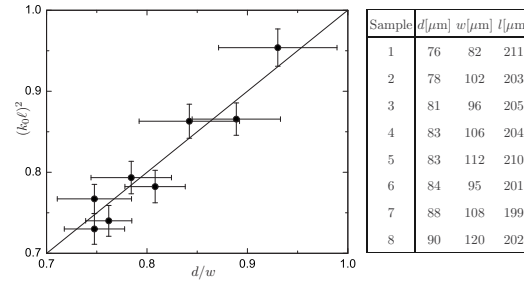

FIG. 4. Plot of $(k_0\ell)^2$ vs d/w. The corresponding SRR dimensions are listed in the table. The solid line shows Eq. (3) without any free parameters. The x-error bars represent the standard deviation (SD) of ten individual measurements of w and d added together. The y-error bars is the 1 nm spectral resolution of the Ando AQ-6315E optical spectrum analyzer added to the SD of ten measurements of the length ℓ.

pect ratio d/w. This is in good agreement with the predictions of Eq. (2).

In Fig. 4 we compare the measurements to our model. For a clearer confirmation of the scaling with the slit-aspect ratio d/w, we rewrite Eq. (2) as

$$(k_0\ell)^2 = \frac{d}{w}, \tag{3}$$

using $\lambda_0=2\pi/k_0$. Thus giving a linear relationship between the free-space wave number, k_0, and the slit aspect ration, d/w. Clearly, the experimental data confirms this scaling. Within the measurement uncertainties we even find quantitative agreement with our simple model.

In conclusion, we have fabricated metamaterials consisting of periodic arrays of subwavelength, nanoscale SRR. The structures offer an artificial magnetic response around 1400 nm wavelength. Our key observation is that the capacitance of SRR may be tuned by simple geometrical means without affecting the inductance significantly. This allows for frequency scaling without changing the over-all scale of the SRR and/or the lattice constant of the periodic lattice of SRRs.

[1] J. B. Pendry and D. R. Smith, Phys. Today **57**, 37 (2004).
[2] V. M. Shalaev, W. S. Cai, U. K. Chettiar, H. K. Yuan, A. K. Sarychev, V. P. Drachev, and A. V. Kildishev, Opt. Lett. **30**, 3356 (2005).
[3] S. Zhang, W. J. Fan, K. J. Malloy, S. R. J. Brueck, N. C. Panoiu, and R. M. Osgood, Opt. Express **13**, 4922 (2005).
[4] T. J. Yen, W. J. Padilla, N. Fang, D. C. Vier, D. R. Smith, J. B. Pendry, D. N. Basov, and X. Zhang, Science **303**, 1494 (2004).
[5] N. Katsarakis, G. Konstantinidis, A. Kostopoulos, R. S. Penciu, T. F. Gundogdu, M. Kafesaki, E. N. Economou, T. Koschny, and C. M. Soukoulis, Opt. Lett. **30**, 1348 (2005).
[6] C. Enrich, M. Wegener, S. Linden, S. Burger, L. Zschiedrich, F. Schmidt, J. F. Zhou, T. Koschny, and C. M. Soukoulis, Phys. Rev. Lett. **95**, 203901 (2005).
[7] J. B. Pendry, A. J. Holden, D. J. Robbins, and W. J. Stewart, IEEE Trans. Microwave Theory Tech. **47**, 2075 (1999).
[8] C. M. Soukoulis, S. Linden, and M. Wegener, Science **315**, 47 (2007).
[9] S. Linden, C. Enrich, M. Wegener, J. F. Zhou, T. Koschny, and C. M. Soukoulis, Science **306**, 1351 (2004).
[10] M. W. Klein, C. Enrich, M. Wegener, C. M. Soukoulis, and S. Linden, Opt. Lett. **31**, 1259 (2006).

[11]N. Katsarakis, T. Koschny, M. Kafesaki, E. N. Economou, and C. M. Soukoulis, Appl. Phys. Lett. **84**, 2943 (2004).

[12]C. Rockstuhl, F. Lederer, C. Etrich, T. Zentgraf, J. Kuhl, and H. Giessen, Opt. Express **14**, 8827 (2006).

[13]H. C. Guo, N. Liu, L. W. Fu, T. P. Meyrath, T. Zentgraf, H. Schweizer, and H. Giessen, Opt. Express **15**, 12095 (2007).

[14]H. C. Guo, N. Liu, L. W. Fu, H. Schweizer, S. Kaiser, and H. Giessen, Phys. Status Solidi B **244**, 1256 (2007).

[15]M. Decker, S. Linden, and M. Wegener, Opt. Lett. **34**, 1579 (2009).

[16]T. D. Corrigan, P. W. Kolb, A. B. Sushkov, H. D. Drew, D. C. Schmadel, and R. J. Phaneuf, Opt. Express **16**, 19850 (2008).

[17]S. O'Brien and J. B. Pendry, J. Phys.: Condens. Matter **14**, 6383 (2002).

[18]K. Aydin, I. Bulu, K. Guven, M. Kafesaki, C. M. Soukoulis, and E. Ozbay, New J. Phys. **7**, 168 (2005).

[19]I. Gil, J. Garcia-Garcia, J. Bonache, F. Martin, M. Sorolla, and R. Marques, Electron. Lett. **40**, 1347 (2004).

[20]T. Driscoll, H.-T. Kim, B.-G. Chae, B.-J. Kim, Y.-W. Lee, N. M. Jokerst, S. Palit, D. R. Smith, M. Di Ventra, and D. N. Basov, Science **325**, 1518 (2009).

A.3 Paper III

- **C. Jeppesen**, S. Xiao, N.A. Mortensen, and A. Kristensen, *Extended verification of scaling behavior in split-ring resonators*, Opt. Commun., **284**, 799-801 (2011).

Contents lists available at ScienceDirect

Optics Communications

Extended verification of scaling behavior in split-ring resonators

Claus Jeppesen [a], Sanshui Xiao [b], Niels Asger Mortensen [b,*], Anders Kristensen [a]

[a] Department of Micro and Nanotechnology, Technical University of Denmark, DTU Nanotech, Building 345 East, DK-2800 Kongens Lyngby, Denmark
[b] Department of Photonics Engineering, Technical University of Denmark, DTU Fotonik, Building 345 West, DK-2800 Kongens Lyngby, Denmark

ARTICLE INFO

ABSTRACT

We present an expanded *LC*-model for nanoscale split-ring resonators (SRR), including the influence of dielectric host materials. The *LC*-model is experimentally verified by changing the geometry of the SRR unit cell as well as by optofluidic tuning, where the SRR samples are covered with index oil. The extended model can be used as a general guideline for metal SRR structures with arbitrary dielectric host materials.

© 2010 Elsevier B.V. All rights reserved.

1. Introduction

Metamaterials are artificially structured materials with exceptional optical properties inherited from the structure of the subwavelength, mesoscopic unit-cell. Designing negative-index materials with as well as negative permeability μ is one of the promising aspects of metamaterials. However, the validity of assigning effective material parameters depends largely on the given structure and frequency [1]. Since a negative electric response is common in metals at e.g. optical frequencies the search has primarily focused on designing structures with a negative magnetic response. Different types of split-ring resonator (SRR) geometries [2–4] are particularly central in this context and have been realized at Terahertz [2,5] to visible frequencies [4,6].

The analogy with inductor–capacitor (*LC*) circuits has motivated considerable efforts in establishing simple circuit models, allowing for an estimate of the resonance frequency $\omega_0 \simeq 1/\sqrt{LC}$ in terms of geometrical parameters of the split-ring resonator structure, see. e.g. Refs. [7–9] and references therein. The *LC*-model has proven to be a good approximation as long as the coupling response of the SRR array is small compared to the response of a single SRR, hence the period Λ has to be sufficiently large [10]. Tuning of the resonance has been accomplished by scaling of a single geometrical dimension [11,12], linear scaling of all SRR dimensions [6,13], and finally by altering the cladding [12,14].

2. Theory and modelling

In this letter we expand the *LC*-model of the SRRs to account for the surroundings. The model is thoroughly tested by changing the cladding material, thereby tuning the resonance frequency. The expanded model can be used for tuning purposes and as a general design guideline for SRR metal structures with arbitrary dielectric host materials. We have previously treated the conventional case of gold SRRs on a glass substrate with the cladding being air and experimentally verified an expression, $\omega \simeq (c/\ell)\sqrt{d/w}$, see Fig. 1, for the resonance behavior based on a *LC*-model [9].

Here, ℓ is the side length, d is the slit width, and w is the slit length. To account for changing cladding material an effective permittivity has to be included in the expression, see Eq. (1)

$$\omega = \frac{S}{\sqrt{\varepsilon_{\text{eff}}}}\frac{c}{\ell}\sqrt{\frac{d}{w}}, \quad \varepsilon_{\text{eff}} = f\epsilon_{\text{clad}} + (1-f)\epsilon_{\text{sub}} \qquad (1)$$

where S is a geometry dependent, dimensionless number, and c is the speed of light in vaccum. Here, f is the concentration factor which measures the fraction of electric field energy located inside the cladding medium with dielectric function ϵ_{clad}. Likewise, $1-f$ gives the fraction of electric field energy located inside the substrate medium with dielectric function ϵ_{sub}, thus implicitly assuming that the electric field is zero inside the metal. We interpret f as a geometrical correction to the plate-capacitor model, while S corrects the inductance from that of a simple single-turn loop with area $\ell \times \ell$. The concentration factor f is extracted from experiments if the electric field distribution is only weakly perturbed by changing ϵ_{clad}. This is done by covering the SRR structures with liquids of different dielectric constant, and probing the resonance frequency ω. The fluidic tuning leaves all other parameters invariant. Subsequently, S is obtained by

* Corresponding author. Tel.: +45 4 525 5724.
E-mail address: asger@mailaps.org (N.A. Mortensen).
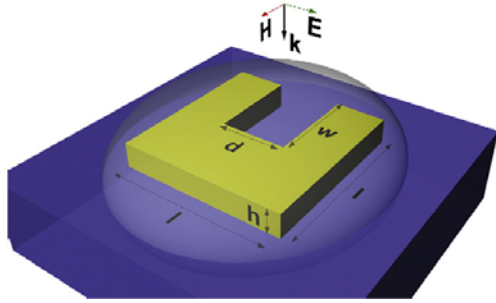
Fig. 1. Schematic drawing of the split-ring resonator design, indicating central geometrical parameters as well as the polarization configuration of the excitation, which is at normal incidence. The split-ring resonator is covered with index oil.
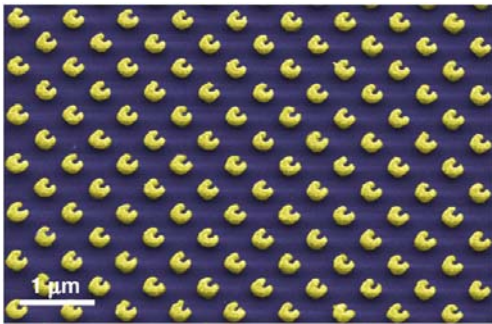
Table 1
Resonance wavelength λ and FWHM measured on 8 samples with periods Λ = 330–660 nm. For Λ = 660 nm it was impossible to determine an accurate FWHM due to the low signal amplitude.

Sample	Λ [nm]	λ [nm]	FWHM [nm]
1	330	1351	343
2	330	1405	305
3	440	1407	252
4	440	1409	253
5	550	1445	250
6	550	1354	239
7	660	1287	–
8	660	1467	–

inserting f and ω into Eq. (1). In this approach, we assume that the cladding dielectric function changes by $\Delta\epsilon$, whereby ϵ_{clad} can be written as $\epsilon_{\text{clad}} = \epsilon_{\text{air}} + \Delta\epsilon$.

Our hypothesis is that the geometrical factors f and S are constant for SRRs where the overall geometry remains unchanged. Small dimensional variations of d/w and l should therefore not have an impact on f and S (Eq. (1)). The hypothesis is tested by numerical calculations using CST Microwave Studio [15]. For constant $h = 30$ nm and $l = 200$ nm, $d/w = 0.8$–1.1 yields $f = 0.56$–0.57. Keeping d/w and h constant, $l = 190$–210 nm gives $f = 0.56$–0.57. Hence, small geometrical variations of d/w or l leads to ~2% variation in f, and even less variation for S. The small perturbations of the geometrical constants f and S support our hypothesis.

3. Fabrication

To experimentally assess the LC-model, 15 samples were prepared with 2 mm by 2 mm arrays of split-ring resonators, see Fig. 2. All SRRs had the same overall single-slit shape but the individual dimensions were altered in the range $d/w = 0.75$–1.15, $l = 150$–210 nm, and $h = 35$–95 nm, thereby enabling a vast parameter space. In the initial phase, 8 samples with $\Lambda = 330$–660 nm were considered to explore the coupling dependent broadening of the resonance. The transmission spectra were obtained using a 1 mm diameter laser spot, thus probing 10^6–10^7 SRRs and thereby ensuring a constant inhomogeneous broadening. The results are given in Table 1.

For $\Lambda = 660$ nm it was impossible to determine an accurate FWHM due to the low signal amplitude. Table 1 shows, that the broadening is nearly constant for $\Lambda = 440$–550 nm, indicating a vanishing coupling dependence of the resonance. By combining these results with the
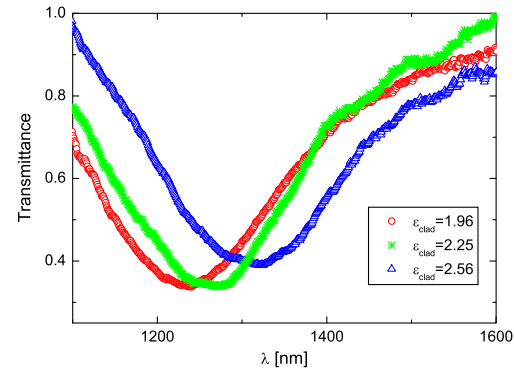

Fig. 3. Fluidic tuning of the SRRs by changing the dielectric constant of the cladding material ϵ_{clad} from 1.96 to 2.56. The spectra were obtained using a supercontinuum light source (SuperK SCB-Compact 100-PC) and an optical spectrum analyzer (Ando AQ-6315E). The spectra are normalized using a reference spectrum of the underlying fused silica substrate.

Fig. 2. Micrograph of a SRR array with pitch $\Lambda = 500$ nm. This sample has $\ell = 200$ nm, $w = 93$ nm, $d = 98$ nm, and $h = 95$ nm.
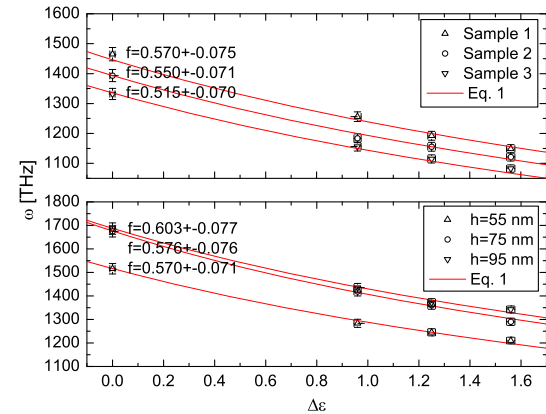

Fig. 4. The measured resonance frequency as a function of cladding tuning. (a) Three samples with constant $h = 35$ nm. Sample 1 has $(d,w,\ell) = (82,83,199)$, sample 2 has $(90,98,201)$, and sample 3 has $(92,109,207)$. The red line is Eq. (1) with $f = 0.55$ and $S = 1.18$, which is the average values from the experimental data. (b) Three samples with $h = 55$–95 nm, $\ell = 200$–205 nm, $w = 80$–93 nm, and $d = 91$–93 nm. The red lines are Eq. (1) with $f = 0.57$–0.60 and $S = 1.24$–1.27. The x-error bars are the uncertainty of the dielectric constant of the cladding material and substrate material. The y-error bars are the 10 nm spectral resolution of the Ando AQ-6315E Optical Spectrum Analyzer.

Sample	d[nm]	w[nm]	l[nm]	h[nm]	λ [nm]			
⊖	52	71	155	35	1131	1341	1348	1388
⊟	74	88	195	55	1243	1468	1513	1557
◇	82	83	199	35	1286	1502	1580	1638
▷	84	108	205	35	1420	1650	-	-
□	86	112	207	35	1470	1725	-	-
▽	90	98	201	35	1352	1591	1634	1685
◁	90	99	206	35	1354	1540	-	-
⌂	90	112	203	35	1461	1700	-	-
⊞	93	80	201	75	1117	1313	1379	1398
△	92	109	207	35	1414	1629	1687	1741
○	97	116	206	35	1469	1648	1730	-
⊠	98	93	190	95	1125	1328	1385	1460
Legend								
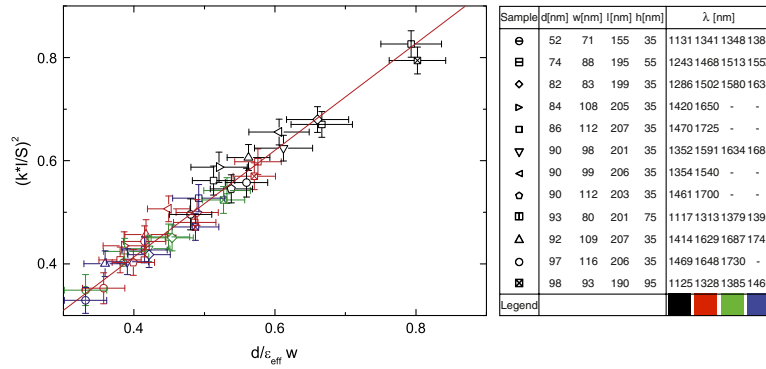
Fig. 5. Plot of $(k\ell/S)^2$ versus $d/\epsilon_{\mathrm{eff}}w$. The SRR dimensions and the resonance wavelengths λ are listed in the table. The solid line ($y = 1.03\ x$) fits the data. The x-error bars represent the standard deviation (SD) of ten individual measurements of w, and d added together with the uncertainty on ϵ_{eff}. The y-error bars are the 10 nm spectral resolution of the Ando AQ-6315E Optical Spectrum Analyzer added to the uncertainty on S, and the SD of ten measurements of the length ℓ.

trade-off between coupling and signal amplitude, $\Lambda = 500$ nm was chosen for the remaining work. The choice was further supported by polarization conversion measurements on samples with two perpendicular orientations of the SRRs showing a stagnating signal amplitude around $\Lambda = 450$–500 nm. The conclusion is therefore that for $\Lambda = 500$ nm coupling effects may safely be ignored and the LC-model of a single isolated resonator can be applied.

Fabrication wise, a 100–180 nm thick layer of EBL resist, ZEP520A (3.6%, Zeon Corp., Tokyo, Japan) is spin coated onto a 1 mm thick fused silica substrate. A 15 nm aluminium layer is thermally deposited on top of the zep layer to prevent charge accumulation during EBL. The proximity corrected EBL exposure is performed with a 100 kV JEOL JBX-9300FS EBL tool (200 μC/cm² dose, 2 nA current, and 6 nm spot size). The aluminium layer is then removed in MF-322 (Rohm and Haas, Coventry, UK) and the positive ZEP resist is developed in ZED-N50 (Zeon Corp.) developer. A brief O₂ plasma descum process is applied to remove the residual resist before 5 nm Ti/30–90 nm Au is deposited by electron beam deposition. The final lift-off is performed by using Remover 1165 (Rohm and Haas) in an ultrasound bath.

4. Results

Fig. 3 illustrates the resonance shift when changing $\epsilon_{\mathrm{clad}} = 1.96$–2.56 by covering a SRR sample with index oil. In Fig. 4(a) the experimental tuning data of three samples with a constant height $h = 35$ nm is compared to our LC-model through Eq. (1). Using an average value of the concentration factor $f = 0.55$ and $S = 1.18$ based on the experimental data, there is an excellent agreement between the measurements and the model. Supporting CST modelling yields $f = 0.57$. As demonstrated previously, the concentration factor f is independent of the geometrical parameters of Eq. (1). However, there is an expected dependence of f on the height h since for increasing h, the portion of the E-field situated in the cladding material should increase relative to the portion of the E-field in the substrate [8]. Fig. 4(b) illustrates resonance data for different heights $h = 55$–95 nm yielding $f = 0.57$–0.60 and $S = 1.24$–1.27. CST simulations yield $f = 0.58$–0.65, which as for the previous results is a small overestimate of the experimental results. Fig. 5 sums up the cladding tuning and geometrical scaling of the SRRs in a single $(k\ell/S)^2$ versus $\epsilon_{\mathrm{eff}}^{-1} \times (d/w)$ graph using the data in the adjacent table. A clear data collapse with a slope $\alpha = 1.03 \pm 0.007$ confirms the model within a 3% error. For the conventional substrate/cladding = glass/air scenario $S/\sqrt{\epsilon_{\mathrm{eff}}} \sim 1$. This leads to the simpler form $(k_0\ell)^2 = (d/w)$, which has been successfully tested in a previous work [9].

5. Conclusion

In conclusion, we have extended the LC-model such that it can be used for changing host materials provided that the field distribution is only slightly perturbed. The model has been thoroughly tested by combining geometrical scaling of the SRR unit cell and tuning the cladding material. The experimental findings have been supported by 3D numerical modelling. The extended LC-model has thus been verified as a design tool for SRRs in future integrated nanophotonic devices. We would like to promote the results of this paper as a first step towards a method for optical sensing using SRR structures. Future efforts should address ways to improve the resonance linewidth.

References

[1] C. Menzel, T. Paul, C. Rockstuhl, T. Pertsch, S. Tretyakov, F. Lederer, Phys. Rev. B 81 (2010) 035320.
[2] T.J. Yen, W.J. Padilla, N. Fang, D.C. Vier, D.R. Smith, J.B. Pendry, D.N. Basov, X. Zhang, Science 303 (2004) 1494.
[3] N. Katsarakis, G. Konstantinidis, A. Kostopoulos, R.S. Penciu, T.F. Gundogdu, M. Kafesaki, E.N. Economou, T. Koschny, C.M. Soukoulis, Opt. Lett. 30 (2005) 1348.
[4] C. Enkrich, M. Wegener, S. Linden, S. Burger, L. Zschiedrich, F. Schmidt, J.F. Zhou, T. Koschny, C.M. Soukoulis, Phys. Rev. Lett. 95 (2005) 203901.
[5] S. Linden, C. Enkrich, M. Wegener, J.F. Zhou, T. Koschny, C.M. Soukoulis, Science 306 (2004) 1351.
[6] M.W. Klein, C. Enkrich, M. Wegener, C.M. Soukoulis, S. Linden, Opt. Lett. 31 (2006) 1259.
[7] H.C. Guo, N. Liu, L.W. Fu, H. Schweizer, S. Kaiser, H. Giessen, Phys. Stat. Sol. (b) 244 (2007) 1256.
[8] T.D. Corrigan, P.W. Kolb, A.B. Sushkov, H.D. Drew, D.C. Schmadel, R.J. Phaneuf, Opt. Express 16 (2008) 19850.
[9] C. Jeppesen, N.A. Mortensen, A. Kristensen, Appl. Phys. Lett. 95 (2009) 1931084.
[10] B. Kante, A. de Lustrac, J.M. Lourtioz, Phys. Rev. B 80 (2009) 035108.
[11] K. Aydin, I. Bulu, K. Guven, M. Kafesaki, C.M. Soukoulis, E. Ozbay, New J. Phys. 7 (2005) 1367.
[12] S.-Y. Chiam, R. Singh, J. Gu, J. Han, W. Zhang, A.A. Bettiol, Appl. Phys. Lett. 94 (2009) 064102.
[13] S. O'Brien, J.B. Pendry, J. Phys. Condens. Matter 14 (2002) 6383.
[14] Y. Sun, X. Xia, H. Feng, H. Yang, C. Gu, L. Wang, Appl. Phys. Lett. 92 (2008) 221101.
[15] The gold dispersion is described by the Drude model with plasma frequency $\omega_p = 1.3673 \times 10^{16}$ s⁻¹, collision frequency $\omega_c = 1.0027 \times 10^{14}$ s⁻¹ and $\epsilon_0 = 9.0$ [16]. The substrate material is fused silica $\epsilon_{\mathrm{sub}} = 2.1$. We employed the frequency domain, a tetrahedral mesh with a 1×10^{16} accuracy, and adaptive mesh refinement. For a 100 THz range, 1000–10,000 samples were calculated giving a discretization of 10–100 THz⁻¹. All CST modelling geometries were given 20 nm radius rounded edges for better representation of the physical samples. On a standard laptop a calculation typically takes 4–8 h.
[16] V.M. Shalaev, W.S. Cai, U.K. Chettiar, H.K. Yuan, A.K. Sarychev, V.P. Drachev, A.V. Kildishev, Opt. Lett. 30 (2005) 3356.

A.4 Paper IV

- **C. Jeppesen**, N.A. Mortensen, and A. Kristensen, *The effect of Ti and ITO adhesion layers on gold split-ring resonators*, Appl. Phys. Lett., Accepted (2010).

The effect of Ti and ITO adhesion layers on gold split-ring resonators

Claus Jeppesen,[1] Niels Asger Mortensen,[2] and Anders Kristensen[1*]

Department of Micro and Nanotechnology,

Technical University of Denmark, DTU Nanotech,

Building 345 East, DK-2800 Kongens Lyngby, Denmark

Department of Photonics Engineering,

Technical University of Denmark, DTU Fotonik,

Building 345 West, DK-2800 Kongens Lyngby, Denmark

(Dated: December 3, 2010)

Abstract

Ultra-thin adhesion layers serve a well-documented fabrication purpose while its influence on the optical properties of gold nanostructures is often neglected. Gold split-ring resonators are fabricated with two commonly used adhesion layers: titanium and indium tin oxide. When compared to all-gold reference samples, a spectral shift of the ground mode resonance is observed. For the titanium sample the spectral shift is accompanied by a resonance broadening, which is less profound for indium tin oxide. The mutual correlation between the shift and the broadening is shown to be qualitatively consistent with perturbative considerations.

PACS numbers: 78.67.-n, 81.07.-b

---

[*] Corresponding author: anders@mailaps.org

1

Split-ring resonators (SRR) are key structures within the field of metamaterials that provide a negative magnetic response to light. SRRs' resonating behavior have also made them a potential candidate as refractive index sensors detecting thin polymer layers [1], Si nanospheres in solution [2], organic monolayers [3], and DNA [4]. Although the sensitivity of SRR based sensors is comparable to other optical sensors such as photonic crystals, see e.g. [5–7], the major drawback of the SRRs has been the very wide resonance peak, see e.g. [8]. Several effects contribute to the resonance broadening including internal damping and coupling between SRRs [9]. To compensate for the losses it has been suggested to embed the SRRs in materials with optical gain [10] and SRRs have been fabricated out of superconducting materials [11]. The fabrication of gold nanostructures typically benefits from adhesion promotors, though exceptions have been reported, see e.g. [12].

In this Letter, we investigate the influence of thin adhesion layers on the optical properties of gold (Au) nanoscale split-ring resonators. Compared with an all-gold reference sample, a vast spectral shift is observed when employing both titanium (Ti) and indium tin oxide (ITO) adhesion layers. While the resonance linewidth remains largely unchanged for the ITO/Au SRRs, the titanium layer significantly broadens the resonance. This indicates the superiority of ITO adhesion layers over Ti in metal nano-optics.

If a gold SRR on a glass substrate is perceived as a reference system, the commonly used adhesion layer can be seen as a perturbation of this system. The shift in frequency $\Delta\omega$ and the associated broadening $\Delta\Gamma$ can be estimated from perturbation theory as

$$\Delta\omega = -\frac{\omega_0}{2} \frac{\epsilon'_{\text{adh}} - \epsilon_{\text{silica}}}{\epsilon_{\text{silica}}} \times f \tag{1a}$$

$$\Delta\Gamma = -\frac{\omega_0}{2} \frac{\epsilon''_{\text{adh}}}{\epsilon_{\text{silica}}} \times f \tag{1b}$$

where ω_0 is the resonance frequency of the unperturbed system, ϵ'_{adh} and ϵ''_{adh} are the real and imaginary part of the permittivity of the adhesion material, ϵ_{silica} is the permittivity of the silica substrate, and f is the fraction of optical power in the volume occupied by the adhesion material. Obviously, $\Delta\omega$ and $\Delta\Gamma$ from Eq. (1) are not fully independent quantities

$$\Delta\Gamma = \chi\Delta\omega, \ \chi = \frac{\epsilon''_{\text{adh}}}{\epsilon'_{\text{adh}} - \epsilon_{\text{silica}}} \tag{2}$$

Using a typical Ti-induced wavelength shift of $\Delta\lambda$=100 nm [13] and a typical value of $\chi\sim1$ (as shown later), Eq. (2) suggests a comparable narrowing of the linewidth. On the other hand, ITO has a better optical quality and consequently $\chi \ll 1$ is expected.

2

In the fabrication, a 150 nm thick layer of EBL resist, ZEP520A (Zeon Corp., Tokyo, Japan) is spincoated onto a 1 mm thick fused silica substrate. A 15 nm aluminium layer is thermally deposited on top of the ZEP layer to prevent charge accumulation during EBL. A 1.2×1.2 mm^2 area is written with a 100 kV JEOL JBX-9300FS EBL tool (200 μC/cm^2 dose, 2 nA current, 6 nm spotsize). The aluminium layer is then removed in MF-322 (Rohm and Haas, Coventry, UK) and the positive ZEP resist is developed in ZED-N50 (Zeon Corp.) developer. A brief O$_2$ plasma descum process is applied to remove residual resist before deposition of a 2-5 nm adhesion layer, Ti or ITO, and 50 nm Au. The final lift-off is performed by using Remover 1165 (Rohm and Haas). A SEM micrograph of a fabricated sample is shown in Fig. 1.
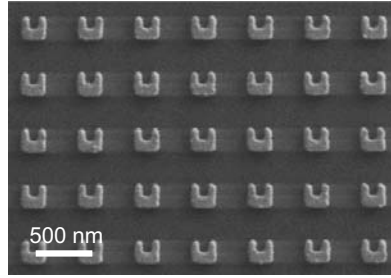

FIG. 1: SEM micrograph of Au SRRs on a fused silica substrate. The structures have a sidelength ℓ=200 nm and a height h=50 nm, while the period is Λ=500 nm.

The results of transmission measurements for the fundamental LC-resonance at normal incidence with a 200-300 μm spot size are given in Fig. 2.

The observed blue-shift and increased resonance magnitude, by omitting the Ti layer (Fig. 2) is in accordance with and extends the observation of Lahiri *et al.* [13].

Here, a signal increase of about 20% is observed. Even more noticeable is the narrower linewidth of 133 nm (FWHM) as opposed to 199 nm for Ti/Au, which is a 33% reduction. Applying Eq. (2) with -ϵ'_{Ti}=4.0, ϵ''_{Ti}=-2.9 [14], and ϵ_{silica}=2.1 yields $\chi_{\text{theory}} \simeq 0.48$ while in the experiments $\Delta\omega$=79 THz and $\Delta\Gamma$=87 THz would suggest a corresponding number χ_{measured}=1.1. One might argue that ϵ''_{Ti}=-2.9 denotes the bulk value and that the loss would be even higher for a 5 nm layer [15]. If we speculate that the loss is doubled we get
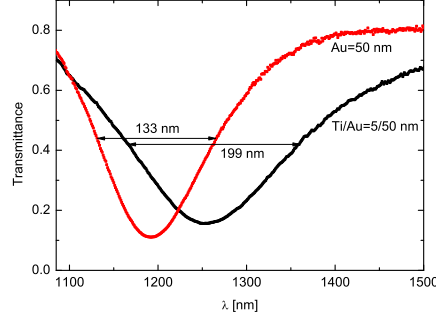
3

FIG. 2: Transmission spectra for samples with and without a 5 nm Ti adhesion layer measured at normal incidence. The spot size is 80 μm. The spectra were obtained at normal incidence using a supercontinuum light source (SuperK SCB-Compact 100-PC) and an optical spectrum analyzer (Ando AQ-6315E).

χ_{theory}=0.96, which is very close to the measured value.

For ITO, Fig. 3 shows an even larger spectral shift ($\Delta\omega$=169 THz). However, most remarkably the resonance remains unbroadened within our measurement accuracy $\Delta\Gamma <$ $2-3$ THz. This indicates the high optical quality of ITO with ϵ_{ITO}" as low as 0.02 according to Eq. (2). This value depends largely on the chemical stoichiometry, the substrate and the processing of ITO [16–18].

The potential of split-ring resonators and related plasmonic resonators are often emphasized in the context of refractive-index sensors [1–4]. Here, we briefly assess the sensitivity of our fabricated structure by fluidic tuning experiments. Figure 4 summarizes the sensitivity measurements for the all-gold sample in Fig. 2 carried out by changing the cladding material from air (n=1) to different index oils ranging from n=1.4 to 1.6.

By combining the sensitivity $\Delta\lambda/\Delta n$=667 nm/RIU $\pm$9 nm/RIU with the 133 nm linewidth, a FOM of 5 is obtained. This is comparable to other metamaterial optical devices [19, 20] at near-infrared frequencies. Full-wave numerical 3D simulations (CST Microwave Studio) predict a sensitivity of 760 nm/RIU, which is in good agreement with the experimental results. The vast improvement of the linewidth is caused by the reduction of the Ohmic resistance within the individual SRR. For further improvement, the SRR-SRR
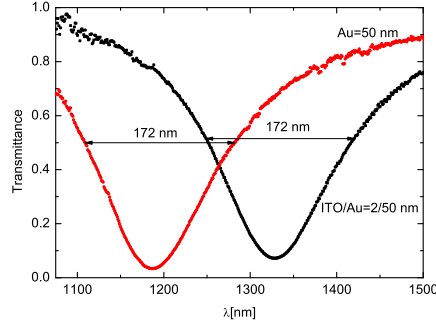
4

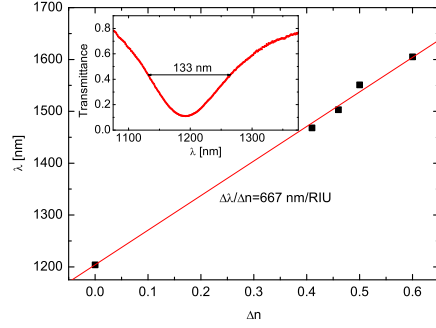FIG. 3: Transmission spectra for samples with and without a 2 nm ITO adhesion layer at normal incidence.

FIG. 4: The sensitivity of the sample for a dynamic range of 0.6 RIU. The inset shows the measured linewidth of the fundamental LC-resonance.

coupling has to be addressed and if possible the inhomogeneous broadening, which is related to variations in geometry, hence fabrication.

In conclusion, we have fabricated Au nanoscale split-ring resonators, contrasting Ti and ITO adhesion promoters. Titanium adhesion layers inherently cause frequency shifts and line broadening, as we clearly observe experimentally. On the other hand, ITO induces a spectral shift but without compromising the resonance quality factor as compared to the all-gold reference sample. However, the large variation in optical parameters of ITO prevents a

5

quantitative model for the SRR samples. This precludes a comparison of SRR samples unless the ITO layer is fully characterized. Characterization is particular difficult for ultrathin adhesion layers. Our results are shown to be consistent with perturbative considerations and suggests that qualitative modelling of thin-film metallic structures should account for even ultra-thin adhesion layers.

[1] B. Lahiri, A. Z. Khokhar, R. M. De La Rue, S. G. McMeekin, and N. P. Johnson, Opt. Express **17**, 1107 (2009).

[2] T. Driscoll, G. O. Andreev, D. N. Basov, S. Palit, S. Y. Cho, N. M. Jokerst, and D. R. Smith, Appl. Phys. Lett. **91**, 062511 (2007).

[3] E. Cubukcu, S. Zhang, Y.-S. Park, G. Bartal, and X. Zhang, Appl. Phys. Lett. **95**, 043113 (2009).

[4] A. W. Clark, A. Glidle, D. R. S. Cumming, and J. M. Cooper, J. Am. Chem. Soc. **131**, 7615 (2009).

[5] D. Erickson, T. Rockwood, T. Emery, A. Scherer, and D. Psaltis, Opt. Lett. **31**, 59 (2006).

[6] N. A. Mortensen, S. Xiao, and J. Pedersen, Microfluid Nanofluid **4**, 117 (2008).

[7] D. Dorfner, T. Zabel, T. Hurlimann, N. Hauke, L. Frandsen, U. Rant, G. Abstreiter, and J. Finley, Biosens Bioelectron **24**, 3688 (2009).

[8] C. Jeppesen, N. A. Mortensen, and A. Kristensen, Appl. Phys. Lett. **95**, 1931084 (2009).

[9] M. Husnik, M. W. Klein, N. Feth, M. Konig, J. Niegemann, K. Busch, S. Linden, and M. Wegener, Nat. Photonics **2**, 614 (2008).

[10] Y. Sivan, S. Xiao, U. K. Chettiar, A. V. Kildishev, and V. M. Shalaev, Opt. Express **17**, 24060 (2009).

[11] V. A. Fedotov, A. Tsiatmas, J. H. Shi, R. Buckingham, P. de Groot, Y. Chen, S. Wang, and N. I. Zheludev, Opt. Express **18**, 9015 (2010).

[12] J. Henzie, M. H. Lee, and T. W. Odom, Nat. Nanotechnol. **2**, 549 (2007).

6

[13] B. Lahiri, R. Dylewicz, R. M. De la Rue, and N. P. Johnson, Opt. Express **18**, 11202 (2010).

[14] P. B. Johnson and R. W. Christy, Phys. Rev. B **9**, 5056 (1974).

[15] S. Linden, C. Enkrich, M. Wegener, J. F. Zhou, T. Koschny, and C. M. Soukoulis, Science **306**, 1351 (2004).

[16] M. Losurdo, M. Giangregorio, P. Capezzuto, G. Bruno, R. De Rosa, F. Roca, C. Summonte, J. Pla, and R. Rizzoli, J. Vac. Sci. Technol. A **20**, 37 (2002).

[17] R. Synowicki, Thin solid films **313**, 394 (1998).

[18] F. Lai, L. Lin, R. Gai, Y. Lin, and Z. Huang, Thin Solid Films **515**, 7387 (2007).

[19] N. Liu, T. Weiss, M. Mesch, L. Langguth, U. Eigenthaler, M. Hirscher, C. Soennichsen, and H. Giessen, Nano Lett. **10**, 1103 (2010).

[20] F. Hao, P. Nordlander, Y. Sonnefraud, P. Van Dorpe, and S. A. Maier, ACS Nano **3**, 643 (2009).

7

A.5 Paper V

- **C. Jeppesen**, N.A. Mortensen, and A. Kristensen, *Metamaterial localized resonance sensors: prospects and limitations*, Opt. Express, **18**(24), 25075-25080 (2010).

Metamaterial localized resonance sensors: prospects and limitations

C. Jeppesen,[1] **S. Xiao,**[2] **N. A. Mortensen,**[2] **and A. Kristensen**[1,*]

[1]*Department of Micro and Nanotechnology, Technical University of Denmark, DTU Nanotech, Building 345 East, DK-2800 Kongens Lyngby, Denmark*
[2]*Department of Photonics Engineering, Technical University of Denmark, DTU Fotonik, Building 345 West, DK-2800 Kongens Lyngby, Denmark*

[*]*anders@mailaps.org*

Abstract: The prospects and limitations of metamaterial localized resonance sensors are investigated theoretically and experimentally. Gold split-ring resonators are employed as the model system where the light induced *LC*-resonance yields a figure-of-merit, sensitivity divided by linewidth, up to 54 depending on the split-ring resonator design and engineering of the light-plasmon coupling. This highest measured value is comparable to quasi-static predictions, suggesting incremental improvements beyond this point. Further optimization attempts show the effect of inhomogeneous broadening giving some indication that the limits have been reached for this particular design and material choice.

© 2010 Optical Society of America

OCIS codes: (160.3918) Metamaterials,(220.4241) Nanostructure fabrication.

References and links

1. N. Fang, H. Lee, C. Sun, and X. Zhang, "Sub-diffraction-limited optical imaging with a silver superlens," Science **308**(5721), 534–537 (2005).
2. C. Jeppesen, R. B. Nielsen, A. Boltasseva, S. Xiao, N. A. Mortensen, and A. Kristensen, "Thin film Ag superlens towards lab-on-a-chip integration," Opt. Express **17**(25), 22543–22552 (2009).
3. I. I. Smolyaninov, Y.-J. Hung, and C. C. Davis, "Magnifying superlens in the visible frequency range," Science **315**(5819), 1699–1701 (2007).
4. J. Valentine, J. Li, T. Zentgraf, G. Bartal, and X. Zhang, "An optical cloak made of dielectrics," Nature Mater. **8**(7), 568–571 (2009).
5. B. Lahiri, A. Z. Khokhar, R. M. De La Rue, S. G. McMeekin, and N. P. Johnson, "Asymmetric split ring resonators for optical sensing of organic materials," Opt. Express **17**(2), 1107–1115 (2009).
6. T. Driscoll, G. O. Andreev, D. N. Basov, S. Palit, S. Y. Cho, N. M. Jokerst, and D. R. Smith, "Tuned permeability in terahertz split-ring resonators for devices and sensors," Appl. Phys. Lett. **91**(6), 062511 (2007).
7. E. Cubukcu, S. Zhang, Y.-S. Park, G. Bartal, and X. Zhang, "Split ring resonator sensors for infrared detection of single molecular monolayers," Appl. Phys. Lett. **95**(4), 043113 (2009).
8. A. W. Clark, A. Glidle, D. R. S. Cumming, and J. M. Cooper, "Plasmonic split-ring resonators as dichroic nanophotonic DNA biosensors," J. Am. Chem. Soc. **131**(48), 7615–17619 (2009).
9. N. A. Mortensen, S. Xiao, and J. Pedersen, "Liquid-infiltrated photonic crystals: enhanced light-matter interactions for lab-on-a-chip applications," Microfluid. Nanofluid. **4**(1-2), 117–127 (2008).
10. D. Dorfner, T. Zabel, T. Hurlimann, N. Hauke, L. Frandsen, U. Rant, G. Abstreiter, and J. Finley, "Photonic crystal nanostructures for optical biosensing applications," Biosens. Bioelectron. **24**(12), 3688–3692 (2009).
11. C. Jeppesen, N. A. Mortensen, and A. Kristensen, "Capacitance tuning of nanoscale split-ring resonators," Appl. Phys. Lett. **95**, 193108 (2009).
12. J. Zhang, S. Xiao, C. Jeppesen, A. Kristensen, and N. A. Mortensen, "Electromagnetically induced transparency in metamaterials at near-infrared frequency," Opt. Express **18**(16), 17187–17192 (2010).
13. Y. Sivan, S. Xiao, U. K. Chettiar, A. V. Kildishev, and V. M. Shalaev, "Frequency-domain simulations of a negative-index material with embedded gain," Opt. Express **17**(26), 24060–24074 (2009).

14. V. A. Fedotov, A. Tsiatmas, J. H. Shi, R. Buckingham, P. de Groot, Y. Chen, S. Wang, and N. I. Zheludev, "Temperature control of Fano resonances and transmission in superconducting metamaterials," Opt. Express **18**(9), 9015–9019 (2010).
15. L. J. Sherry, R. Jin, C. A. Mirkin, G. C. Schatz, and R. P. Van Duyne, "Localized surface plasmon resonance spectroscopy of single silver triangular nanoprisms," Nano Lett. **6**(9), 2060–2065 (2006).
16. F. Wang and Y. R. Shen, "General properties of local plasmons in metal nanostructures," Phys. Rev. Lett. **97**(20), 206806 (2006).
17. M. Svedendahl, S. Chen, A. Dmitriev, and M. Kall, "Refractometric sensing using propagating versus localized surface plasmons: a direct comparison," Nano Lett. **9**(12), 4428–4433 (2009).
18. P. B. Johnson and R. W. Christy, "Optical constants of noble metals," Phys. Rev. B **6**(12), 4370–4379 (1972).
19. M. A. Ordal, L. L. Long, R. J. Bell, S. E. Bell, R. R. Bell, R. W. Alexander, and C. A. Ward, "Optical properties of the metals Al, Co, Cu, Au, Fe, Pb, Ni, Pd, Pt, Ag, Ti, and W in the infrared and far infrared," Appl. Opt. **22**(7), 1099–1119 (1983).
20. M. Stockman, S. Faleev, and D. Bergman, "Localization versus delocalization of surface plasmons in nanosystems: can one state have both characteristics?" Phys. Rev. Lett. **87**(16), 167401 (2001).
21. S. Zhang, D. A. Genov, Y. Wang, M. Liu, and X. Zhang, "Plasmon-induced transparency in metamaterials," Phys. Rev. Lett. **101**(4), 047401 (2008).
22. H. Liu, D. A. Genov, D. M. Wu, Y. M. Liu, Z. W. Liu, C. Sun, S. N. Zhu and X. Zhang, "Magnetic plasmon hybridization and optical activity at optical frequencies in metallic nanostructures," Phys. Rev. B **76**(7), 073101 (2007).
23. J. Henzie, M. H. Lee, and T. W. Odom, "Multiscale patterning of plasmonic metamaterials," Nat. Nanotechnol. **2**(9), 549–554 (2007).
24. X. Yu, L. Shi, D. Han, J. Zi, and P. V. Braun, "High quality factor metallodielectric hybrid plasmonic-photonic crystals," Adv. Funct. Mater. **20**(12), 1910–1916 (2010).
25. A. V. Kabashin, P. Evans, S. Pastkovsky, W. Hendren, G. A. Wurtz, R. Atkinson, R. Pollard, V. A. Podolskiy, and A. V. Zayats, "Plasmonic nanorod metamaterials for biosensing," Nature Mater. **8**(11), 867–871 (2009).
26. X. Fan, I. M. White, S. I. Shopoua, H. Zhu, J. D. Suter, and Y. Sun, "Sensitive optical biosensors for unlabeled targets: a review," Anal. Chim. Acta **620**(1-2), 8–26 (2008).

1. Introduction

Metamaterials are artificially structured materials that obtain their properties from their mesoscopic unit cell structure rather than from the constituent materials. The focus of metamaterials has primarily been on their unique optical properties such as a negative refractive index, that enables the fabrication of exotic devices e.g. near-field superlenses [1, 2], hyperlenses [3], and invisibility cloaks [4]. However, lately there has also been considerable interest in using metamaterials as refractive index sensors. Metamaterials consisting of split-ring resonators (SRRs) are among the potential sensor candidates. SRRs have already been employed to detect thin polymer layers [5], Si nanospheres in solution [6], organic monolayers [7] and DNA [8]. SRR sensors have a competitive sensitivity to e.g. photonic crystal based sensors [9, 10] but with the wide resonance peak, see e.g. [11], being a major drawback. Several suggestions have been made to improve this including utilization of EIT-like concepts [12], embedding the SRRs in optical gain materials [13], and fabricating SRRs out of superconducting materials [14].

In this paper, we investigate the limits of metamaterial based sensors and derive an analytical expression for the figure-of-merit [15]

$$\text{FOM} = \frac{|\Delta\lambda/\Delta n|}{\delta\lambda} = \frac{Q}{\lambda}\left|\frac{\Delta\lambda}{\Delta n}\right|, \tag{1}$$

which favors a large sensitivity $\Delta\lambda/\Delta n$ and a narrow resonance linewidth $\delta\lambda = \lambda/Q$, which is central for the quantification of minute refractive-index changes. The quality factor Q has contributions from coupling, radiation loss, and inhomogeneous broadening, i.e. $Q = 1/(Q_0^{-1} + Q_{\text{coup}}^{-1} + Q_{\text{rad}}^{-1} + Q_{\text{inhom}}^{-1})$. In addition, there is an intrinsic Q_0 related to the ohmic damping of the plasmons. Surprisingly, in the quasi-static limit Q_0 has a universal nature [16]. The FOM inherits this universality, carrying no information on the detailed geometry of the plasmonic resonator. For common plasmonic metals (such as Au, Ag, and Al) this allows us to estimate
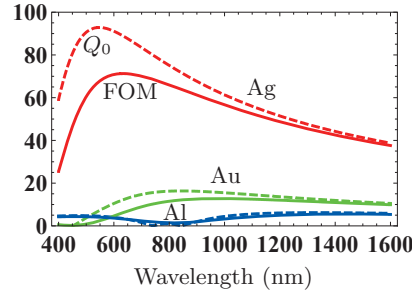
Fig. 1. The figure-of-merit (solid lines) in the quasi-static limit for three common plasmonic metals (Au, Ag, and Al). The dashed lines show corresponding results for the quality-factor.

typical FOMs in the range from 5 to 80, depending on the particular resonance frequency and the material of choice. The derived expression is tested by a SRR based model system where the coupling of bright and dark plasmonic elements is exploited to narrow the linewidth of the fundamental *LC*-resonance for all-gold SRRs.

2. Theory

Wang and Shen [16] used quasi-static arguments (assuming that $k\Lambda \ll 1$, with Λ being a characteristic length scale of the unit cell) to show that for metal structures surrounded by air, plasmonic localized resonances would have a universal quality factor

$$Q_0 = \frac{\omega \frac{\partial \varepsilon_m'}{\partial \omega}}{2\varepsilon_m''}, \quad k\Lambda \ll 1, \tag{2}$$

where $\varepsilon_m = \varepsilon_m' + i\varepsilon_m''$ is the complex permittivity of the metal. This result implies that any efforts of improving the sharpness of the plasmon resonance will be unfruitful, since the Q is only determined by the choice of metal and resonance frequency. Following the same lines we may derive a universal value of the FOM in the quasi-static limit. In particular, it can be shown that the sensitivity becomes $\partial\lambda/\partial n = (-\varepsilon_m'/\varepsilon_m'')\lambda/Q_0$ so that Eq. (1) becomes

$$\text{FOM} = \frac{|\varepsilon_m'|}{\varepsilon_m''}, \quad k\Lambda \ll 1. \tag{3}$$

A similar result was reported recently by Svedendahl *et al.* [17]. Interestingly, this intrinsic FOM is highly dependent on the plasmon damping while at the same time fully independent of the underlying geometrical details of the resonant plasmonic structure. Improving the geometrical properties will thus mainly serve to minimize radiation and coupling degradation of the intrinsic FOM. For larger resonator structures, the quasi-static assumption is not fulfilled, but as emphasized in Ref. [16], the predictions may still serve as important guidelines. Fig. 1 illustrates Eq. (2) and Eq. (3) for three often used metals in metamaterials with data taken from [18,19]. As seen, there is a vast difference in FOM between the chosen metals with silver being the best and aluminum being the worst. Most importantly, we emphasize the characteristic scale of the FOM, indicating that for localized plasmonic resonances in typical metal nanostructures the FOM is unlikely to exceed the range 10 to 10^2. For the majority of experimental studies, gold is the preferred material for nanostructures because it is relatively stable over time whereas silver rapidly oxidizes in an atmospheric environment.

3. Design and fabrication

To narrow the linewidth of the fundamental *LC*-resonance, we employ the coupling of bright and dark plasmonic elements. Bright and dark elements were first introduced by Stockman *et al.* [20]. The bright elements are easily excited by free-space radiation and the radiation dissipation limits their quality factor. When excited, the bright element can excite neighboring dark elements via near-field coupling. The absent direct radiation coupling results in a high quality factor for the dark elements, thus mainly being limited by the loss of the metal [21]. For a SRR, a bright element requires the arms to be aligned perpendicular to the radiation polarization whereas rotating the SRR by $\pm\pi/2$ leads to a dark element. For SRR based devices some optical activity occurs [22] but most of the energy stored in the dark element is re-radiated through the bright element. Here, the effect of the bright and dark elements is investigated by defining a unit cell of 2×2 SRRs and then changing the number of bright elements from four to one.

   In fabrication, a 180 nm thick layer of EBL resist, ZEP520A (Zeon Corp., Tokyo, Japan) is spincoated onto a 1 mm thick fused silica substrate. A 15 nm aluminium layer is thermally deposited on top of the ZEP layer to prevent charge accumulation during EBL. A 1.2×1.2 mm^2 area is written with a 100 kV JEOL JBX-9300FS EBL tool (200 μC/cm^2 dose, 2 nA current, 6 nm spotsize). The aluminium layer is then removed in MF-322 (Rohm and Haas, Coventry, UK) and the positive ZEP resist is developed in ZED-N50 (Zeon Corp.) developer. A brief O$_2$ plasma descum process is applied to remove residual resist before 50 nm Au is deposited by electron beam deposition. The final lift-off is performed by using Remover 1165 (Rohm and Haas). The fabricated samples are given in Fig. 2.
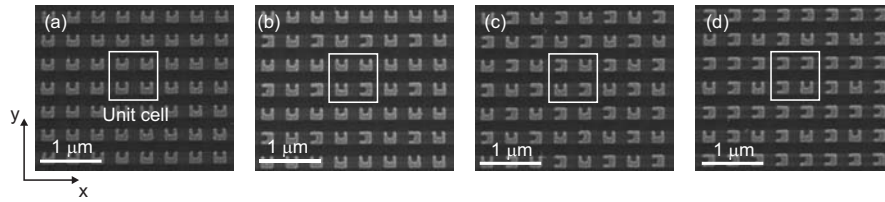

Fig. 2. SEM micrograph of the four unit cell configurations. The incident light is polarized along the *x*-direction. The samples have a sidelength ℓ=200 nm, height *h*=90 and a period Λ=400 nm. (a) 4 bright SRRs per unit cell. (b) 3 bright + 1 dark SRRs per unit cell. (c) 2 bright + 2 dark SRRs per unit cell. (d) 1 bright + 3 dark SRRs per unit cell.

4. Optical characterization

The transmission spectra are recorded in a free space setup using a supercontinuum light source (500-1750 nm, SuperK SCB-Compact 100-PC) and an optical spectrum analyzer (400-1750 nm, Ando AQ-6315E). The output beam is collimated and broadened to a 200 μm spot via a parabolic mirror. Then the light is linearly polarized by a Glan-Thompson polarizer before it reaches the sample. After traversing the sample, the beam is focused by another parabolic mirror and collected with an output fiber with a 10 μm core diameter leading to the spectrum analyzer. The transmission measurements are summarized in Fig. 3.

   By combining bright and dark elements, the linewidth is reduced from 220 nm in Fig. 3(a) to 29 nm in Fig. 3(d), which is a 87% reduction. At the same time the resonance depth exhibits a 40% (0.88 to 0.53) signal decrease. The fact that the relative narrowing is larger than the relative signal modulation, demonstrates the superiority of the latter design. Hence, the energy
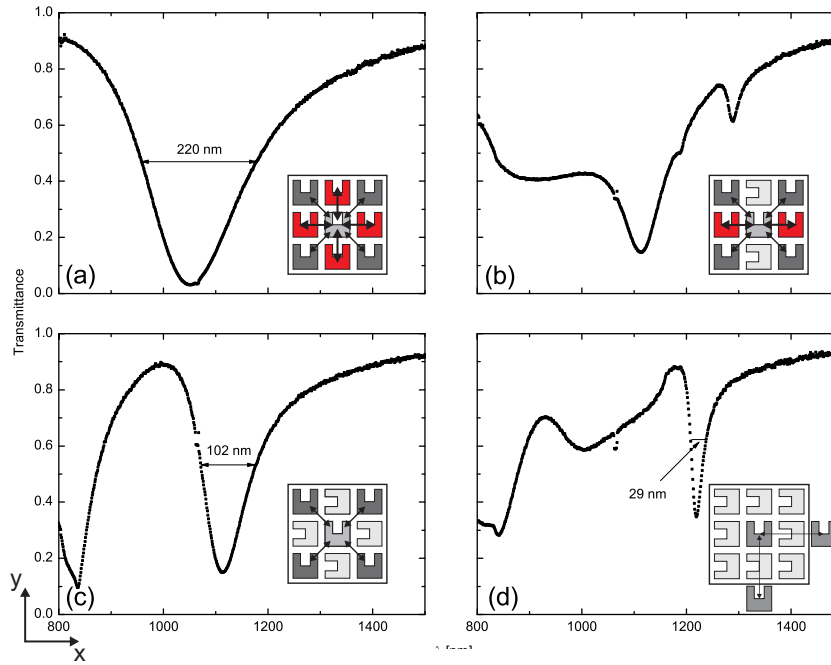
Fig. 3. Transmission measurements of the four unit cell configurations. The incident light is polarized along the *x*-direction. The insets show the nearest-neighbor interactions of the bright elements with the arrow width denoting the SRR-SRR coupling strength. (a) 4 bright SRRs per unit cell. (b) 3 bright + 1 dark SRRs per unit cell. (c) 2 bright + 2 dark SRRs per unit cell. (d) 1 bright + 3 dark SRRs per unit cell. The small signal disturbance at 1064 nm is an artifact from the pumping laser of the supercontinuum light source.

dissipation from SRR-SRR coupling is significantly less than the energy dissipation steming from the coupling to the radiation field.

The insets in Fig. 3 illustrate the nearest-neighbor coupling of the bright element. Due to the coupling, the measured signal from one SRR within the array, $A_{\mathrm{SRR_{meas}}}$, is a sum of several contributions

$$A_{\mathrm{SRR_{meas}}} = \sum A_{\mathrm{SRR}} + c_1 \times A_{\mathrm{nn}} + c_2 \times A_{\mathrm{nnn}} \cdots, \tag{4}$$

where c_1 and c_2 are configuration dependent positive integers and the subscripts nn and nnn denote nearest-neighbor and next-nearest-neighbor, respectively. The strongest contribution comes from the SRR itself (A_{SRR}) and for Fig. 3(a), (c), and (d) the nearest-neighbor term dominates. However, for Fig. 3(b) there are only 2 nearest-neighbors and 4 next-nearest-neighbors so that the dominance is less pronounced, resulting in a double dip. Even contributions from SRRs further away can be seen, which illustrates the vast dominance of the nearest-neighbor terms in Fig. 3(a), (c), and (d) where no other contributions to the fundamental *LC*-resonance are clearly observable. Note that the resonance at Λ=850 nm in Fig. 3(c) and (d) is a higher order mode and therefore not considered here. The overall narrowing can be seen as a step towards the intrinsic response of a single isolated SRR.

Fig. 3(d) illustrates the potential of SRR based sensors. The transmission spectrum for a

slightly more optimized structure in terms of the individual SRR geometry as well as the period Λ is given in Fig. 4. The sensitivity was measured by fluidic tuning of the cladding material. A

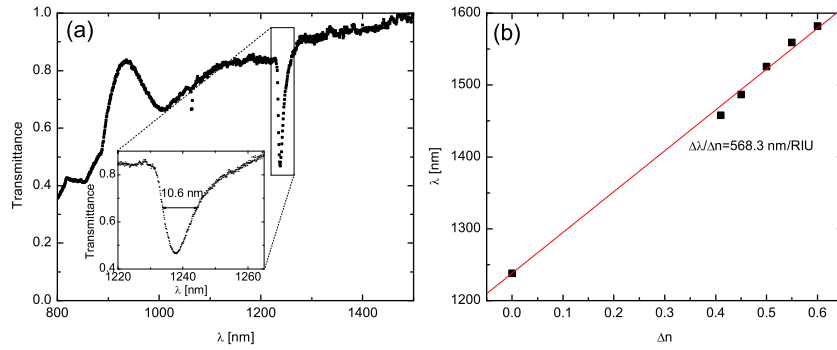Fig. 4. Transmission measurements of optimized "1 bright + 3 dark" structure. The SRRs have ℓ=200 nm, h=90 nm, Λ=425 nm. (a) Standard transmission measurement with air as cladding (b) Sensitivity curve based on transmission measurements for a dynamic range of 0.6 RIU.

sensitivity of 568.3 nm/RIU±6.9 nm/RIU and a linewidth of 10.6 nm, translates into a FOM of 54. This is one of the largest FOM's reported at visible or infrared frequencies [23,24]. Whereas the sensitivity is typical for this type of structure, the linewidth is extraordinary compared to typical values for similar designs [11].

Numerical simulations (CST Microwave Studio) have indicated that by increasing the height h the resonance could be additionally narrowed without affecting the sensitivity. However, h=100 nm did not further improve the linewidth. To the contrary the linewidth was widening to ∼12-13 nm. The increase is attributed to a poorer lift-off process, hence larger inhomogeneous broadening. This indicates that the limits of optimization has been reached for this particular SRR design and material choice.

5. Discussion and conclusion

Equation (3) shows that the fundamental limitation of localized plasmon based sensors scales with the material loss. Metals are commonly used in metamaterials at the expense of a high loss compared to semiconductors or dielectrics. Despite recent advances for guided plasmon modes in nanorod arrays [25], metallic metamaterials are unable to obtain the same figure-of-merits as seen in LSPR or interferometry based devices [26]. Hence, with present knowledge, metamaterial-based resonant structures do not appear as obvious candidates for a competitive refractometric sensing platform.

In conclusion, we have demonstrated the limitations of metamaterial localized resonance sensors theoretically and experimentally. Gold split-ring resonators have been employed as the model system yielding a figure-of-merit of up to 54 depending on the split-ring resonator design and the light-plasmon coupling. The measured values are comparable to quasi-static predictions, suggesting incremental improvements beyond this point.

Appendix B

Complete list of publications

B.1 Journal articles

- **C. Jeppesen**, N.A. Mortensen, and A. Kristensen, *The effect of Ti and ITO adhesion layers on gold split-ring resonators*, Appl. Phys. Lett., Accepted (2010).

- **C. Jeppesen**, S. Xiao, N.A. Mortensen, and A. Kristensen, *Extended verification of scaling behavior in split-ring resonators*, Opt. Commun., **284**, 799-801 (2011).

- **C. Jeppesen**, S. Xiao, N.A. Mortensen, and A. Kristensen, *Metamaterial localized resonance sensors: prospects and limitations*, Opt. Express, **18**(24), 25075-25080 (2010).

- S. Xiao, J. Zhang, L. Peng, **C. Jeppesen**, R. Malureanu, A. Kristensen, and N.A. Mortensen, *Nearly-zero transmission through periodically modulated ultrathin metal films*, Appl. Phys. Lett., **97**(7), 071116 (2010).

- J. Zhang, S. Xiao, **C. Jeppesen**, A. Kristensen, and N. A. Mortensen, *Electromagnetically induced transparency in metamaterials at near-infrared frequency*, Opt. Express, **18**(16), 17187-17892 (2010).

- **C. Jeppesen**, N.A. Mortensen, and A. Kristensen, *Capacitance tuning of nanoscale split-ring resonators*, Appl. Phys. Lett., **95**(19), 193108 (2009). Selected for the Virtual Journal of Nanoscale Science & Technology, Nov. 16, 2009.

- **C. Jeppesen**, R. B. Nielsen, A. Boltasseva, S. Xiao, N. A. Mortensen, and A. Kristensen, *Thin film Ag superlens towards lab-on-a-chip integration*, Opt. Express, **17**(25), 22543-22552 (2009). Selected for the Virtual Journal for Biomedical Optics, Volume 5, Issue 1, Jan. 4, 2010.

- **C. Jeppesen**, K. Molhave, and A. Kristensen, *Competition between the thermal gradient and the bimorph effect in locally heated MEMS actuators*, Journal of Micromechanics and Microengineering, **19**(1), 015008 (2009).

- N. Kehagias, V. Reboud, G. Chansin, M. Zelsmann, **C. Jeppesen**, C. Schuster, M. Kubenz, M Kubenz, F. Reuther, G. Gruetzner, and C. M. Sotomayor Torres, *Reverse- contact UV nanoimprint lithography for multilayered structure fabrication*, Nanotechnology, **18**(7), 175303 (2007).

- N. Kehagias, V. Reboud, G. Chansin, M. Zelsmann, **C. Jeppesen**, F. Reuther, C. Schuster, M. Kubenz, G. Gruetzner, and C. M. Sotomayor Torres, *Submicron three-dimensional structures fabricated by reverse contact UV nanoimprint lithography*, Journal of Vacuum Science and Technology B, **24**(6), 3002-3005 (2006).

- B. Bilenberg, S. Jacobsen, C. Pastore, T. Nielsen, S. R. Enghoff, **C. Jeppesen**, A. V. Larsen, and A. Kristensen, *Technology for Fabrication of Nanostructures by Standard Cleanroom Processing and Nanoimprint Lithography*, Japanese Journal of Applied Physics, **44**(7B), 5606-5608 (2005).

- B. Bilenberg, M. Hansen, D. Johansen, V. Ozkapici, **C. Jeppesen**, P. Szabo, I. M. Obieta, O. Arroyo, J. O. Tegenfeldt, and A. Kristensen, *Topas Based Lab-on-a-chip Microsystems Fabricated by Thermal Nanoimprint Lithography*, Journal of Vacuum Science and Technology B, **23**(6), 2944-2949 (2005).

B.2   Non-refereed proceedings, bookchapters etc.

- A. Boltasseva, R.B. Nielsen, **C. Jeppesen**, A. Kristensen, R. Bakker, Z. Liu, H.-K. Yuan, A.V. Kildishev, and V.M. Shalaev, *Fabricating plasmonic components for nano- and meta-photonics*, Metamaterials & plasmonics: Fundamental, Modelling, Applications, 209-221, Springer, Netherlands (2009).

- N. Kehagias, V. Reboud, G. Chansin, M. Zelsmann, **C. Jeppesen**, C. Schuster, F. Reuther, G. Gruetzner, and C.M.S. Torres, *3D nanofabircation by reverse contact UV nanoimprint lithography*, Microprocesses and Nanotechnology 2007, Digest of Papers Pages, 408-409 (2007).

B.3   Conference contributions (personally given)

- **C. Jeppesen**, S. Xiao, N. A. Mortensen, and A. Kristensen *Geometrical and fluidic tuning of nanoscale split-ring resonator*, CLEO, San Jose, California, May 31-June 5, 2010.

- **C. Jeppesen**, S. Xiao, N. A. Mortensen, and A. Kristensen, *Capacitance tuning of nanoscale split-ring resonators*, Invited Paper, SPIE Photonics Europe, 12-16 April 2010, Brussels, Belgium.

- **C. Jeppesen**, R. B. Nielsen, S. Xiao, N. A. Mortensen, A. Boltasseva, and A. Kristensen, *An experimental investigation of Fang's Ag superlens suitable for integration*, SPIE, Optics & Photonics, San Diego, CA, 2-6 August 2009.